SPUTTER DEPOSITION AND FORMATION MECHANISM OF Pt AND Pt ALLOY NANOPARTICLES

Lianlian Deng

Graduate School of Engineering

Hokkaido University

September 2019

SPUTTER DEPOSITION AND FORMATION MECHANISM OF Pt AND Pt ALLOY NANOPARTICLES

Lianlian Deng

Laboratory of Novel Materials Hybrid Engineering

Division of Materials Science and Engineering

Faculty of Engineering

Hokkaido University

A dissertation submitted to the Graduate School of Engineering

of Hokkaido University in

partial fulfillment of the requirements for the degree of

Doctor of Philosophy in Materials Science and Engineering

Abstract

Platinum (Pt) and Pt alloy nanoparticles (NPs) have been the subject of intense study, especially in catalysis. Chemical reduction methods often use reducing agents and stabilizing agents to produce metal NPs, and hence, the NPs can contain byproducts which can influence the catalytic properties. In addition, the synthesis of alloy NPs can result in core-shell structure or phase segregation due to different reduction potentials of different metal ions. To solve these issues, synthesis of metal and metal alloy NPs by vacuum sputtering onto a liquid matrix is proposed. The method is a green approach because it neither uses toxic reducing agents, nor produces any by-products. Further the top-down vacuum technique can generate metal atoms/clusters from the bulk metal targets, regardless the different reduction potentials of different metals, making the synthesis of solid solution alloy NPs become feasible. A low volatile liquid medium can be used in vacuum sputtering to control the growth, disperse, and stabilize NPs. However, the stability, growth, and formation mechanism of NPs are still the subject of discussion and dependent on multiple sputtering parameters. Thus, this study aims to synthesize Pt and Pt alloy NPs with desired size and understand the stability, growth and formation mechanism of the synthesized NPs.

Synthesis of highly uniform Pt NPs with small size (below 2.0 nm) and narrow size distribution by sputtering of Pt onto polyethylene glycol (Mw = 600) is the topic of chapter 2. The results indicate that particle sizes were tailorable from 0.9 ± 0.3 nm to 1.4 ± 0.3 nm by varying the sputtering current (5-50 mA) with negligible particle

aggregation occurred in PEG during sputtering. It is found that a slight growth of particle size after sputtering can be attributed to the addition of free Pt atoms to the existing Pt NPs. All samples formed stable dispersions in PEG for 5 months storage. This result suggests an advantage of using a liquid matrix to produce and stabilize NPs.

Chapter 3 in the thesis is devoted for the synthesis of well-dispersed and stable Pt/Cu alloy NPs and studying growth mechanism of the alloy NPs in sputtering of Pt/Cu alloy target onto PEG. The effects of sputtering current, rotation speed of the stirrer, sputtering time, sputtering period, and temperature of PEG on the particle size are studied systematically. The key results demonstrate that the aggregation and growth of Pt/Cu alloy NPs occurred at the surface as well as inside the liquid polymer after the particles landed on the liquid surface. According to particle size analysis, a low sputtering current, high rotation speed for the stirrer, short sputtering period, and short sputtering time are found to be favorable for producing small-sized single crystalline alloy NPs. On the other hand, varying the temperature of the liquid PEG does not have any significant impact on the particle size. Thus, these findings shed light on controlling NP growth using the newly developed green sputtering deposition technique.

Chapter 4 targets to the synthesis and formation mechanism of Pt/Au alloy NPs in a wide composition range by simultaneous sputter deposition of two independent magnetron sources onto PEG (Mw = 600). The resulting NPs are alloy with the face-centered cubic (fcc) structure. It is observed that the particle sizes, composition,

and shape are strongly correlated. On the other hand, these characteristics can be tailored by varying sputtering parameters appropriately. Large agglomerates are formed at Pt content less than 16 at. %, showing partial alloy structure. Highly dispersed NPs with no agglomeration in PEG can be obtained when Pt is more than 27 at. %. Moreover, a small amount of Pt could terminate the agglomeration of Au when sputtering on TEM grid. Experimental results for 30 min sputtering onto PEG for various sputtering currents, as well as computational simulations, indicate that using the formation energy and selective attachment during particle formation can be used for explaining the composition-dependent particle-size of Pt/Au NPs.

Finally, research findings, contribution, and perspective are summarized in chapter 5 of the thesis.

Acknowledgment

Thanks to my supportive supervisor, Professor Tetsu Yonezawa and Assistant Professor, Nguyen Thanh Mai, who shared their expertise and knowledge for the completion of this work. Thanks to Dr. Y. Ishida and Mr. H. Tsukamoto for fruitful discussion and Mr. H. Tsukamoto for his experimental assistance.

I also thank Mr. J. Shi for the help in my study and life. Thanks to my Japanese friends, Mr. Y. Komatsuzaki, Mr. S. Oono, and Mr. K. Yamamoto who helped me a lot during my stay in Japan. Thanks to Mr. K. Hiraya who helped me improve my Japanese. Thanks to my labmates in Laboratory of Novel Materials Hybrid Engineering who shared happiness and helped me during my stay in Sapporo. I also thank other friends here who cried, laughed, and celebrated the challenges of life with me. Thanks to my family who always support me. I thank Ministry of Education, Culture, Sports, Science and Technology-Japan (MEXT) for financial support for my stay in Sapporo.

Table of Contents

1 General Introduction 1

1.1 Properties and applications of platinum and platinum/copper, platinum/gold alloy nanoparticles 1

1.2 Generic synthesis of Pt and Pt/Cu, Pt/Au alloy nanoparticles 3

1.3 Fundamental of sputter deposition 4

1.4 Sputter deposition onto liquid to prepare nanoparticles 7

1.5 Size control of nanoparticles by sputter deposition 9

1.6 Synthesis of Pt and Pt/Cu, Pt/Au alloy nanoparticles by sputter deposition 13

1.7 Growth and formation mechanism 18

1.8 Summary and perspective 24

1.9 References 26

2. Pt nanoparticles prepared by single target sputtering 41

2.1 Introduction 41

2.2 Experimental section 43

2.2.1 Preparation of Pt nanoparticles 43

2.2.2 Characterization 44

2.3 Results and discussion 45

2.3.1 UV-vis spectra of Pt NPs dispersion of PEG 45

2.3.2 TEM observations of Pt NPs 47

2.3.3 Structure and colloidal stability of Pt NPs dispersed in PEG 53

2.4 Conclusions 57

2.5 References 59

3. Pt/Cu alloy nanoparticles prepared by single target sputtering 66

3.1 Introduction 66

3.2 Experimental section 69

3.2.1 Preparation of Pt/Cu NPs 69

3.2.2 Study of the particle growth mechanism 70

3.2.3 Characterization 72

3.3 Results and discussion 73

3.3.1 Composition, structure, and optical properties of the sputtered Pt/Cu NPs dispersed in PEG 74

3.3.2 Growth mechanism of Pt/Cu NPs during sputtering 78

3.4 Conclusions 94

3.5 References 95

4. Pt/Au alloy nanoparticles prepared by double target sputtering 103

4.1 Introduction 103

4.2 Experimental Section 105

4.2.1 Preparation of Pt/Au NPs 105

4.2.2 Characterization 106

4.2.3 Computational methods 108

4.3 Results and discussion 109

4.3.1 Pt/Au alloy NPs formed by simultaneous sputter deposition onto liquid PEG.

109
4.3.2 Relation among the size, shape, and composition of the prepared NPs 116
4.3.3 Possible formation mechanism..... 122
4.4 Conclusions..... 133
4.5 References..... 135
5. General conclusion..... 144
Appendix I. Supplementary information for chapter 2 147
Appendix II. Supplementary information for Chapter 3 153
Appendix III. Supplementary information for chapter 4..... 162
List of publications..... 176
List of research accomplishments 177

List of figures

Figure 1.1 (a) Representative scheme of a typical DC-magnetron sputtering system. (b) Details of the magnetron. (c) Representative scheme of the physical ejection of atoms from the target to the substrate surface. 5
Figure 1.2 TEM images of Au NPs prepared by sputter deposition onto EMI-BF4 (a) and TMPA-TFSI (b). 8
Figure 1.3 Schematic illustrations of Au-Ag foil binary targets having various f_{Au}. (b) Photographs of BMI-PF_6 obtained after the sputter deposition of Ag (f_{Au} = 0, left), Au/Ag (f_{Au} = 0.50, center) and Au (f_{Au} = 1, right) NPs. 8
Figure 1.4 Left: schematic (not to scale) of the combinatorial co-deposition from two sputter targets into a cavity array substrate filled with IL. Right: Schematic of the proposed formation process of NP in IL. 9
Figure 1.5 (a) The scattering profiles of the Au NPs in [C_4mim]BF_4 that were generated at working distances of 25 (red points), 50 (green points), and 75 mm (blue points). The black curves are theoretical fittings, which were obtained with the assumption that the NPs are spherical and the size distribution is expressed by C distribution. (b) The particle size distributions against the diameter for the scattering profiles of Fig. 2(a). The working distance dependences of d_{peak} (closed circles) and WFWHM (open circles) are shown in the inset. 11
Figure 1.6 The size distributions of Au NPs synthesized at different target temperatures. 11
Figure 1.7 Particle-size distributions of Au NPs generated in PEG at different temperatures. 12
Figure 1.8 TEM images and size-distribution histograms of Au NPs prepared in PEG (a,c) without and (b,d) with stirring. 13
Figure 1.9 HRTEM images of Pt NPs sputtered for various durations: (a) 10 s, (b) 20 s, (c) 30 s, (d) 45 s, (e) 60 s and (f) 120 s with a deposition power of 30 W and TA = 23.8. 15
Figure 1.10 TEM micrographs of 1 mt Pt deposits at two different metal concentrations: (a) 1.5×10^{15}; and (b) 5.3×10^{15} atoms/cm^2. 16
Figure 1.11 Schematic illustration of Pt–SWCNT composite material fabricated in this study. 16
Figure 1.12 TEM images and size distributions of NPs obtained by sputter deposition on TMPA-TFSA: (a) Au NPs (f_{Au} = 1.0), (b) AuPt NPs (f_{Au} =0.33), and (c) Pt NPs (f_{Au} = 0). 18
Figure 1.13 Possible mechanisms for the nucleation and growth of sputtered gold NPs into ILs. 20
Figure 1.14 Schematic mechanism for sputtering of titanium onto PEEL (left-hand side) and silver into BMIMTFSI (right-hand side). 23
Figure 1.15 Schematic illustration for the formation of AgNPs or AgTFs by sputtering deposition of Ag onto liquids. 23
Figure 1.16 Scheme of the growth mechanism of gold nanoparticles after sputter deposition onto an ionic liquid. 24
Figure 2.1 UV-Vis spectra of NPs obtained by sputter deposition onto PEG (left) and

photograph of Pt NPs dispersion of PEG under room light (right) with different sputtering current. 46
Figure 2.2 TEM images and size distributions of NPs obtained by sputtering onto PEG under sputtering current of (a) 5 mA, (b) 10 mA, (c) 20 mA, (d) 50 mA. 48
Figure 2.3 TEM images and size distributions of NPs obtained by sputtering on TEM grid for 1 s under sputtering current of (a) 10 mA, (b) 20 mA, (c) 50 mA. Sample sputtered under 5 mA was hard to observe in normal TEM. 50
Figure 2.4 Relation between particle size and sputtering current sputtered onto PEG (black), on grid for 1 s (red) and on grid for 5 s (blue).....52
Figure 2.5 (a) Particle size of Pt NPs in PEG under various sputtering currents after 0, 10, 20, 30 days and 5 months measured by normal TEM and (b) particles size growth of Pt NPs in PEG prepared at sputter current of 20 mA. 53
Figure 2.6 (a) UV-vis spectra of Pt NPs in PEG sputtered at 20 mA for as-synthesized and storage samples after keeping for 0-30 days and magnified pictures of UV-Vis spectra shown in (a) for (b) low wavelength and (c) higher wavelength region. 55
Figure 2.7 STEM-HAADF images of as-sputtered Pt NPs in PEG (a) and Pt NPs in PEG after 30 days (b), 43 days (c), and 50 days (d) stored under room temperature in dark under the sputtering current of 20 mA. TEM images of Pt NPs sputtered on grid for 1s, 5s and 30s under the sputtering current of 20 mA were given in Figure 2.3b, Figure S2, and S3 respectively.....56
Figure 3.1 (a) UV-Vis absorption spectra of Pt (black curve), Pt/Cu (red curve), and Cu (blue curve) NPs obtained by continuous sputter deposition onto PEG at a sputtering current of 20 mA and (b) their respective enlarged spectra. 74
Figure 3.2 Pt/Cu NPs prepared by continuous sputtering onto PEG at a sputtering current of 50 mA for 30 min, with a rotation speed of 80 rpm at 30 °C. (a) HAADF-STEM image, corresponding EDX mapping images of (b) Pt L and (c) Cu K, (d) STEM-EDX line profile measured across two NPs; the inset shows the STEM-HAADF image of the analyzed NPs (the yellow arrow shows the scanning path for the line profile). (e) HR-TEM image of a Pt/Cu NP. 75
Figure 3.3 XRD profiles of a Pt/Cu alloy target (pink curve), Pt/Cu thin films sputtered on XRD glass substrates at a sputtering current of 50 mA for 5 min (orange curve) and 1 min (green curve), Pt/Cu NPs prepared by continuously sputtering onto PEG at a sputtering current of 30 mA with a rotation speed of 80 rpm for 4 h at 30 °C (red curve); the stick patterns represent the reference patterns of Cu (JCPDS number 04-0836) and Pt (JCPDS number 04-0802). 77
Figure 3.4 Photographs of PEG dispersions of Pt/Cu NPs under ambient light (left) and UV-Vis absorption spectra of the NPs (right) obtained by continuous sputter deposition onto PEG at different sputtering currents for 30 min at 30 °C with a rotation speed of 80 rpm. 79
Figure 3.5 TEM images and size histograms of the NPs obtained by continuous sputtering onto PEG at different sputtering currents: (a) 5, (b) 10, (c) 20, (d) 30, (e) 40, and (f) 50 mA for 30 min at 30 °C with a rotation speed of 80 rpm. 81
Figure 3.6 Size histograms of NPs obtained by sputtering onto TEM grids for 5 s at different sputtering currents: (a) 10 mA, (b) 20 mA, (c) 30 mA, (d) 40 mA, (e) 50 mA. The insets

are corresponding TEM images; all scale bars are 20 nm. 84
Figure 3.7 Relationship between the particle size and sputtering current. Continuous sputtering onto PEG (black) and TEM grids for 1 s (red) and 5 s (blue). 84
Figure 3.8 Relationship between particle size and rotation speed of the stirrer. The error bars represent the standard deviation of the particle size. 85
Figure 3.9 (a) A schematic illustration of different sputtering periods. (b) Schematic diagram illustrating our hypothesis of the growth of Pt/Cu NPs on the PEG surface at short and long sputtering periods. (c) Relationship between particle size and sputtering period. Size histograms of Pt/Cu NPs at a fixed sputtering current of 50 mA, rotation speed of 80 rpm, PEG temperature of 30 °C, and different sputtering periods of (d) 30 min and (e) 5 s. The total sputtering time (excluding 5 s stopping time between two sputtering periods) in all the cases was 30 min. The imag1e of Pt/Cu NPs prepared with the sputtering period of 30 min without interval is shown in Figure 3.5(f). 88
Figure 3.10 Size histograms of Pt/Cu NPs obtained by continuous sputtering onto PEG at a fixed sputtering current of 30 mA, PEG temperature of 30 °C, rotation speed of 80 rpm, and different sputtering times. (a) 15 min, (b) 1 h, (c) 2 h, and (d) 4 h. Insets are the corresponding TEM images, all the scale bars are 20 nm. (e) Corresponding STEM image at a sputtering current of 30 mA for 4 h. (f) Relationship between NP size and sputtering time. The TEM image and size distribution of the NPs obtained at a sputtering time of 30 min is shown in Figure 3.5(d). 89
Figure 4.1 UV-vis absorption spectra of samples obtained by sputtering of only Pt (I), only Au (II), physical mixture of (I) and (II) samples (III), sputtering Pt target for 30 min followed by sputtering Au target for 30 min (IV), sputtering Au target for 30 min followed by sputtering Pt target for 30 min (V), and simultaneous sputtering of Pt and Au for 30 min (VI). 111
Figure 4.2 XRD patterns of Pt/Au NPs obtained via sputtering onto PEG under various sputtering current of Pt target from 0 (black), 10 (red), 20 (blue), 30 (pink), 40 (green) and 50 mA (cyan) while keeping sputtering current of Au target constant at 50 mA (a). XRD patterns in (a) in range of 2θ from 35.0° to 42° (b). Stick patterns are the reference patterns of Pt (JCPDS #04-0809) and Au (JCPDS #04-0784). The relation between the lattice parameter and Pt at. % of the bimetallic NPs (c); the data collecting from the samples of Pt-50 mA/Au-40 mA (41 at.% Pt), Pt-50 mA/Au-30 mA (51 at.% Pt), Pt-40 mA/Au-20 mA (57 at.% Pt), and Pt-50 mA-4 h (100 at.% Pt) were also used in this graph. HAADF-STEM image (JEOL JEM-ARM200F, operating at 200 kV) of Pt/Au NPs obtained by sputtering onto PEG under sputtering current of Pt-50 mA/Au-50 mA (d). HAADF-STEM image (JEOL JEM-ARM200F, operating at 120 kV) of Pt/Au NPs obtained by sputtering onto PEG under sputtering current of Pt-20 mA/Au-50 mA (e), corresponding STEM EDX-mapping images of Pt L (f) and Au L (g), UV-Vis absorption spectra of PEG-NPs dispersions produced by co-sputtering onto PEG using different sputtering current of Pt target from 0-20 mA (h) and 20-50 mA (i) while keeping sputtering current of Au target constant at 50 mA. 112
Figure 4.3 TEM images of NPs dispersed in PEG obtained by sputtering onto PEG using different sputtering currents of Pt and Au targets (0-50 mA). Particles in the same column were obtained using the same sputtering current for Pt with increasing sputtering

current for Au from top to bottom. Particles in the same row were obtained using the same sputtering current for Au with an increase of sputtering current for Pt from left to right. Numbers as insets show particle size (in white text) and composition (in yellow text) of the bimetallic Pt/Au NPs in term of Pt at. %. The scale bar in the image is 20 nm. 118

Figure 4.4 Size distributions of NPs obtained by sputtering onto PEG using different sputtering currents of Au target: 10 (a), 20 (b), 30 (c), 40 (d), 50 mA (e) while keeping sputtering current of Pt target constant at 50 mA, and using different sputtering currents of Pt target: 40 mA (f) and 30 mA (g) while keeping sputtering current for Au target constant at 50 mA. 119

Figure 4.5 Relation between NP size and Pt atomic content, the fitting curve is based on the Boltzmann model. The R^2 value for the nonlinear fit of the data is 0.985. The data collecting from the samples of Pt-50 mA/Au-5 mA (93 at. % Pt) and Pt-50 mA (100 at. % Pt) were also used in this graph. 119

Figure 4.6 Schematic diagram illustrates the relation of sputtering current, formation energy, and particle size: when Pt content is increased, the formation energy of the particles is increased, and hence this results in the formation of smaller particles. 127

Figure 4.7 HAADF image (a) and EDX mapping results of the sample obtained by sputtering onto PEG at sputtering current of Pt-50 mA/Au-50 mA for Pt L (b), Au L (c), and overlap image of Pt and Au (d). EDX-line profile results (e) of the Pt L (red line)/Au L (blue line) for another nanoparticle of the sample. ((a)-(d) were obtained by JEOL JEM-ARM200F, operating at 80 kV, (e) were obtained by JEOL JEM-ARM200F, operating at 200 kV.) 129

Figure 4.8 DFT-simulated Au_{25} (a), Pt_1Au_{24} with Pt atom on the surface (b), Pt_1Au_{24} with Pt atom in the center (c), Pt_2Au_{23} with Pt atoms on the surface (d), and Pt_2Au_{23} with Pt atoms in the center (e) clusters. Au and Pt atoms are shown in yellow and gray respectively. 131

Figure 4.9 Schematic illustration for the formation of Pt/Au alloy NPs by sputtering deposition of Pt and Au onto PEG. 132

List of tables

Table 1.1 Sputter Currents, Composition, and Size for Cu, Au, and Au/Cu Alloy NPs. 12
Table 3.1 Summary of the experimental parameters 72
Table 3.2 XRF and EDX analyses of the sputtered materials 76
Table 4.1 Summary of different preparation methods. 111
Table 4.2 DFT calculated adsorption energy and bond length between the model PEG molecule and different surfaces. 124
Table 4.3 EDX results of particle shown in Figure 4.11a-d. 129
Table 4.4 Formation energy of different structures of Au_{25}, Pt_1Au_{24}, and Pt_2Au_{23}. 132

List of abbreviations

TEM	Transmission Electron Microscopy
HR-TEM	High Resolution Transmission Microscopy
UV-Vis	Ultraviolet-Visible spectroscopy
EDS	Energy Dispersive X-ray Spectroscopy
STEM	Scanning Transmission Electron Microscopy
HAADF-STEM	High Angle Annular Dark Field- Scanning Transmission Electron Microscopy
XRF	X-ray Fluorescence Spectroscopy
XRD	X-ray Diffraction
XPS	X-ray photoelectron Spectroscopy
MUA	Mercaptoundecanoic Acid
PEG	Polyethylene Glycol
DFT	Density Functional Theory
nm	nanometer
NPs	nanoparticles
RTILs	room temperature ionic liquids
SWCNT	single-walled carbon nanotube
DC	direct current
RF	radio frequency

1 General Introduction

1.1 Properties and applications of platinum and platinum/copper, platinum/gold alloy nanoparticles

Nanoparticles (NPs) are defined as particulate dispersions or solid particles with a size in the range of 10~1000 nm.[1] Metal NPs have been applied in many different areas, for example, they have been widely used in catalysis,[2] biological labeling,[3] optoelectronics,[4] and information storage.[5-6] Monometallic and bimetallic NPs have been studied intensively. Monometallic NPs composed of only single metal. Monometallic NPs are of different types depending upon the type of metal atom present such as magnetic and transition metal NPs, etc. There are two general methods to synthesize monometallic NPs, chemical and physical routes, and the most common is the colloidal synthesis due to its good control on the particle size in solution.[7] Structure and size of particle can be stabilized by using stabilizing agents.[7-8] On the other hand, bimetallic NPs, consist of two different metals, have drawn a greater attention than the monometallic NPs from both scientific and technological point of view.[9-10] Their size, shape, structure, and composition determine the properties of the bimetallic NPs. Therefore, many researchers have been focused on the synthesis of NPs to have a good control on the size, shape, structure, and composition of particles.[10-13] The properties of bimetallic NPs may differ from those of monometallic NPs, such as composition and size dependent optical, catalytic effects et al.[7, 14-15]

Platinum (Pt) NPs have been intensively investigated because of their unique catalytic,[16] and also drawn attention as sensor[17] or have many biomedical applications.[18] However, the widespread commercialization and deployment of Pt catalyst is still limited due to their high cost. For example, the cost of Pt in a hydrogen polymer electrolyte membrane fuel cell (PEMFC) for a 100 kW (134 hp) vehicle is much higher than that for an entire 100 kW gasoline engine. According to the cost reduction targets set by the U.S. Department of Energy (DOE), the total Pt catalyst loading (on both anode and cathode) in a membrane electrode assembly (MEA) must be reduced to below 0.125 $mg \cdot cm^{-2}$.[19] On the other hand, pure Pt nanocatalyst are easy to deactivation or poisoning during catalytic activity. To enhance the effectiveness of Pt catalysts and anti-poisoning ability, Pt-based bimetallic nanoparticle catalysts have been synthesized. It also helps in decreasing the amount of need of noble metal, Pt.[20-21] The Pt-X (X = Cu,[22-25] Au,[26-28] or Ag, etc.) alloys are very important due to their high catalytic performance compared with their corresponding monometallic NPs.[29] In the recent years, polymer-protected colloidal Pt/Cu alloy particles have been prepared and these can be used for the catalytic hydrogenation of solution, where the bimetallic clusters are used as active and selective agents for the hydration of acrylonitrile to acrylamide as well as for hydrogenation of 1,3-cyclooctadiene to cyclooctene.[30] It has also been found that Pt/Cu bimetallic catalysts are effective in the reduction of NO_x. Studies about Pt/Cu based bimetallic NPs have revealed their heterogeneous catalytic activities for reduction of gas phase NO with hydrogen as the reducing agent.[31-32] On the other hand, Pt/Au bimetallic NPs

have also been studied widely. Hu et al. have concluded that bimetallic Pt/Au nanocatalyst shows better catalytic capability as compared with monometallic Au or Pt.[33]

1.2 Generic synthesis of Pt and Pt/Cu, Pt/Au alloy nanoparticles

The catalytic property can be sensitive to metal particle size and composition because the surface structure and electronic properties can change greatly in the 1-50 nm size range. NPs with small size and relatively narrow particle size distribution show high catalytic activity due to large number of atoms on surface.[34] Thus, a great effort has been made to synthesize particles with small size and narrow size distribution. Researchers have discovered many new methods to prepare NPs which are of the required size, composition, and shape because these factors greatly influence the properties of the material. Pt, Pt/Cu, and Pt/Au alloy NPs have been prepared using radio frequency sputtering, reverse micelles,[35-36] electron beam lithography[37] and chemical vapor deposition techniques. Among these methods, considerable research efforts have been devoted to prepare catalysts by chemical reduction routes. This method produces metallic NPs in the zero valent state. In this method, two processes namely, reduction and interaction between the metallic NPs and polymeric species operate. Different reducing agents such as sodium borohydride, elemental hydrogen, Tollen's reagent and ascorbate, etc. are being used. For example,

Pt NPs synthesized by chemical methods with stabilizing agents such as poly(vinyl pyrrolidone) (PVP),[38] 3-(N,N-dimethyldodecylammonio) propanesulfonate (SB12),[39] etc. Pt/Cu alloy NPs are obtained by chemical reduction routes[22-24] using strong reducing agents[23] or at high temperatures.[22, 24-25] Pt/Au alloy NPs synthesized by chemical methods reported by other groups.[40-43]

However, NPs prepared by chemical reduction methods often use the toxic reducing agents and contain byproducts which usually results in the obtained NPs with limited purity and influence their future application such as the catalytic properties.[44] In order to synthesize small particles, stabilizer is needed, which is also reduce the catalytic activity if it is not removed completely. However, removal of these stabilizers usually requires harsh treatment such as thermal treatment[39, 44] or acid treatment.[44] On the other hand, in the case of synthesis of alloy NPs, due to different reduction potential of different metal ions, core-shell structure or phase segregation is easily obtained instead of alloy NPs.[45-46]

1.3 Fundamental of sputter deposition

In 1852, sputtering was conducted in a DC (direct current) gas discharge tube by Grove.[47] He found that the cathode surface of the discharge tube was sputtered by energetic ions formed in the gas phase and that the cathode material was deposited on the inner wall of the discharge tube. It is well accepted that in the sputter deposition process, when a metal target is attacked by gaseous ions, metal atoms or clusters

(aggregation of several atoms) are ejected; these metal atoms or clusters collide with each other multiple times to form NPs. This technique is commonly used for thin-film deposition, etching, and analytical techniques.[48-52] Today, with the further development of sputter deposition technique, there are different ways to perform sputtering, for example, DC-diode, RF-diode (radio frequency), and magnetron sputtering.

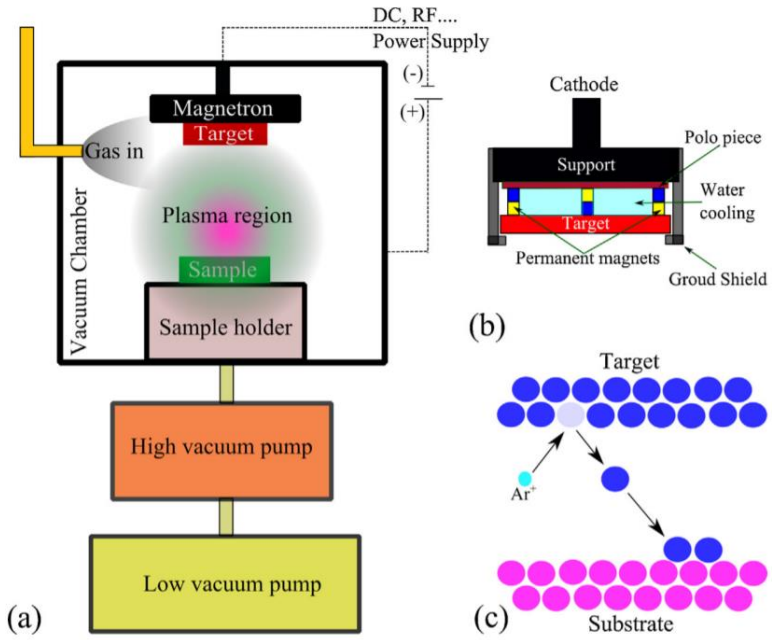

Figure 1.1 (a) Representative scheme of a typical DC-magnetron sputtering system. (b) Details of the magnetron. (c) Representative scheme of the physical ejection of atoms from the target to the substrate surface.

Reproduced with permission from ref 53. Copyright 2013 Elsevier Ltd.

Figure. 1a–c shows a representative sputter deposition system, which consists of target, magnetrons, substrate positions, substrate holder, vacuum chamber, vacuum

pumps, power supplies, plasma, and the physical ejection of atoms from the target to the substrate surface.[53] Due to the applied electric field, the electrons follow helical paths around the magnetic field lines, undergoing ionizing collisions with gaseous neutrals near the target surface. However, as the sputtered atoms are neutrally charged, they are unaffected by the magnetic trap. Therefore, it is well accepted that there occur no considerable collisions between the sputtered species in the gas phase at low gas pressures.[54-55] Controlling of all experimental parameters during the sputtering process, such as, sputtering time, sputtering current, target temperature, position of substrate, et al. is a fundamental way to achieving the desired properties in the final product.[56-57]

In general, sputtering is performed onto solid substrates, where the atoms nucleate and a film begins to grow after a few seconds. Models of thin film nucleation processes and other details can be seen in the sputtering deposition handbook.[58] However, Instead of the traditional solid substrate,[59-60] using a liquid substrate for vacuum sputtering can be considered as a suitable method for obtaining alloy NPs with controllable size, shape, and composition.[60-62] Many kinds of liquids can be used as the substrate, such as ionic liquids,[63-68] polymers,[7, 69-75] silicone oil,[76] and vegetable oil,[54] Actually, this process can be conducted on any liquid that has a sufficiently low vapor pressure to be introduced inside a vacuum condition.

1.4 Sputter deposition onto liquid to prepare nanoparticles

The first sputtering deposition onto a liquid substrate was performed in 1996: the RF magnetron sputtering of silver directly onto pure silicone oil.[77] During the sputtering process, Ag clusters on the surface of the silicone oil grow gradually and begin to connect with each other. Finally, a continuous rough thin film with a distinct surface morphology form. Further investigations into film deposition onto silicone oil surface were carried out,[78-82] in 1999 when an innovative study was proposed by Wagener who reported for the first time, Fe NPs with an average size of 10-15 nm and narrow particle size distribution were obtained by sputtering onto mineral oil and silicone oil.[83] However, silicone oil cannot stabilize NPs efficiently, and the obtained NPs were not stable. Thus, it is very necessary to find a good liquid substrate for the sputter deposition of NPs without using stabilizers to control particle growth and stabilize NPs. Ever since Torimoto group synthesized stable colloidal metal NPs by sputtering Au target onto ionic liquid without using stabilization agents in 2006 (Figure 1.2)[84], sputter deposition on liquid was applied to several ionic liquids, and efforts have been devoted to understand the mechanism of nanoparticle formation through sputtering onto ionic liquids.[55] Recently, not only monometallic NPs but also bimetallic NPs have been synthesized by sputter deposition. For example, Au/Ag (Figure 1.3),[65] Au/Pt,[66] and Au/Cu[67] alloy NPs have been prepared by sputtering a mixed target material onto an ionic liquid by the Torimoto group. Au/Ag,[70] Au/Cu (Figure 1.4),[62, 71] and Au/Pd[68] alloy NPs synthesized by co-sputtering onto liquids have been reported. Au/Pd alloy NPs have also been prepared by sputtering alloy

targets onto ionic liquids.[85]

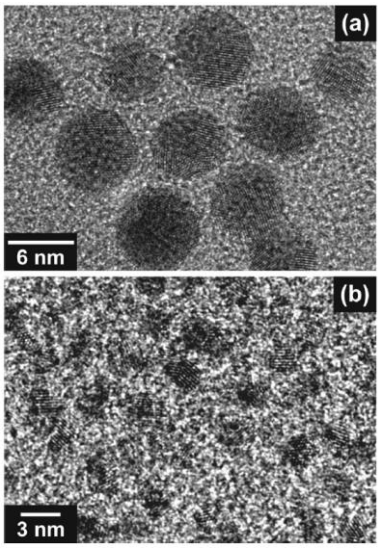

Figure 1.2 TEM images of Au NPs prepared by sputter deposition onto EMI-BF4 (a) and TMPA-TFSI (b).

Reproduced with permission from ref 84. Copyright 2006 AIP Publishing.

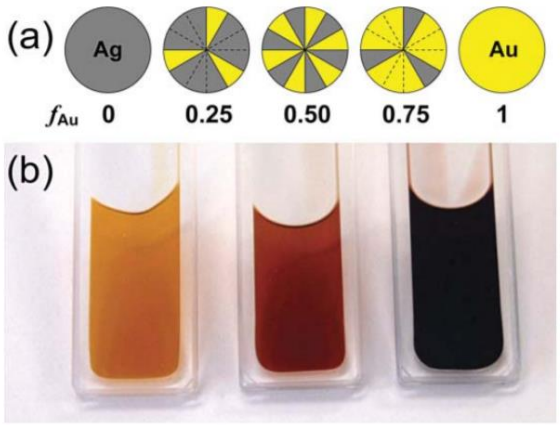

Figure 1.3 Schematic illustrations of Au-Ag foil binary targets having various f_{Au}. (b) Photographs of BMI-PF_6 obtained after the sputter deposition of Ag (f_{Au} = 0, left), Au/Ag (f_{Au} = 0.50, center) and Au (f_{Au} = 1, right) NPs.

Reproduced with permission from ref 65. Copyright 2008 RSC Publishing.

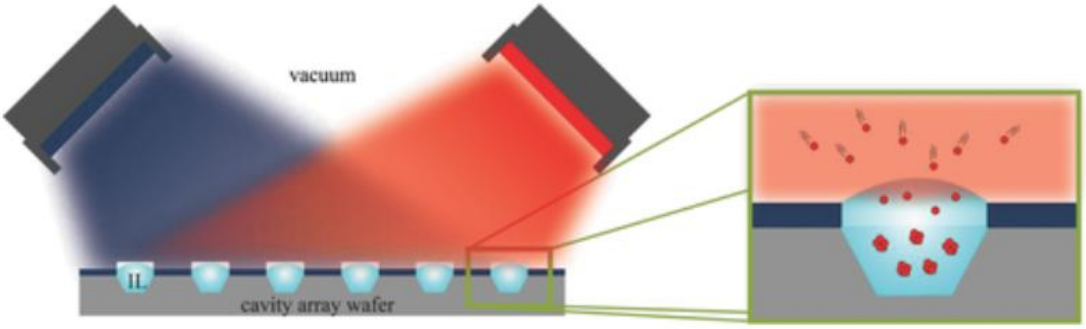

Figure 1.4 Left: schematic (not to scale) of the combinatorial co-deposition from two sputter targets into a cavity array substrate filled with IL. Right: Schematic of the proposed formation process of NP in IL.

Reproduced with permission from ref 62. Copyright 2014 Wiley-VCH.

1.5 Size control of nanoparticles by sputter deposition

Properties and functions of NPs are strongly dependent on the size, composition, and shape, especially the synthesis of size-controlled NPs is very important. Controlling the particle size and size distribution is the primary aim in the synthesis of metal NPs by both chemical and physical routes. In the sputtering deposition method, this control could be realized by varying experimental parameters.[53] To control the parameters related to the sputtering process, parameters such as kinds of liquid, distance between the target and the substrate (Figure 1.5),[56] temperature of target (Figure 1.6),[56] sputtering current (Table 1.1),[71] temperature of liquid (Figure 1.7),[69] and sputtering time[56] are adjusted to control the particle size and particle size distribution. These parameters in general result in controlling the number of target

metal atoms ejected from the target and varying the physical property of liquid substrate, resulting in NPs with different sizes, size distributions, shapes, and compositions. For example, in order to control the growth in the liquid solution, the surface tension and viscosity of the liquid medium are the most important parameters. It is reported that varying the temperature of the liquid substrate from 0 to 60 °C controlled the viscosity and results in Au NP size increasing from about 2 to 8 nm (Figure 1.7).[69] Furthermore, it is also reported that stirring liquid during sputtering deposition decreased the size and size distribution of the NPs from 7.4 ± 2.1 nm to 3.7 ± 0.9 nm because stirring the liquid accelerates the diffusion of metal atoms and clusters not only on the liquid surface but also inside the liquid, thus, suppressing the accumulation of NPs on the liquid surface and inside the bulk liquid, finally forming small particles (Figure 1.8).[86] Varying sputtering parameters to control the sizes of NPs have been widely attempted. Current progress in this field includes dissolving stabilizing agents in liquid to offer precisely control of NPs' size and properties.[72-73] The use of thiol molecules as a stabilizer due to their strong affinity with noble metal atoms for controlling the particle diameters via sputtering deposition.

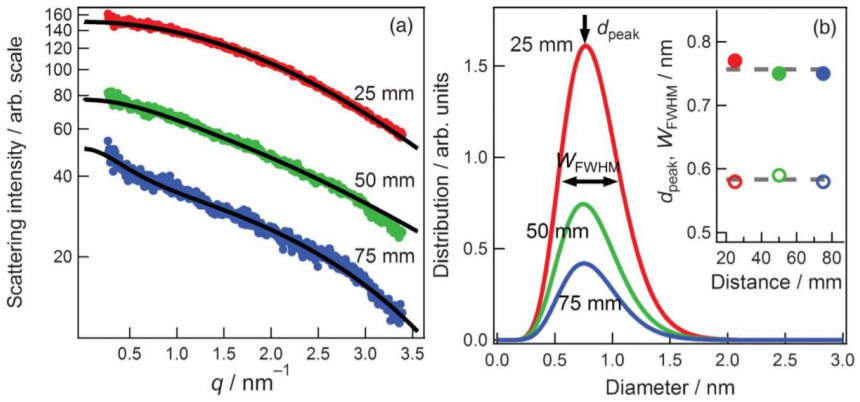

Figure 1.5 (a) The scattering profiles of the Au NPs in $[C_4mim]BF_4$ that were generated at working distances of 25 (red points), 50 (green points), and 75 mm (blue points). The black curves are theoretical fittings, which were obtained with the assumption that the NPs are spherical and the size distribution is expressed by C distribution. (b) The particle size distributions against the diameter for the scattering profiles of Fig. 2(a). The working distance dependences of d_{peak} (closed circles) and WFWHM (open circles) are shown in the inset.

Reproduced with permission from ref 56. Copyright 2011 RSC Publishing.

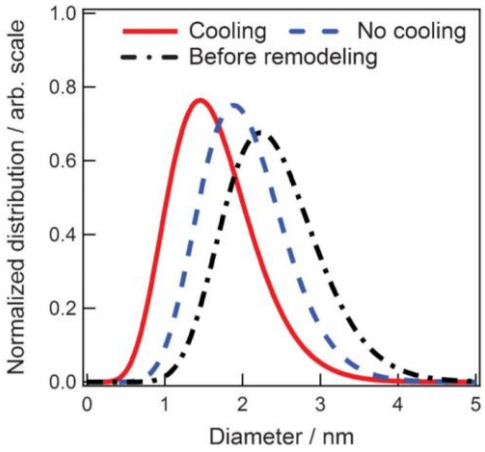

Figure 1.6 The size distributions of Au NPs synthesized at different target temperatures.

Reproduced with permission from ref 56. Copyright 2011 RSC Publishing.

Table 1.1 Sputter Currents, Composition, and Size for Cu, Au, and Au/Cu Alloy NPs.

Reproduced with permission from ref 71. Copyright 2017 ACS Publications.

	sputter current			Cu content			particle size	
sample no.	I_{Cu}[a]/mA	I_{Au}[a]/mA	products	$C_{Cu,ICP}$[b]/mol %	$C_{Cu/grid}$[c]/mol %	$C_{Cu/PEG}$[d]/mol %	d_{grid}[e]/nm	d_{PEG}[f]/nm
1	0	10	Au	0	0	0	1.7 ± 0.7	2.6 ± 0.8
2	0	20	Au	0	0	0	1.8 ± 0.5	2.7 ± 0.9
3	40	0	Cu	100	100	100	1.2 ± 0.2	1.0 ± 0.3
4	50	0	Cu	100	100	100	1.3 ± 0.3	1.5 ± 0.4
5	30	10	Au/Cu	57			1.3 ± 0.4	1.7 ± 0.4
6	40	10	Au/Cu	65			2.1 ± 0.5	1.9 ± 0.5
7	50	10	Au/Cu	71	58 ± 11	41 ± 11	1.7 ± 0.5	2.0 ± 0.5
8	30	20	Au/Cu	34			1.7 ± 0.5	2.1 ± 0.6
9	40	20	Au/Cu	42	43 ± 15		2.2 ± 0.6	2.5 ± 1.0
10	50	20	Au/Cu	48	44 ± 8	24 ± 9	2.6 ± 0.8	2.2 ± 0.6
11[g]	20		Au/Cu	43	37 ± 11		1.7 ± 0.3	2.0 ± 0.5
12[g]	40		Au/Cu	43			2.5 ± 1.7	2.5 ± 0.9

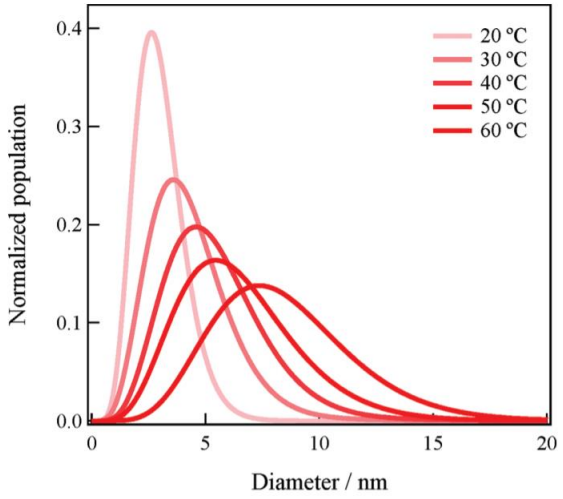

Figure 1.7 Particle-size distributions of Au NPs generated in PEG at different temperatures.

Reproduced with permission from ref 69. Copyright 2011 American Chemical Society.

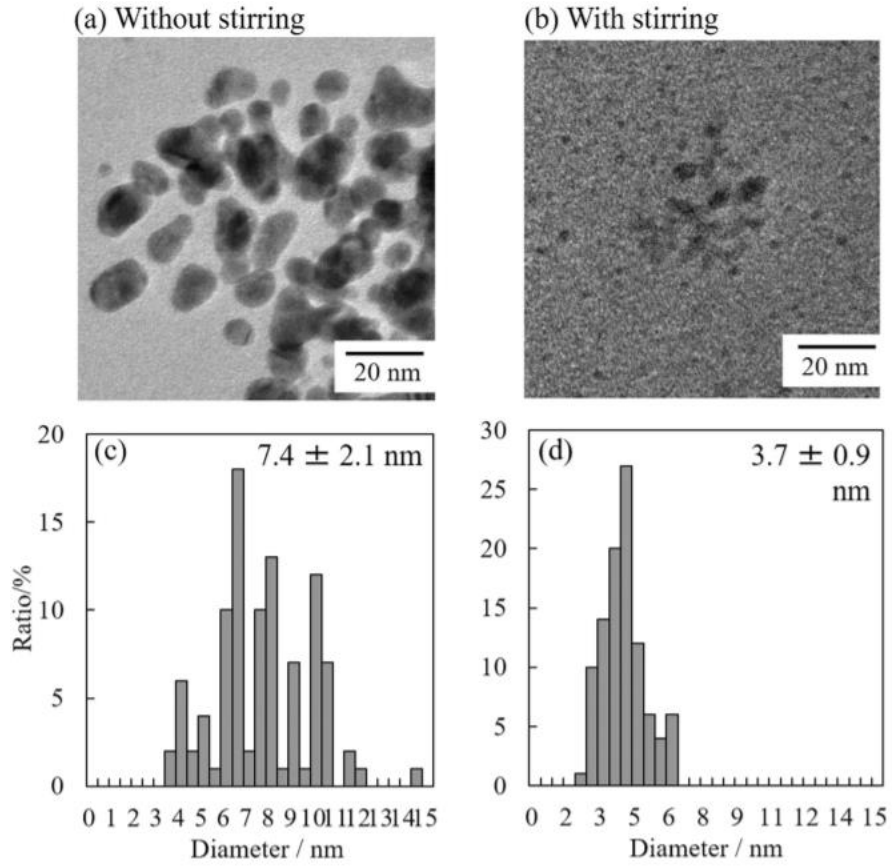

Figure 1.8 TEM images and size-distribution histograms of Au NPs prepared in PEG (a,c) without and (b,d) with stirring.

Reproduced with permission from ref 86. Copyright 2016 Nature Publishing Group.

1.6 Synthesis of Pt and Pt/Cu, Pt/Au alloy nanoparticles by sputter deposition

Small Pt and Pt-based alloy NPs are highly interesting thanks to their high ratios of surface atoms and thus enhance the catalytic properties.[87-88] A handful study has prepared Pt NPs with size below 2 nm via a chemical reduction in organic media[89] while most of the reported Pt NPs sizes were larger than 2 nm. Pt NPs have been prepared by sputtering without stabilizers.[90-97] Ramalingam et al. studied the NP

growth during sputtering onto solid substrate by varying the target angle, power, and time (Figure 1.9).[90] Andreazza et al studied the nucleation and coalescence island mechanisms of Pt by sputtering onto solid substrate (Figure 1.10).[91] Yoshii et al. reported that using Pt-sputtered room temperature ionic liquids (RTILs), and succeeded in the establishment of a facile Pt nanoparticle-single-walled carbon nanotube (SWCNT) composite fabrication method. They found that RTIL can work as nanoglue for sticking Pt NPs against SWCNTs (Figure 1.11).[92] Staszek et al. have synthesized Pt NPs with average size of 1.7 nm by sputtering onto IL.[93] Carbon-supported 2 nm and highly dispersed platinum NPs were synthesized by sputtering onto water.[94] Although many kinds of liquid were used as capture medium to synthesize Pt NPs, size control of sub-2 nm Pt NPs sputtered onto PEG and the stability of Pt in PEG have not been addressed yet.

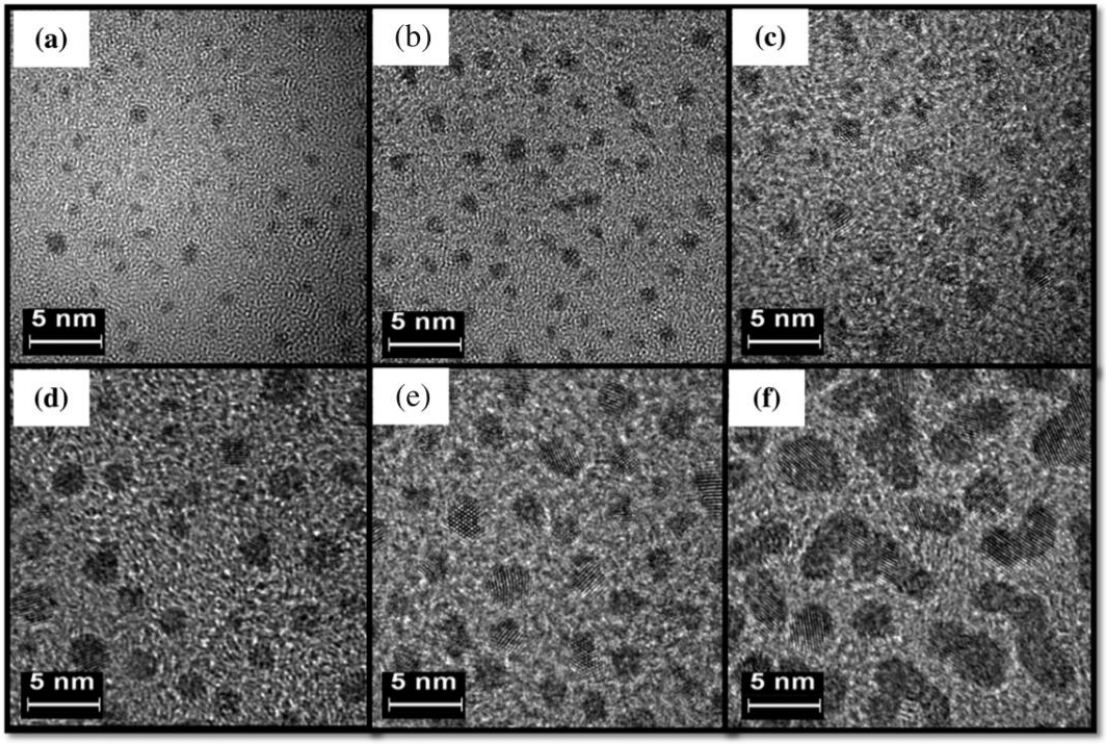

Figure 1.9 HRTEM images of Pt NPs sputtered for various durations: (a) 10 s, (b) 20 s, (c) 30 s, (d) 45 s, (e) 60 s and (f) 120 s with a deposition power of 30 W and TA = 23.8. Reproduced with permission from ref 90. Copyright 2013 IOP Publishing.

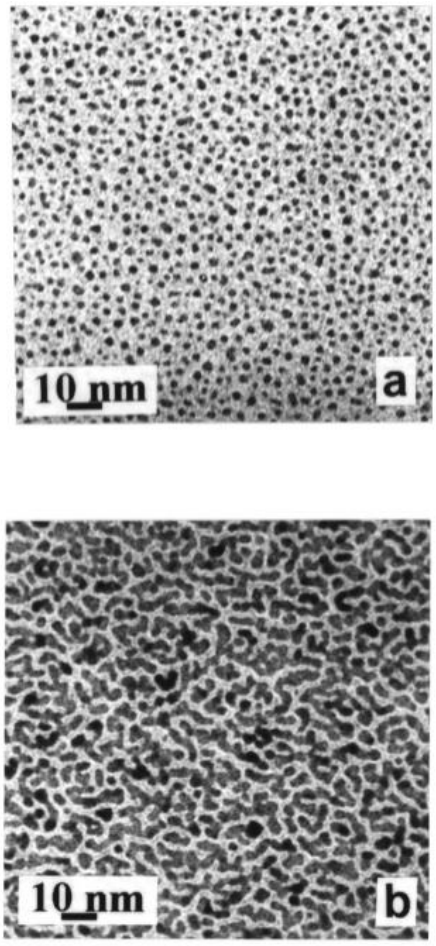

Figure 1.10 TEM micrographs of 1 mt Pt deposits at two different metal concentrations: (a) 1.5×10^{15}; and (b) 5.3×10^{15} atoms/cm^2.

Reproduced with permission from ref 91. Copyright 2002 Elsevier Ltd.

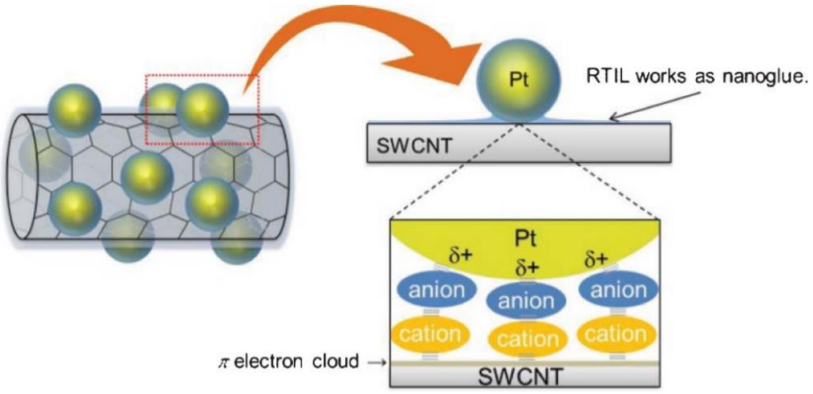

Figure 1.11 Schematic illustration of Pt–SWCNT composite material fabricated in this study.

Reproduced with permission from ref 92. Copyright 2012 RSC Publishing.

In the synthesis of Pt/Cu alloy NPs by sputter deposition, an interesting approach for the synthesis of Pt/Cu bimetallic NPs by sputtering onto TiO_2 nanotube arrays was described by Farsinezhad et al. The results showed that Pt/Cu have emerged as high performance photocatalysts for both photooxidation and photoreduction[98] However, as far as we know, the synthesis of Pt/Cu alloy NPs by sputtering onto a liquid has not been reported yet. As for synthesizing Pt/Au alloy NPs by sputter deposition, it is reported that Pt/Au alloy NPs have been synthesized by single target sputtering onto ionic liquid using mixed foil targets (Figure 1.12).[66] However, this method requires various targets with different composition for varying composition of the resulting alloy NPs. Thus, a sputtering system comprised of multiple targets for alloy formation would be ideal.

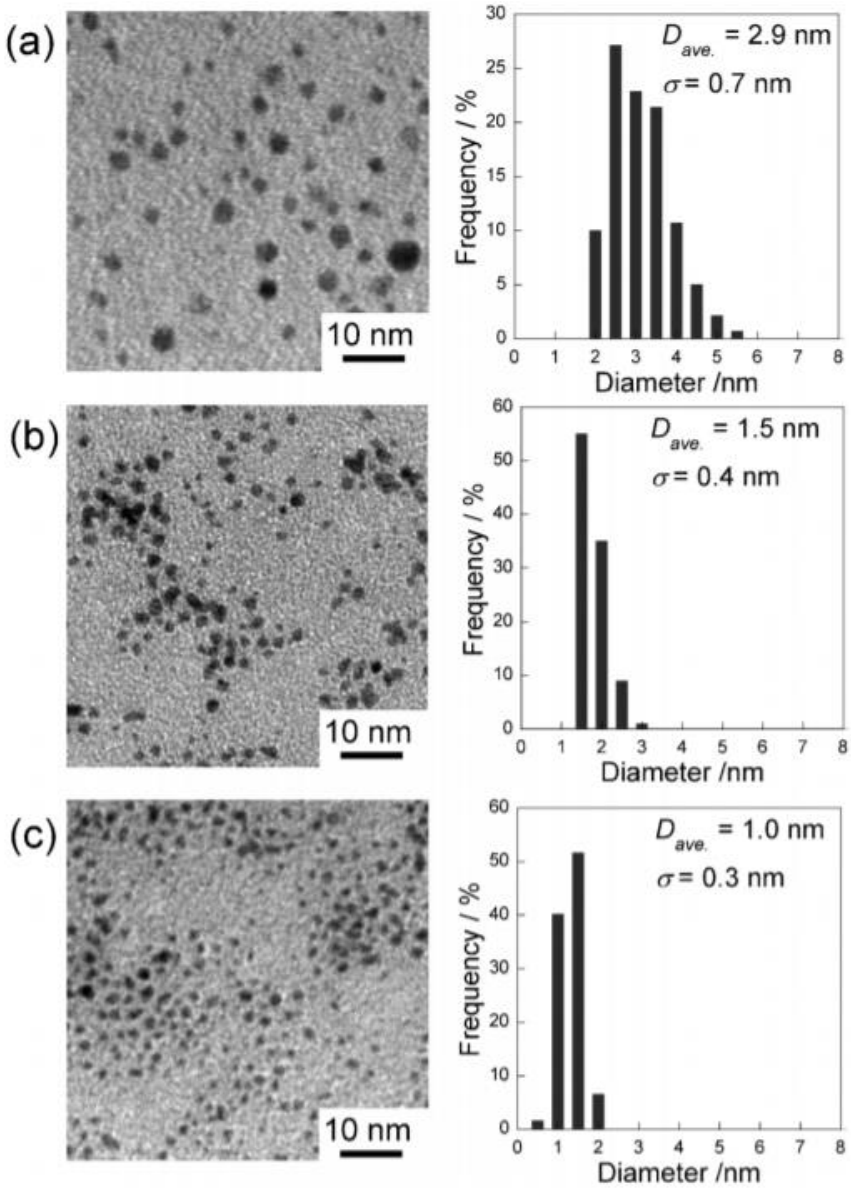

Figure 1.12 TEM images and size distributions of NPs obtained by sputter deposition on TMPA-TFSA: (a) Au NPs (f_{Au} = 1.0), (b) AuPt NPs (f_{Au} =0.33), and (c) Pt NPs (f_{Au} = 0).

Reproduced with permission from ref 66. Copyright 2012 RSC Publishing.

1.7 Growth and formation mechanism

As mentioned previously, it is accepted that there occur no considerable

collisions between the sputtered species in the gas phase at low gas pressures.[54-55] Thus, particle growth mainly occurs in the liquid phase. For sputtering onto solid substrate, there are many researchers have studied the growth mechanism, for example, Ramalingam et al. investigated the NP growth during sputtering onto solid substrate by varying the target angle, power, and time (Figure 1.9). It was shown that, with time, nucleation dependent growth dominates first, and then which is replaced by diffusion and coalescence based growth, finally agglomeration occurrs.[90] Andreazza et al also studied the nucleation and coalescence island mechanisms of Pt by sputtering onto solid substrate.[91] The results showed that the nucleation and islands growth of Pt have been followed from an early stage through to complete substrate coverage.

For sputtering onto liquid, there are two kinds of growth mechanisms: growth during sputtering and after sputtering. As for the growth during sputtering, there are three possible growth mechanisms[99] (Figure 1.13) after particles land on a liquid surface during vacuum sputtering onto a liquid-particle collision, aggregation, and growth on the liquid surface; these NPs then fall into the bulk liquid and are stabilized. Alternatively, particles can fall into the bulk of the liquid without collision and grow on the liquid surface; however, collision and growth occur inside the bulk liquid. In another mechanism, particles grow both on the liquid surface and inside the bulk liquid.

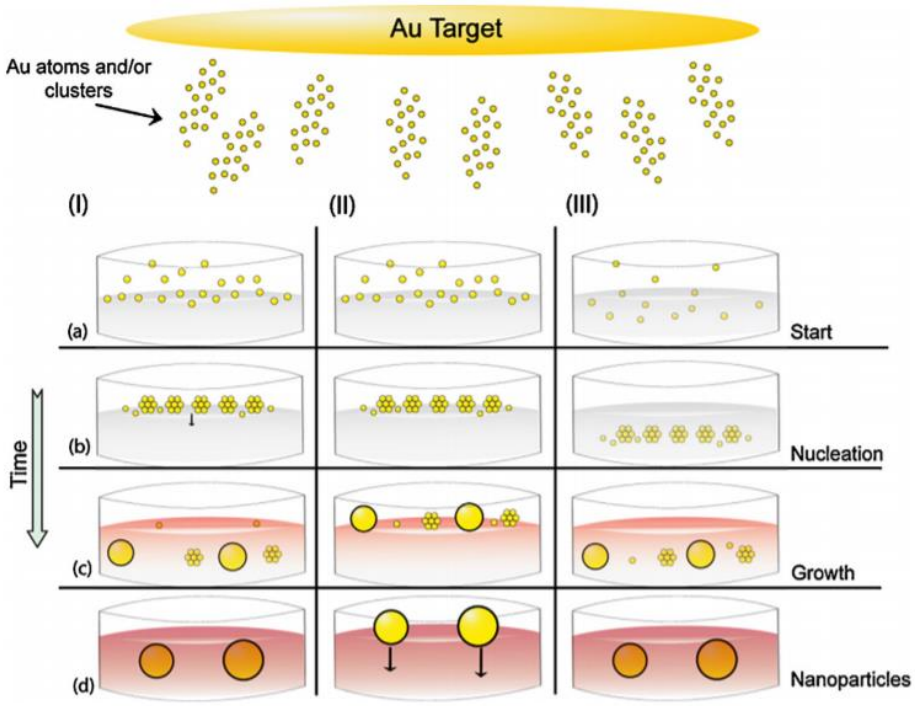

Figure 1.13 Possible mechanisms for the nucleation and growth of sputtered gold NPs into ILs.

Reproduced with permission from ref 99. Copyright 2010 American Chemical Society.

Parameters pertaining to the liquid, such as the surface tension, viscosity, temperature, and functional groups, interaction between liquid and metal NPs (Figure 1.14),[63] determine the major growth mechanism. For example, Carette et al. reported that compared with sputtering onto pentaerythritol ethoxylate (PEEL), an organic oil, spherical and crystallized Ag NPs were obtained by sputtering onto ionic liquid (IL), which may be explained by the stronger interaction between the IL molecules and the Ag atoms compared with that of PEEL molecule and Ag atoms. This situation enables the growth of Ag NP inside the homogeneous IL solution.[63] Nishikawa's group published a recent study in which the influence of conditions such as sputtering

discharge current, discharge voltage, target-substrate distance, sputtering time and target temperature on particle size were investigated. They concluded that the temperature of the target and the applied voltages have a strong effect on the size of the Au NPs generated by sputtering onto IL liquid (BMI·BF_4), while the argon pressure, target-substrate distance, discharge current, and sputtering time have little or no influence on particle size.[56] They stated that low liquid, low target temperatures, and high applied voltages are desired to generate smaller particles. Wender et al. pointed out that both nucleation and growth of Au NPs occurred on the surfaces of several ionic liquids.[54] It was reported that the growth of Au NPs occurred on the liquid surface of castor oil at a low sputtering power and inside the liquid at a high sputtering power. Vanecht et al. reported evidence that Au NPs grow inside the ionic liquids and the growth was regulated by the viscosity of liquid as the particle sizes have a linear relationship with the viscosity.[55] Carette et al. pointed out that Ag NPs grow inside ionic liquids after observing that chemical interactions between 1-butyl-3-methylimidazolium bis(trifluoromethylsulfonyl)-imide ([BMIM][TFSI]) molecules and Ag atoms are highly favored.[63] However, other studies reported that Au NPs grow on the surface as well as in the bulk of an ionic liquid; this result was postulated based on the observation that small Au NPs were obtained with ionic liquids of low surface tension and viscosity.[64] Wender and coworkers showed that the formation of NPs or thin-films depended on the discharge voltages and the surface coordination ability of the different liquid used. Low applied voltages and/or low coordinating oils led to the formation of a thin films. Meanwhile, the opposite led to

the formation of NPs. Figure 1.15 shows the scheme proposed.[100] Hatakeyama et al. showed that increasing the temperature of polyethylene glycol (PEG) used as the liquid substrate for the sputtering of an Au target led to the formation of large Au NPs; they demonstrated that the growth of Au NPs in PEG was controlled by the diffusive velocity of the sputtered particles.[69]

As for the growth after sputtering, Binnemans and coworkers are the only researchers who studied the growth of the Au NPs after sputter deposition, i.e., as a second step (Figure 1.16).[55, 101] They pointed out that Au NPs grow by consuming primary clusters and then aggregated with each other, finally precipitation occurred. However, they conducted the sputter deposition over very short time periods (~60 s) onto large volumes of IL (~4 mL). In this case, the Au concentration is considerably different from the other cases presented.[64, 84, 99] And the growth of different metal NPs may be different due to the different chemical interactions between metal atom and liquid molecule, the growth process of Pt NPs in liquid polymer has not been addressed yet.

As far as we know, there is no study on the formation mechanism of alloy NPs in co-sputtering system has been reported.

The exact growth mechanism of NPs and formation mechanism of alloy NPs in co-sputtering system are still a subject of discussion, especially the growth and alloy formation mechanism of NPs in liquid polymers.

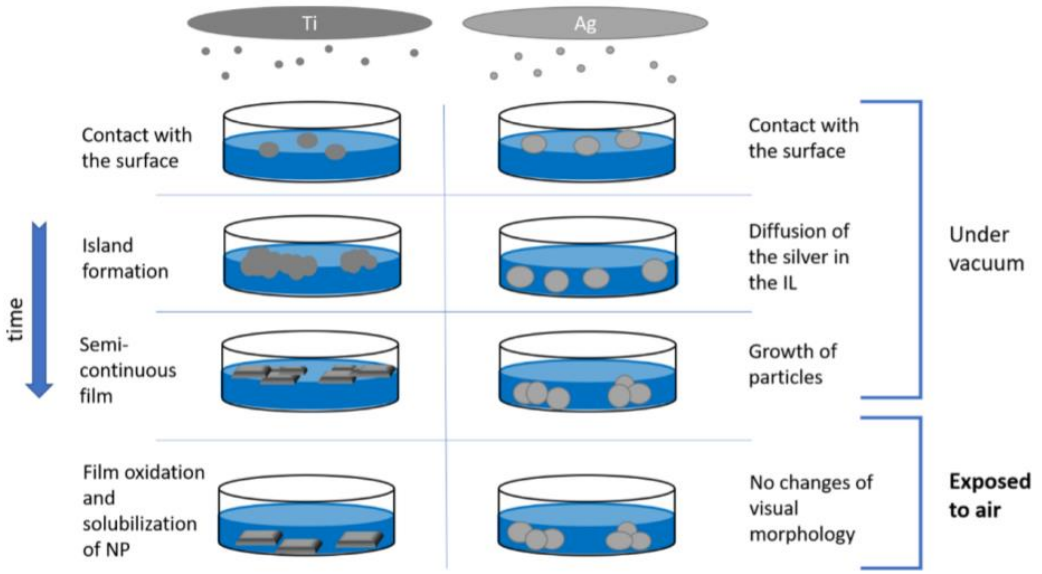

Figure 1.14 Schematic mechanism for sputtering of titanium onto PEEL (left-hand side) and silver into BMIMTFSI (right-hand side).

Reproduced with permission from ref 63. Copyright 2018 American Chemical Society.

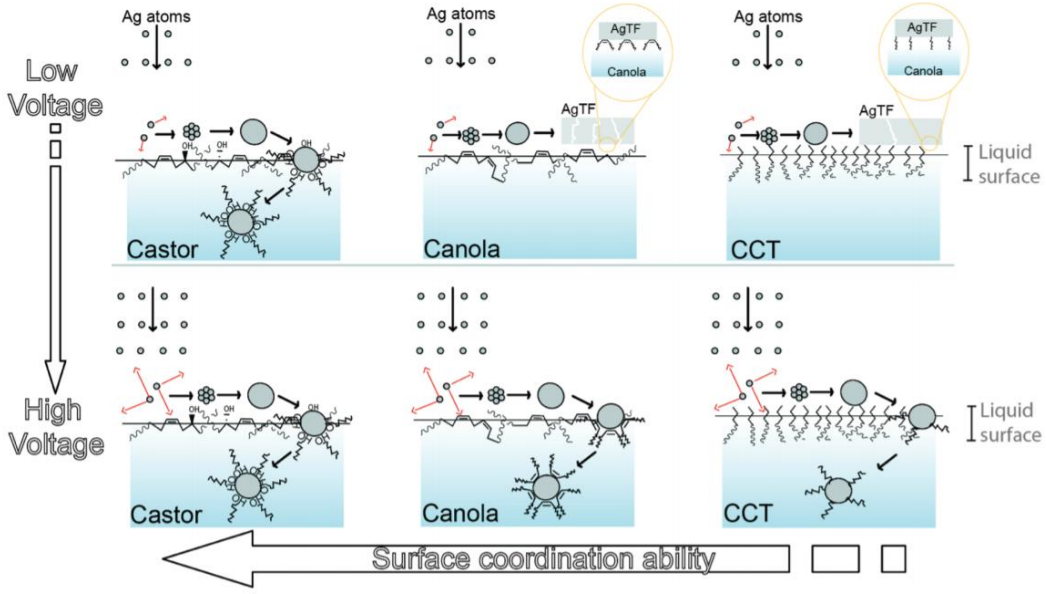

Figure 1.15 Schematic illustration for the formation of AgNPs or AgTFs by sputtering deposition of Ag onto liquids.

Reproduced with permission from ref 100. Copyright 2011 American Chemical Society.

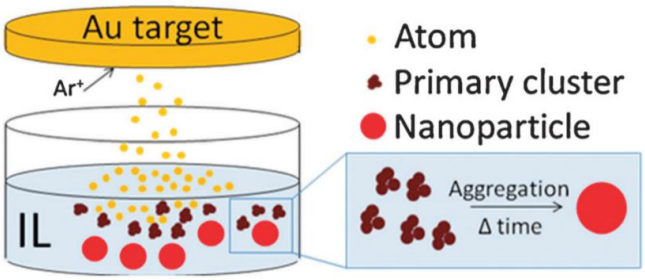

Figure 1.16 Scheme of the growth mechanism of gold nanoparticles after sputter deposition onto an ionic liquid.

Reproduced with permission from ref 55. Copyright 2011 RSC Publishing.

1.8 Summary and perspective

Sputtering metals onto liquids to prepare monometallic, bimetallic or even trimetallic NPs represents a new, simple, clean, and versatile way to synthesize stable colloidal NPs in many kinds of liquid medium, such as, ILs, liquid polymer, vegetable oils et al. This physical process (sputtering) excludes other chemicals, e.g. metal precursors, surfactants, reducing agents et al, during synthesis, which can influence the properties of NPs in the final products. Thus, sputtering onto liquid substrates is a very efficient method to prepare NPs with many functions. Instead of a simple sputter deposition, this technique can be performed combined with the co-sputtering various targets onto liquid, resulting in a specific composition and shape of NPs. Varying physical parameters during sputtering could allow for greater control of NP size, size distribution, shape, composition, and concentration, led to the formation of desired particle. However, the growth and formation mechanism are not yet fully understood with regard to sputtering. Future investigations must be carried out in order to

discover the mechanisms of NP growth and alloy formation. Especially the correlations of size, shape, composition, and atom concentration are rather ambiguous without systematic experimental estimation or simulation basics. Therefore, future investigation is necessary in order to fully understand the entire process.

To conclude, the possibility of synthesizing monometallic and bimetallic NPs is one of the advantages of this technique. Furthermore, sputtering is a controllable and stable process that can be used to prepare small-sized (1-10 nm) colloidal NPs. If the exact growth and formation mechanism are understood, the sputtering method will become one of the most promising in the field of nanomaterial colloidal synthesis for a variety of applications.

1.9 References

1. Mohanraj, V.; Chen, Y., Nanoparticles-a review. Tropical journal of pharmaceutical research 2006, 5 (1), 561-573.

2. Lewis, L. N., Chemical catalysis by colloids and clusters. Chemical Reviews 1993, 93 (8), 2693-2730.

3. Nicewarner-Pena, S. R.; Freeman, R. G.; Reiss, B. D.; He, L.; Peña, D. J.; Walton, I. D.; Cromer, R.; Keating, C. D.; Natan, M. J., Submicrometer metallic barcodes. Science 2001, 294 (5540), 137-141.

4. Kamat, P. V., Photophysical, photochemical and photocatalytic aspects of metal nanoparticles. ACS Publications: 2002.

5. Murray, C.; Sun, S.; Doyle, H.; Betley, T., Monodisperse 3d transition-metal (Co, Ni, Fe) nanoparticles and their assembly intonanoparticle superlattices. Mrs Bulletin 2001, 26 (12), 985-991.

6. Frey, N. A.; Sun, S., Magnetic nanoparticle for information storage applications. Inorganic Nanoparticles: Synthesis, Application, and Perspective 2010, 33-68.

7. Corpuz, R. D.; Ishida, Y.; Nguyen, M. T.; Yonezawa, T., Synthesis of Positively Charged Photoluminescent Bimetallic Au-Ag Nanoclusters by Double-Target Sputtering Method on a Biocompatible Polymer Matrix. Langmuir 2017, 33 (36), 9144-9150.

8. Corpuz, R. D.; Ishida, Y.; Yonezawa, T., Controlling an electrostatic repulsion by oppositely charged surfactants towards positively charged fluorescent gold nanoclusters. Physical Chemistry Chemical Physics 2016, 18 (13), 8773-8776.

9. Sharma, G.; Gupta, V. K.; Agarwal, S.; Kumar, A.; Thakur, S.; Pathania, D., Fabrication and characterization of Fe@ MoPO nanoparticles: ion exchange behavior and photocatalytic activity against malachite green. Journal of Molecular Liquids 2016, 219, 1137-1143.

10. Toshima, N.; Yonezawa, T., Bimetallic nanoparticles-novel materials for chemical and physical applications. New Journal of Chemistry 1998, 22 (11), 1179-1201.

11. Shankar, S. S.; Rai, A.; Ahmad, A.; Sastry, M., Rapid synthesis of Au, Ag, and bimetallic Au core-Ag shell nanoparticles using Neem (Azadirachta indica) leaf broth. Journal of colloid and interface science 2004, 275 (2), 496-502.

12. Jung, H.; King, M. E.; Personick, M. L., Strategic synergy: advances in the shape control of bimetallic nanoparticles with dilute alloyed surfaces. Current opinion in colloid & interface science 2019.

13. Ying, J.; Li, J.; Jiang, G.; Cano, Z. P.; Ma, Z.; Zhong, C.; Su, D.; Chen, Z., Metal-organic frameworks derived platinum-cobalt bimetallic nanoparticles in nitrogen-doped hollow porous carbon capsules as a highly active and durable catalyst for oxygen reduction reaction. Applied Catalysis B: Environmental 2018, 225, 496-503.

14. Sharma, G.; Kumar, A.; Sharma, S.; Naushad, M.; Dwivedi, R. P.; ALOthman, Z. A.; Mola, G. T., Novel development of nanoparticles to bimetallic nanoparticles and their composites: a review. Journal of King Saud University-Science 2017.

15. Luo, J.; Njoki, P. N.; Lin, Y.; Wang, L.; Zhong, C. J., Activity-composition

correlation of AuPt alloy nanoparticle catalysts in electrocatalytic reduction of oxygen. Electrochemistry communications 2006, 8 (4), 581-587.

16. Rauber, M.; Alber, I.; Müller, S.; Neumann, R.; Picht, O.; Roth, C.; Schökel, A.; Toimil-Molares, M. E.; Ensinger, W., Highly-ordered supportless three-dimensional nanowire networks with tunable complexity and interwire connectivity for device integration. Nano letters 2011, 11 (6), 2304-2310.

17. Shen, Q.; Jiang, L.; Zhang, H.; Min, Q.; Hou, W.; Zhu, J.-J., Three-dimensional dendritic Pt nanostructures: sonoelectrochemical synthesis and electrochemical applications. The Journal of Physical Chemistry C 2008, 112 (42), 16385-16392.

18. Manikandan, M.; Hasan, N.; Wu, H.-F., Platinum nanoparticles for the photothermal treatment of Neuro 2A cancer cells. Biomaterials 2013, 34 (23), 5833-5842.

19. Li, L.; Hu, L.; Li, J.; Wei, Z., Enhanced stability of Pt nanoparticle electrocatalysts for fuel cells. Nano Research 2015, 8 (2), 418-440.

20. Karthikeyan, B.; Murugavelu, M., Nano bimetallic Ag/Pt system as efficient opto and electrochemical sensing platform towards adenine. Sensors and Actuators B: Chemical 2012, 163 (1), 216-223.

21. Patra, S.; Yang, H., Synthesis of trimetallic Au@ Pb@ Pt core-shell nanoparticles and their electrocatalytic activity toward formic acid and methanol. Bulletin of the Korean Chemical Society 2009, 30 (7), 1485-1488.

22. Shiraishi, Y.; Sakamoto, H.; Sugano, Y.; Ichikawa, S.; Hirai, T., Pt-Cu bimetallic alloy nanoparticles supported on anatase TiO2: highly active catalysts for aerobic

oxidation driven by visible light. ACS nano 2013, 7 (10), 9287-9297.

23. Xu, Z.; Zhang, H.; Liu, S.; Zhang, B.; Zhong, H.; Su, D. S., Facile synthesis of supported Pt-Cu nanoparticles with surface enriched Pt as highly active cathode catalyst for proton exchange membrane fuel cells. international journal of hydrogen energy 2012, 37 (23), 17978-17983.

24. Jia, Y.; Su, J.; Chen, Z.; Tan, K.; Chen, Q.; Cao, Z.; Jiang, Y.; Xie, Z.; Zheng, L., Composition-tunable synthesis of Pt–Cu octahedral alloy nanocrystals from PtCu to $PtCu_3$ via underpotential-deposition-like process and their electro-catalytic properties. RSC Advances 2015, 5 (23), 18153-18158.

25. Xu, D.; Liu, Z.; Yang, H.; Liu, Q.; Zhang, J.; Fang, J.; Zou, S.; Sun, K., Solution-Based Evolution and Enhanced Methanol Oxidation Activity of Monodisperse Platinum-Copper Nanocubes. Angewandte Chemie International Edition 2009, 48 (23), 4217-4221.

26. Hernández-Fernández, P.; Rojas, S.; Ocón, P.; Gómez de La Fuente, J.; San Fabián, J.; Sanza, J.; Pena, M.; García-García, F.; Terreros, P.; Fierro, J., Influence of the preparation route of bimetallic Pt-Au nanoparticle electrocatalysts for the oxygen reduction reaction. The Journal of Physical Chemistry C 2007, 111 (7), 2913-2923.

27. Suntivich, J.; Xu, Z.; Carlton, C. E.; Kim, J.; Han, B.; Lee, S. W.; Bonnet, N. p.; Marzari, N.; Allard, L. F.; Gasteiger, H. A., Surface composition tuning of Au-Pt bimetallic nanoparticles for enhanced carbon monoxide and methanol electro-oxidation. Journal of the American Chemical Society 2013, 135 (21), 7985-7991.

28. Selvarani, G.; Selvaganesh, S. V.; Krishnamurthy, S.; Kiruthika, G.; Sridhar, P.; Pitchumani, S.; Shukla, A., A methanol-tolerant carbon-supported Pt-Au alloy cathode catalyst for direct methanol fuel cells and its evaluation by DFT. The Journal of Physical Chemistry C 2009, 113 (17), 7461-7468.

29. Maiyalagan, T.; Dong, X.; Chen, P.; Wang, X., Electrodeposited Pt on three-dimensional interconnected graphene as a free-standing electrode for fuel cell application. Journal of Materials Chemistry 2012, 22 (12), 5286-5290.

30. Toshima, N.; Wang, Y., Preparation and catalysis of novel colloidal dispersions of copper/noble metal bimetallic clusters. Langmuir 1994, 10 (12), 4574-4580.

31. Obuchi, A.; Ogata, A.; Mizuno, K.; Ohi, A.; Ohuchi, H., Properties of Pd-Au and Pt-Cu alloy surfaces for the adsorption and catalytic reduction of O_2 and NO by H_2. Colloids and Surfaces A: Physicochemical and Engineering Aspects 1993, 80 (2-3), 121-126.

32. Odenbrand, C. I.; Blanco, J.; Avila, P.; Knapp, C., Lean NO_x reduction in real diesel exhaust with copper and platinum titania based monolithic catalysts. Applied Catalysis B: Environmental 1999, 23 (1), 37-44.

33. Hu, Y.; Zhang, H.; Wu, P.; Zhang, H.; Zhou, B.; Cai, C., Bimetallic Pt-Au nanocatalysts electrochemically deposited on graphene and their electrocatalytic characteristics towards oxygen reduction and methanol oxidation. Physical Chemistry Chemical Physics 2011, 13 (9), 4083-4094.

34. Li, J.; Liang, X.; King, D. M.; Jiang, Y.-B.; Weimer, A. W., Highly dispersed Pt nanoparticle catalyst prepared by atomic layer deposition. Applied Catalysis B:

Environmental 2010, 97 (1-2), 220-226.

35. Weihua, W.; Xuelin, T.; Kai, C.; Gengyu, C., Synthesis and characterization of Pt-Cu bimetallic alloy nanoparticles by reverse micelles method. Colloids and Surfaces A: Physicochemical and Engineering Aspects 2006, 273 (1-3), 35-42.

36. Tsai, Y. W.; Tseng, Y. L.; Sarma, L. S.; Liu, D. G.; Lee, J. F.; Hwang, B. J., Genesis of Pt clusters in reverse micelles investigated by in situ X-ray absorption spectroscopy. The Journal of physical chemistry B 2004, 108 (24), 8148-8152.

37. Contreras, A. M.; Grunes, J.; Yan, X.-M.; Liddle, A.; Somorjai, G., Fabrication of platinum nanoparticles and nanowires by electron beam lithography (EBL) and nanoimprint lithography (NIL): comparison of ethylene hydrogenation kinetics. Catalysis letters 2005, 100 (3-4), 115-124.

38. Chen, J.; Lim, B.; Lee, E. P.; Xia, Y., Shape-controlled synthesis of platinum nanocrystals for catalytic and electrocatalytic applications. Nano Today 2009, 4 (1), 81-95.

39. Hui, C.; Li, X.; Hsing, I.-M., Well-dispersed surfactant-stabilized Pt/C nanocatalysts for fuel cell application: Dispersion control and surfactant removal. Electrochimica acta 2005, 51 (4), 711-719.

40. Xu, J.; Zhao, T.; Liang, Z.; Zhu, L., Facile preparation of AuPt alloy nanoparticles from organometallic complex precursor. Chemistry of Materials 2008, 20 (5), 1688-1690.

41. Gu, W.; Deng, X.; Jia, X.; Li, J.; Wang, E., Functionalized graphene/Fe 3 O 4 supported AuPt alloy as a magnetic, stable and recyclable catalyst for a catalytic

reduction reaction. Journal of Materials Chemistry A 2015, 3 (16), 8793-8799.

42. Chan-Thaw, C. E.; Chinchilla, L. E.; Campisi, S.; Botton, G. A.; Prati, L.; Dimitratos, N.; Villa, A., AuPt Alloy on TiO2: A Selective and Durable Catalyst for l-Sorbose Oxidation to 2-Keto-Gulonic Acid. ChemSusChem 2015, 8 (24), 4189-4194.

43. Wu, W.; Tang, Z.; Wang, K.; Liu, Z.; Li, L.; Chen, S., Peptide templated AuPt alloyed nanoparticles as highly efficient bi-functional electrocatalysts for both oxygen reduction reaction and hydrogen evolution reaction. Electrochimica Acta 2018, 260, 168-176.

44. Li, D.; Wang, C.; Tripkovic, D.; Sun, S.; Markovic, N. M.; Stamenkovic, V. R., Surfactant removal for colloidal nanoparticles from solution synthesis: the effect on catalytic performance. Acs Catalysis 2012, 2 (7), 1358-1362.

45. Wanjala, B. N.; Luo, J.; Fang, B.; Mott, D.; Zhong, C.-J., Gold-platinum nanoparticles: alloying and phase segregation. Journal of Materials Chemistry 2011, 21 (12), 4012-4020.

46. Bian, T.; Zhang, H.; Jiang, Y.; Jin, C.; Wu, J.; Yang, H.; Yang, D., Epitaxial growth of twinned Au-Pt core-shell star-shaped decahedra as highly durable electrocatalysts. Nano letters 2015, 15 (12), 7808-7815.

47. Grove, W. R., VII. On the electro-chemical polarity of gases. Philosophical Transactions of the Royal Society of London 1852, (142), 87-101.

48. Chelvanathan, P.; Yusoff, Y.; Haque, F.; Akhtaruzzaman, M.; Alam, M.; Alothman, Z.; Rashid, M.; Sopian, K.; Amin, N., Growth and characterization of RF-sputtered ZnS thin film deposited at various substrate temperatures for

photovoltaic application. Applied Surface Science 2015, 334, 138-144.

49. Takeda, S.; Suzuki, S.; Odaka, H.; Hosono, H., Photocatalytic TiO_2 thin film deposited onto glass by DC magnetron sputtering. Thin solid films 2001, 392 (2), 338-344.

50. Sato, H.; Minami, T.; Takata, S.; Yamada, T., Transparent conducting p-type NiO thin films prepared by magnetron sputtering. Thin solid films 1993, 236 (1-2), 27-31.

51. Kluth, O.; Schöpe, G.; Hüpkes, J.; Agashe, C.; Müller, J.; Rech, B., Modified Thornton model for magnetron sputtered zinc oxide: film structure and etching behaviour. Thin solid films 2003, 442 (1-2), 80-85.

52. Wirtz, T.; Mansilla, C.; Verdeil, C.; Migeon, H.-N., Storing Matter: A new quantitative and sensitive analytical technique based on sputtering and collection of sample material. Nuclear Instruments and Methods in Physics Research Section B: Beam Interactions with Materials and Atoms 2009, 267 (16), 2586-2588.

53. Wender, H.; Migowski, P.; Feil, A. F.; Teixeira, S. R.; Dupont, J., Sputtering deposition of nanoparticles onto liquid substrates: Recent advances and future trends. Coordination Chemistry Reviews 2013, 257 (17-18), 2468-2483.

54. Wender, H.; de Oliveira, L. F.; Feil, A. F.; Lissner, E.; Migowski, P.; Meneghetti, M. R.; Teixeira, S. R.; Dupont, J., Synthesis of gold nanoparticles in a biocompatible fluid from sputtering deposition onto castor oil. Chemical communications 2010, 46 (37), 7019-7021.

55. Vanecht, E.; Binnemans, K.; Seo, J. W.; Stappers, L.; Fransaer, J., Growth of sputter-deposited gold nanoparticles in ionic liquids. Physical Chemistry Chemical

Physics 2011, 13 (30), 13565-13571.

56. Hatakeyama, Y.; Onishi, K.; Nishikawa, K., Effects of sputtering conditions on formation of gold nanoparticles in sputter deposition technique. RSC Advances 2011, 1 (9), 1815-1821.

57. Deng, L.; Nguyen, M. T.; Mei, S.; Tokunaga, T.; Kudo, M.; Matsumura, S.; Yonezawa, T., Preparation and growth mechanism of Pt/Cu alloy nanoparticles by sputter deposition onto a liquid polymer. Langmuir 2019, 35, 8418-8427.

58. Wasa, K.; Hayakawa, S., Handbook of sputter deposition technology. 1992.

59. Brown, B.; Wolter, S. D.; Stoner, B. R.; Glass, J. T., Alloying effects of cosputtered gold-platinum thin films on the oxygen reduction reaction in acidic electrolyte. Journal of the Electrochemical Society 2008, 155 (8), B852-B859.

60. Zhao, J.; Baibuz, E.; Vernieres, J.; Grammatikopoulos, P.; Jansson, V.; Nagel, M.; Steinhauer, S.; Sowwan, M.; Kuronen, A.; Nordlund, K., Formation mechanism of Fe nanocubes by magnetron sputtering inert gas condensation. ACS nano 2016, 10 (4), 4684-4694.

61. Sugioka, D.; Kameyama, T.; Kuwabata, S.; Yamamoto, T.; Torimoto, T., Formation of a Pt-Decorated Au Nanoparticle Monolayer Floating on an Ionic Liquid by the Ionic Liquid/Metal Sputtering Method and Tunable Electrocatalytic Activities of the Resulting Monolayer. ACS applied materials & interfaces 2016, 8 (17), 10874-10883.

62. König, D.; Richter, K.; Siegel, A.; Mudring, A. V.; Ludwig, A., High-Throughput Fabrication of Au-Cu Nanoparticle Libraries by Combinatorial Sputtering in Ionic

Liquids. Advanced Functional Materials 2014, 24 (14), 2049-2056.

63. Carette, X.; Debièvre, B.; Cornil, D.; Cornil, J. r. m.; Leclère, P.; Maes, B.; Gautier, N.; Gautron, E.; El Mel, A.-A.; Raquez, J.-M., On the Sputtering of Titanium and Silver onto Liquids, Discussing the Formation of Nanoparticles. The Journal of Physical Chemistry C 2018, 122 (46), 26605-26612.

64. Hatakeyama, Y.; Okamoto, M.; Torimoto, T.; Kuwabata, S.; Nishikawa, K., Small-angle X-ray scattering study of Au nanoparticles dispersed in the ionic liquids 1-alkyl-3-methylimidazolium tetrafluoroborate. The Journal of Physical Chemistry C 2009, 113 (10), 3917-3922.

65. Okazaki, K.-i.; Kiyama, T.; Hirahara, K.; Tanaka, N.; Kuwabata, S.; Torimoto, T., Single-step synthesis of gold-silver alloy nanoparticles in ionic liquids by a sputter deposition technique. Chemical Communications 2008, (6), 691-693.

66. Suzuki, S.; Suzuki, T.; Tomita, Y.; Hirano, M.; Okazaki, K.-i.; Kuwabata, S.; Torimoto, T., Compositional control of AuPt nanoparticles synthesized in ionic liquids by the sputter deposition technique. CrystEngComm 2012, 14 (15), 4922-4926.

67. Suzuki, S.; Tomita, Y.; Kuwabata, S.; Torimoto, T., Synthesis of alloy AuCu nanoparticles with the L1 0 structure in an ionic liquid using sputter deposition. Dalton Transactions 2015, 44 (9), 4186-4194.

68. Hirano, M.; Enokida, K.; Okazaki, K.-i.; Kuwabata, S.; Yoshida, H.; Torimoto, T., Composition-dependent electrocatalytic activity of AuPd alloy nanoparticles prepared via simultaneous sputter deposition into an ionic liquid. Physical Chemistry Chemical

Physics 2013, 15 (19), 7286-7294.

69. Hatakeyama, Y.; Morita, T.; Takahashi, S.; Onishi, K.; Nishikawa, K., Synthesis of gold nanoparticles in liquid polyethylene glycol by sputter deposition and temperature effects on their size and shape. The Journal of Physical Chemistry C 2011, 115 (8), 3279-3285.

70. Nguyen, M. T.; Yonezawa, T.; Wang, Y.; Tokunaga, T., Double target sputtering into liquid: A new approach for preparation of Ag-Au alloy nanoparticles. Materials Letters 2016, 171, 75-78.

71. Nguyen, M. T.; Zhang, H.; Deng, L.; Tokunaga, T.; Yonezawa, T., Au/Cu bimetallic nanoparticles via double-target sputtering onto a liquid polymer. Langmuir 2017, 33 (43), 12389-12397.

72. Ishida, Y.; Nakabayashi, R.; Matsubara, M.; Yonezawa, T., Silver sputtering into a liquid matrix containing mercaptans: the systematic size control of silver nanoparticles in single nanometer-orders. New journal of chemistry 2015, 39 (6), 4227-4230.

73. Sumi, T.; Motono, S.; Ishida, Y.; Shirahata, N.; Yonezawa, T., Formation and optical properties of fluorescent gold nanoparticles obtained by matrix sputtering method with volatile mercaptan molecules in the vacuum chamber and consideration of their structures. Langmuir 2015, 31 (14), 4323-4329.

74. Deng, L.; Nguyen, M. T.; Yonezawa, T., Sub-2 nm single-crystal Pt nanoparticles via sputtering onto a liquid polymer. Langmuir 2018, 34 (8), 2876-2881.

75. Chung, M. W.; Cha, I. Y.; Ha, M. G.; Na, Y.; Hwang, J.; Ham, H. C.; Kim, H.-J.;

Henkensmeier, D.; Yoo, S. J.; Kim, J. Y., Enhanced CO2 reduction activity of polyethylene glycol-modified Au nanoparticles prepared via liquid medium sputtering. Applied Catalysis B: Environmental 2018, 237, 673-680.

76. Ishida, Y.; Sumi, T.; Yonezawa, T., Sputtering synthesis and optical investigation of octadecanethiol-protected fluorescent Au nanoparticles. New Journal of Chemistry 2015, 39 (8), 5895-5897.

77. Ye, G.-x.; Zhang, Q.-r.; Feng, C.-m.; Ge, H.-l.; Jiao, Z.-k., Structural and electrical properties of a metallic rough-thin-film system deposited on liquid substrates. Physical Review B 1996, 54 (20), 14754.

78. Ge, H.; Feng, C.; Ye, G.; Ren, Y.; Jiao, Z., Growth mechanism and electrical properties of metallic films deposited on silicone oil surfaces. Journal of applied physics 1997, 82 (11), 5469-5471.

79. Ye, G.-X.; Michely, T.; Weidenhof, V.; Friedrich, I.; Wuttig, M., Nucleation, growth, and aggregation of Ag clusters on liquid surfaces. Physical review letters 1998, 81 (3), 622.

80. Quan-Lin, Y.; Sen-Jiang, Y.; Jin-Sheng, J.; Gao-Xiang, Y., Formation mechanism and orderly structures of an iron film system deposited on silicone oil surfaces. Chinese physics letters 2003, 20 (7), 1109.

81. Xu, X.-J.; Ye, Q.-L.; Ye, G.-X., Temperature dependence of coercivity behavior in iron films on silicone oil surfaces. Physics Letters A 2007, 361 (4-5), 429-433.

82. Zhang, Y.-J.; Yu, S.-J., Experimental observations of disk-shaped patterns in Fe films sputtering deposited on silicone oil surfaces. International Journal of Modern

Physics B 2009, 23 (14), 3147-3157.

83. Wagener, M.; Günther, B., Sputtering on liquids-a versatile process for the production of magnetic suspensions? Journal of Magnetism and Magnetic Materials 1999, 201 (1-3), 41-44.

84. Torimoto, T.; Okazaki, K.-i.; Kiyama, T.; Hirahara, K.; Tanaka, N.; Kuwabata, S., Sputter deposition onto ionic liquids: Simple and clean synthesis of highly dispersed ultrafine metal nanoparticles. Applied physics letters 2006, 89 (24), 243117.

85. Liu, C.; Cai, X.; Wang, J.; Liu, J.; Riese, A.; Chen, Z.; Sun, X.; Wang, S.-D., One-step synthesis of AuPd alloy nanoparticles on graphene as a stable catalyst for ethanol electro-oxidation. international journal of hydrogen energy 2016, 41 (31), 13476-13484.

86. Ishida, Y.; Akita, I.; Sumi, T.; Matsubara, M.; Yonezawa, T., Thiolate-protected gold nanoparticles via physical approach: unusual structural and photophysical characteristics. Scientific reports 2016, 6, 29928.

87. Rioux, R.; Song, H.; Hoefelmeyer, J.; Yang, P.; Somorjai, G., High-surface-area catalyst design: synthesis, characterization, and reaction studies of platinum nanoparticles in mesoporous SBA-15 silica. The Journal of Physical Chemistry B 2005, 109 (6), 2192-2202.

88. Kou, R.; Shao, Y.; Wang, D.; Engelhard, M. H.; Kwak, J. H.; Wang, J.; Viswanathan, V. V.; Wang, C.; Lin, Y.; Wang, Y., Enhanced activity and stability of Pt catalysts on functionalized graphene sheets for electrocatalytic oxygen reduction. Electrochemistry Communications 2009, 11 (5), 954-957.

89. Wang, Y.; Ren, J.; Deng, K.; Gui, L.; Tang, Y., Preparation of tractable platinum, rhodium, and ruthenium nanoclusters with small particle size in organic media. Chemistry of Materials 2000, 12 (6), 1622-1627.

90. Ramalingam, B.; Mukherjee, S.; Mathai, C. J.; Gangopadhyay, K.; Gangopadhyay, S., Sub-2 nm size and density tunable platinum nanoparticles using room temperature tilted-target sputtering. Nanotechnology 2013, 24 (20), 205602.

91. Andreazza, P.; Andreazza-Vignolle, C.; Rozenbaum, J.; Thomann, A.-L.; Brault, P., Nucleation and initial growth of platinum islands by plasma sputter deposition. Surface and Coatings Technology 2002, 151, 122-127.

92. Yoshii, K.; Tsuda, T.; Arimura, T.; Imanishi, A.; Torimoto, T.; Kuwabata, S., Platinum nanoparticle immobilization onto carbon nanotubes using Pt-sputtered room-temperature ionic liquid. RSC Advances 2012, 2 (22), 8262-8264.

93. Staszek, M.; Siegel, J.; Kolářová, K.; Rimpelová, S.; Švorčík, V., Formation and antibacterial action of Pt and Pd nanoparticles sputtered into liquid. Micro & Nano Letters 2014, 9 (11), 778-781.

94. Hu, X.; Takai, O.; Saito, N., Simple synthesis of platinum nanoparticles by plasma sputtering in water. Japanese Journal of Applied Physics 2013, 52 (1S), 01AN05.

95. Yoshii, K.; Tsuda, T.; Torimoto, T.; Kuwabata, S., Carbon composite with Pt nanoparticles prepared by Room-temperature ionic liquid-sputtering method. ECS Transactions 2010, 33 (7), 127-133.

96. Tsuda, T.; Kurihara, T.; Hoshino, Y.; Kiyama, T.; Okazaki, K.-i.; Torimoto, T.;

Kuwabata, S., Electrocatalytic activity of platinum nanoparticles synthesized by room-temperature ionic liquid-sputtering method. Electrochemistry 2009, 77 (8), 693-695.

97. Cha, I. Y.; Ahn, M.; Yoo, S. J.; Sung, Y.-E., Facile synthesis of carbon supported metal nanoparticles via sputtering onto a liquid substrate and their electrochemical application. RSC Advances 2014, 4 (73), 38575-38580.

98. Farsinezhad, S.; Sharma, H.; Shankar, K., Interfacial band alignment for photocatalytic charge separation in TiO_2 nanotube arrays coated with CuPt nanoparticles. Physical Chemistry Chemical Physics 2015, 17 (44), 29723-29733.

99. Wender, H.; de Oliveira, L. F.; Migowski, P.; Feil, A. F.; Lissner, E.; Prechtl, M. H.; Teixeira, S. R.; Dupont, J., Ionic liquid surface composition controls the size of gold nanoparticles prepared by sputtering deposition. The Journal of Physical Chemistry C 2010, 114 (27), 11764-11768.

100. Wender, H.; Gonçalves, R. V.; Feil, A. F.; Migowski, P.; Poletto, F. S.; Pohlmann, A. R.; Dupont, J.; Teixeira, S. R., Sputtering onto liquids: from thin films to nanoparticles. The Journal of Physical Chemistry C 2011, 115 (33), 16362-16367.

101. Vanecht, E.; Binnemans, K.; Patskovsky, S.; Meunier, M.; Seo, J. W.; Stappers, L.; Fransaer, J., Stability of sputter-deposited gold nanoparticles in imidazolium ionic liquids. Physical Chemistry Chemical Physics 2012, 14 (16), 5662-5671.

2. Pt nanoparticles prepared by single target sputtering

2.1 Introduction

Noble metal nanoparticles (NPs) can be synthesized using various synthesis methods such as chemical reduction,[1-3] photochemical reduction,[4-5] laser ablation,[6-7] sputtering,[8-10] plasma-in-liquid process[11] and so on. Among them, vacuum sputtering technique can produce atoms and clusters without using toxic reducing agents.[10] Ionized Ar gas attack metal target to eject metal atoms or small clusters. Atoms and clusters aggregate and finally form NPs. With use of a low vapor pressure liquid as a matrix in sputtering, it becomes a green technique to prepare nanoparticles dispersed in liquid. Recently, polyethylene glycol (PEG, M_W = 600) has attracted great attention as the liquid matrix for producing dispersions of metal and metal alloy nanoparticles, e.g. Au, Ag, Cu, Au/Ag, and Au/Cu alloy.[12-17] This is because PEG is non-toxic, economic and its vapor pressure is low enough[18] to make the vacuum sputtering deposition possible. In addition, PEG (M_W = 600) can stabilize nanoparticles via its high viscosity. PEG with molecular weight lower than 1000 is liquid at room temperature, while PEG with higher molecular weight is a solid with a low-melting temperature. Liquid PEG with higher molecular weight has higher viscosity. Our previous study indicated that the viscosity can influence the size of the produced Ag NPs in which too viscous liquid resulted in thin Ag film.[19] Among liquid PEGs of different M_W, we chose PEG with M_W = 600 for its molecular weight, and thus its

viscosity, in the middle range. Current progress in this field includes dissolving stabilizing agents in PEG to offer precisely control of NPs' size and properties.[13-14] In our previous studies to produce noble metal NPs such as Au, Ag, and Au/Ag alloys via sputtering onto neat PEG, we noticed that without addition of mercapto capping ligand, a large number of nanoparticles bigger than 2 nm were obtained.[15]

Platinum (Pt) NPs have been intensively investigated because of their unique catalytic,[20] and also drawn attention as sensor[21] or applied in biomedical field.[22] Considerable research efforts have been devoted to prepare Pt NPs by chemical methods[23-24] with stabilizers such as poly(vinyl pyrrolidone) (PVP),[25] 3-(N,N-dimethyldodecylammonio) propanesulfonate (SB12),[26] etc. However, removal of these stabilizers requires harsh treatment such as thermal treatment[26-27] or acid treatment.[27] On the other hand, Pt NPs have also been prepared by sputtering without stabilizers.[28-35] The effect of target angle, applied power, and sputtering time[28] and argon pressure[29] on the size and shape of Pt NPs sputtered on a solid substrate has been studied. Pt NPs obtained by sputtering onto liquid substrate have also been reported.[30-32] The effect of temperature, sputtering time[33] and kinds of working gas[34] on the particle size has been studied. An interesting approach in the use of liquid PEG containing carbon powder as matrix to prepare Pt NPs with an average size of 2 nm was described by Cha et al.[35] Small Pt NPs are highly interesting thanks to their high ratios of surface atoms and thus enhance the catalytic properties.[36-37] A handful study has prepared Pt NPs with size below 2 nm via a chemical reduction in organic media[38] while most of the reported Pt NPs sizes were larger than 2 nm. Although sub-2 nm Pt

NPs have been observed via sputtering on TEM gird,[28] size control of sub-2 nm Pt NPs sputtered onto PEG and the stability of Pt in PEG have not been addressed yet.

In the present study, we proposed using single target sputter deposition of Pt target onto PEG as the liquid matrix to prepare highly uniform Pt NPs, because the viscosity of PEG can inhibit NP growth. Pt NP sizes can be tailored by varying sputtering current in a narrow range. Particle growth and their stability in PEG have been studied via examining the particle size and structures after various storage time of the sputtered Pt NPs in PEG. We demonstrate that sub-2 nm Pt NPs have been prepared without using additional stabilizers.

2.2 Experimental section

2.2.1 Preparation of Pt nanoparticles

Before using for sputtering, polyethylene glycol (PEG, Average molecular weight 600, purchased from Junsei) was heated under vacuum condition at 80 ºC for 2 h to remove water and dissolved gases. And then PEG (10 mL) was added in a pertri dish with a diameter of 63 mmϕ. The petri dish was placed in the sputtering chamber whereas the surface of the liquid was positioned 50 mm away from the metal target. After multiple times of Ar (99.99% purity) purging and evacuation, the pressure of the chamber was set at 2 Pa with Ar as carrying gas. A mechanical stirrer was used to stir the liquid at the stirring speed of 80 rpm. Sputtering was performed for 10 min to clean the target surface prior to collect Pt NPs in PEG. Sputtering was performed with

current varied from 5 to 50 mA on a collodion coated copper TEM grid and onto PEG. Sputtering onto PEG was performed for 30 min and PEG temperature of 30 °C whereas sputtering onto grid performed for 1 and 5 s. All sputter currents used were stable during sputtering. Since various factors, e.g. temperature of liquid, gas pressure, sputtering time, sputtering current, and liquid-target distance, have effect on the size of Pt NPs prepared by sputtering, Taguchi experimental design can be used to optimize the experimental conditions.[39] Take into consideration that high sputtering temperature will decrease the viscosity of PEG thereby less stable NPs, long sputtering time will make severe particle aggregation (Figure S1) whereas too short sputtering time cannot produce enough amount of particles, we fixed the sputtering temperature and sputtering time constant at 30 °C and 30 min, respectively whereas 2 Pa is used as the optimal pressure for our device. The sputtered Pt NPs dispersed in PEG were stored at room temperature in dark for various periods of times (as synthesized to 5 months) to study the stability and particle growth after sputtering.

2.2.2 Characterization

Size, size distribution and shape of the obtained Pt NPs were analyzed by a JEOL JEM-2010 and a JEOL-2000FX transmission electron microscopy (TEM) operating at 200 kV. TEM samples were prepared by dipping the collodion-coated Cu grid in PEG contain Pt NPs, followed by taking out the grid then gently dipping it in ethanol for 7 min to dissolve PEG. Finally, the grids were dried in the air for a few minutes at room temperature. The histograms of nanoparticle size distribution were obtained by

measuring approximately 300 particles from at least 3 different regions of grid using ImageJ software. High resolution images of Pt NPs were collected on a scanning transmission electron microscope (STEM, JEOL JEM-ARM200F, 200 kV). Optical absorption spectra in UV-Vis region were obtained using a JASCO V-630 spectrophotometer using a quartz cuvette with 1 mm optical path. Samples sputtered at 5-20 mA were used to measured UV-Vis spectra without any dilution whereas samples sputtered at 30-50 mA were diluted 3 times using PEG before measuring UV-Vis spectra. Chemical state of Pt NPs was investigated by JEOL JPS-9200 X-ray photoelectron spectroscopy (XPS) device equipped with a monochromatic Mg Kα source operating at 100 W under ultrahigh vacuum (~ 5.0×10^{-7} Pa) conditions. Binding energies were referenced to the Si 2p binding energy of the Si wafer substrate. The crystalline structure of NPs was determined using X-ray diffraction (XRD, Rigaku Mini Flex II, Cu Ka). C powder and methanol were added to PEG dispersion of Pt NPs. Pt on C powder was collected by centrifugation and washed several times with methanol, then dried for XPS and XRD measurement.

2.3 Results and discussion

2.3.1 UV-vis spectra of Pt NPs dispersion of PEG

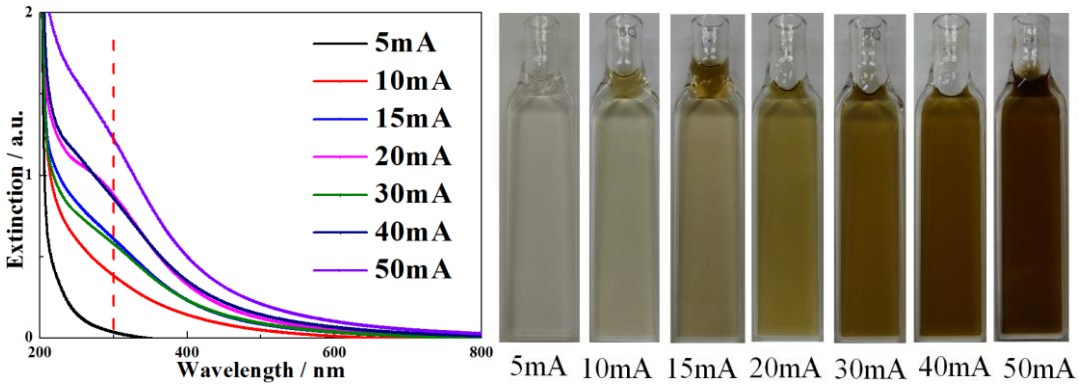

Figure 2.1 UV-Vis spectra of NPs obtained by sputter deposition onto PEG (left) and photograph of Pt NPs dispersion of PEG under room light (right) with different sputtering current.

UV-Vis spectra and photograph of Pt NPs dispersion of PEG are shown in Figure. 2.1. An absorption band between 200 and 300 nm has been reported for Pt NPs.[40] Here, UV-spectra of the sputtered Pt NPs in PEG showed an absorption around 300 nm under various sputtering current, indicating the presence of Pt NPs in PEG. Different sputtering current only changed spectrum intensity, not the absorption position, which may relate to the concentration of Pt NPs in PEG. In other words, the higher the sputter current, the more Pt NPs were produced in PEG. This is because an increase in sputtering current results in a higher sputtering rate.[10] As can be seen from the right picture of Figure 2.1, the color of the PEG containing Pt NPs changes from nearly colorless to yellow and to dark brown as the sputtering current increased from 5 to 50 mA, which indicates that the NPs concentration increased. We estimated the number of Pt NPs, $N_{Pt\ NPs}$, quantitatively based on measuring the weight of the sputtered Pt, m_{Pt} (g), average particle radius, r (m), (TEM images, shown later in

Figure 2.2), and assume the density of the Pt NPs, ρ (g/m^3), as the same as that of the bulk Pt, 21.45×10^6 g/m^3; thus $N_{Pt\ NPs}$ = ¾ m_{Pt}/(πρr^3) particles. Hence the concentration of Pt NPs in PEG (10 mL), $C_{Pt\ NPs}$, is $C_{Pt\ NPs} = N_{Pt\ NPs}/10^{-2}$ (particles/L). A circular aluminum foil with the diameter as same as the pertri dish (placed on the petri dish) was used to collect the sputtered Pt for certain time to measure the weight of Pt with high accuracy. For 30 min sputtering, 1.3 mg and 9.7 mg of Pt were obtained using sputter currents of 10 mA and 50 mA, respectively. As a result, we found that the concentrations of Pt NPs in PEG after 30 min sputtering were 8.7×10^{18} particles/L and 31.5×10^{18} particles/L under sputter current 10 mA and 50 mA, respectively.

2.3.2 TEM observations of Pt NPs

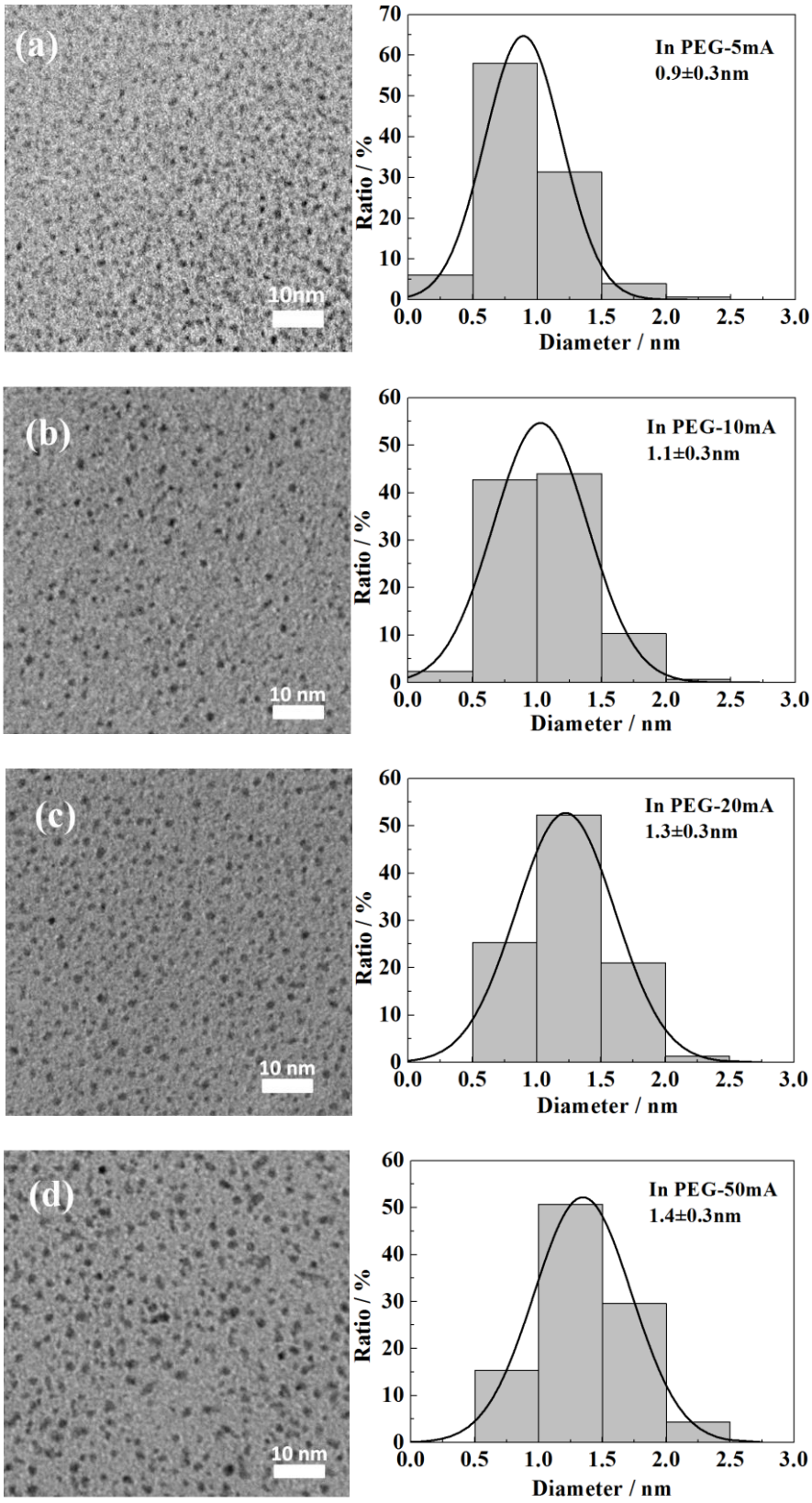

Figure 2.2 TEM images and size distributions of NPs obtained by sputtering onto PEG under sputtering current of (a) 5 mA, (b) 10 mA, (c) 20 mA, (d) 50 mA.

As can be observed in Figure 2.2, Pt particles are isolated and randomly distributed without severe agglomeration. An increase in sputtering current resulted in an increase in particles' size from 0.9 ± 0.3 nm (5 mA) to 1.3 ± 0.3 nm (20 mA). Further increase in sputter current from 20 mA to 50 mA does not change the particles' size significant, i.e. nearly constant size of 1.3 ± 0.3 nm (20-50 mA) were obtained. For all sputtered currents used, Pt NPs with narrow size distribution were observed.

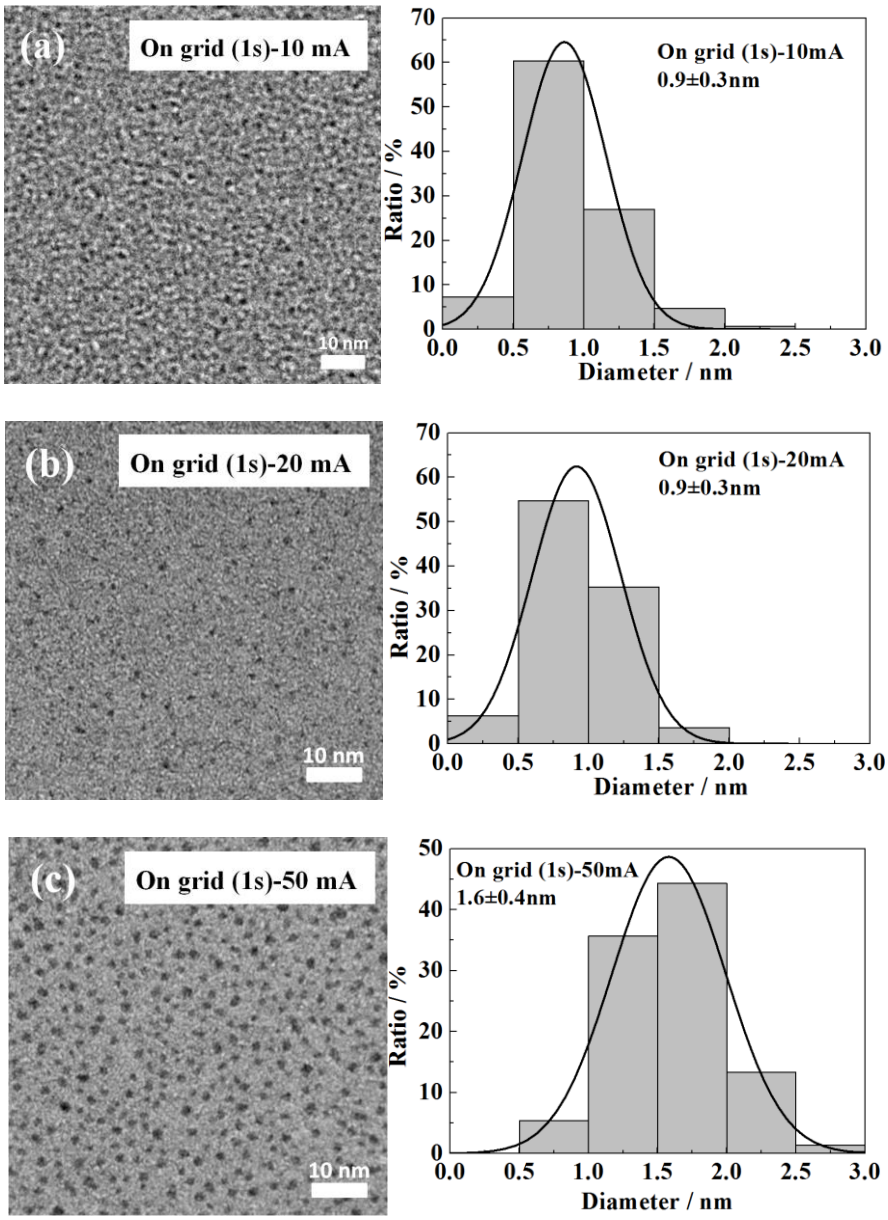

Figure 2.3 TEM images and size distributions of NPs obtained by sputtering on TEM grid for 1 s under sputtering current of (a) 10 mA, (b) 20 mA, (c) 50 mA. Sample sputtered under 5 mA was hard to observe in normal TEM.

It was known that in the sputtering chamber, the sputtered atoms can collide with each other, leads to cluster formation,[28] and then clusters aggregate on or in liquid to from NPs.[41] Increasing sputtering current leads to sputtering rate increased. Thus, it

can cause increase in the collision probability between atoms and can result in forming larger clusters and larger NPs. To investigate whether any aggregation and growth of NP occurred in PEG, we compared the particle size of as-sputtered Pt NPs in PEG and that of Pt NPs sputtered on TEM grids for 1 and 5 s. The TEM images and size distributions of Pt NPs sputtered on TEM grid for 1 s were shown in Figure 2.3. The TEM images and size distributions of Pt NPs sputtered on TEM grid for 5 s were given in Supporting information, Figure S2. The summary of the particle sizes was shown in Figure 2.4.

After 1 s sputtering on grid, particle size was constant at 0.9 ± 0.3 nm for sputter current from 10 to 20 mA, but the particles density increases from 42 × 10^3 particles/μm^2 to 47 × 10^3 particles/μm^2. This indicates that the higher the sputter current, the more the particles were sputtered and thus higher sputtering rates was obtained.[10] Then linear increase in particle size from 0.9 ± 0.3 nm to 1.6 ± 0.4 nm was observed as sputter current increased from 20 to 50 mA. On the other hand, after 5 s sputtering on grid, particle size was found linearly increase from 0.9 ± 0.2 nm to 2.7 ± 0.6 nm as sputter current increased from 5 to 50 mA. Longer sputtering time on grid, i.e. for 30 s, at low sputtering current of 20 mA resulted to severe particle agglomeration or growth in form of nanoislands (Figure S3). The increase of particle size sputtered on TEM grids by prolong sputtering time indicated that particles growth on solid surface occurred because particles on grid cannot move. These results match well with the works done by B. Ramalingam and co-authors.[28]

It was found that at sputter currents of 50 mA, Pt NPs in PEG (1.4 ± 0.3 nm,

Figure 2.2d) was slightly smaller than Pt NPs sputtered on TEM grid for 1 s (1.6 ± 0.4 nm, Figure 2.3c) and much smaller than Pt NPs sputtered on TEM grid for 5 s (2.7 ± 0.6 nm). Similar phenomenon was observed under sputter current of 40 mA. When sputter currents were of 10 - 30 mA, the sizes of Pt NPs in PEG were slightly bigger than that of Pt NPs sputtered on grid for 1 s and smaller than NPs after 5 s sputtered on TEM grid. This suggested that some aggregation or particle growth can happen in PEG during sputtering (30 min). However, based on the fact that the similar sizes of Pt NPs obtained in PEG and sputtered on TEM grid for 1 s (within 0.5 nm difference) were observed, it can be deduced that PEG can prevent the growth of NPs to some extent that significant particle growth was not occurred as observed for Pt NPs sputtered on grid for 5 s.

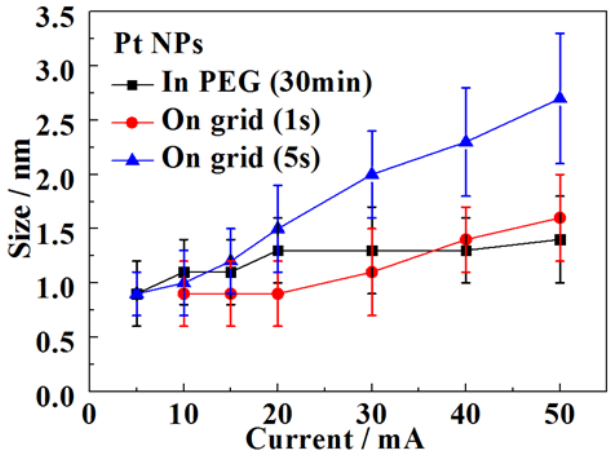

Figure 2.4 Relation between particle size and sputtering current sputtered onto PEG (black), on grid for 1 s (red) and on grid for 5 s (blue).

2.3.3 Structure and colloidal stability of Pt NPs dispersed in PEG

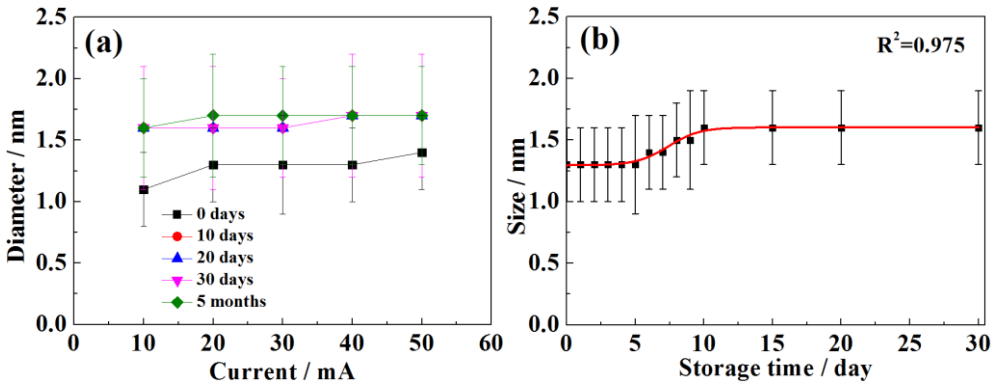

Figure 2.5 (a) Particle size of Pt NPs in PEG under various sputtering currents after 0, 10, 20, 30 days and 5 months measured by normal TEM and (b) particles size growth of Pt NPs in PEG prepared at sputter current of 20 mA.

It can be seen from Figure 2.5a that the sizes of Pt NPs (from 1.1 ± 0.3 nm to 1.4 ± 0.3 nm) prepared using different sputter currents (10 - 50 mA) are increased slightly to 1.6 ± 0.4 nm (sputter current 10 mA) and 1.7 ± 0.4 nm (sputter current 20 - 50 mA) for 10 days storage. Then the sizes did not change significantly even after keeping in the dark at room temperature for 5 months. This indicates that Pt NPs of 1.7 ± 0.4 nm were stable in PEG. Details in changes of particle size for the first 30 days of sample prepared using sputter current 20 mA was shown in Figure 2.5b. In contrast with slightly change in size of Pt NPs, PEG dispersion of Au NPs showed color change from dark red to red-purple after a week, indicating large size Au NPs formed.[12] Along with the increase in particles size, it was observed that the absorption intensity in UV-Vis spectra (Figures 2.6a and b) decreased in the short wavelength, i.e. 240-360 nm, with longer storage time and finally the absorption shoulder disappear,

indicating the growth of the Pt NPs. The XPS spectra of as-prepared sample (20 mA, 30 min, sputtered onto PEG) and 7 months stored one were quite similar (Figure S4). After 7 months storage, the surface atomic percentage of Pt(0) slightly decreased. In addition, we noticed that the lattice fringe of metallic Pt of the stored sample still appeared for entire a particle after 1 month storage (show later). Hence, the partial oxidation of Pt may not occur significantly in 1 month storage in which the UV-Vis shoulder in 240-360 nm disappeared. Thus, we think that the chemical changes of Pt could occur to some extent and could somewhat contribute but not the main contribution to the change in surface plasmon band of Pt as observed in UV-Vis spectra. Slightly increased in absorption intensity of UV-Vis spectra for the longer wavelength (740-790 nm) in the first 7 days of storage was observed and then it fluctuated within the experimental errors (Figure 2.6c). This indicates that minor aggregation can occur in PEG. These results were in good consistent with the TEM observation.

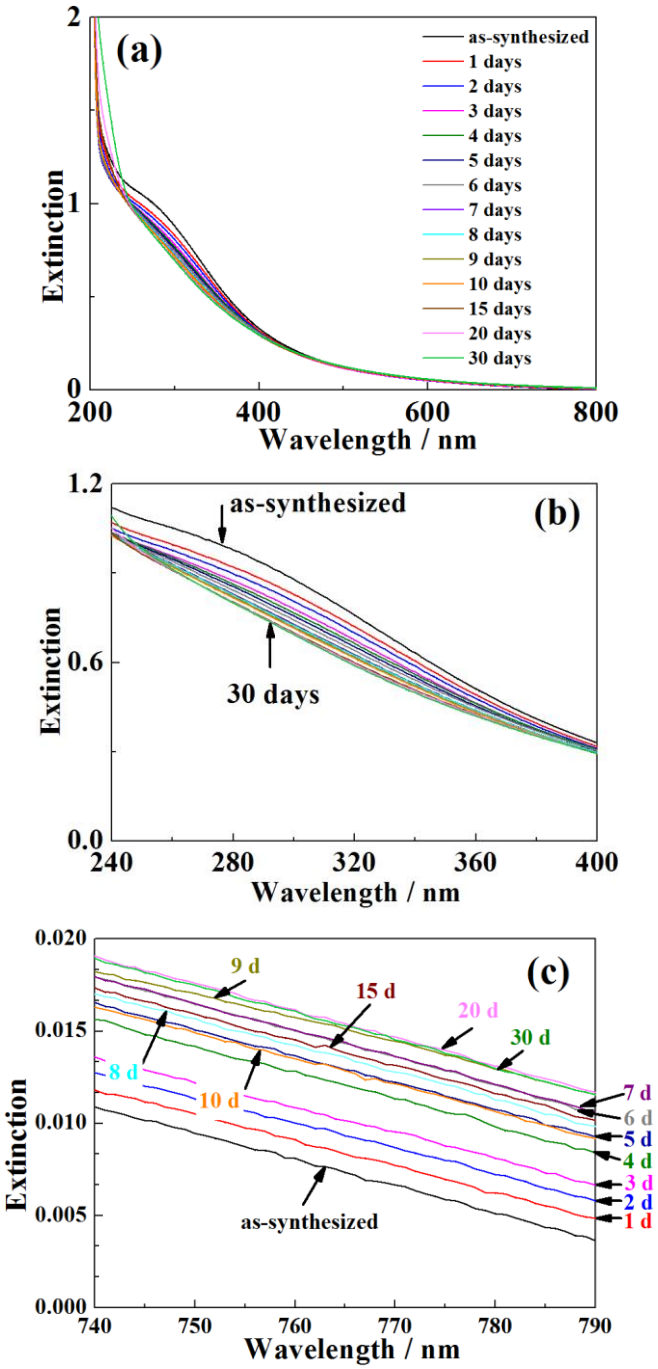

Figure 2.6 (a) UV-vis spectra of Pt NPs in PEG sputtered at 20 mA for as-synthesized and storage samples after keeping for 0-30 days and magnified pictures of UV-Vis spectra shown in (a) for (b) low wavelength and (c) higher wavelength region.

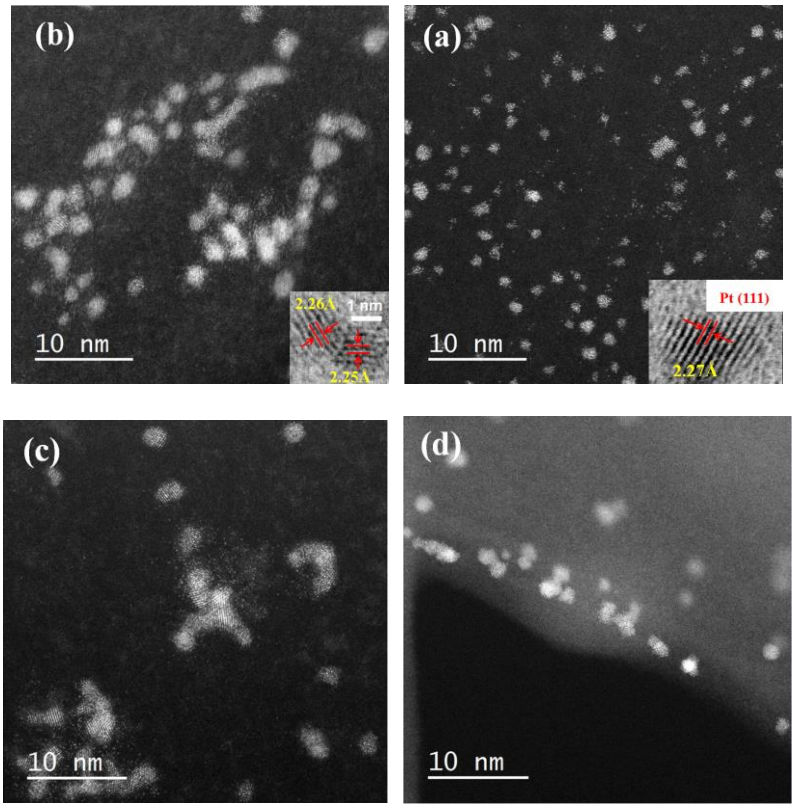

Figure 2.7 STEM-HAADF images of as-sputtered Pt NPs in PEG (a) and Pt NPs in PEG after 30 days (b), 43 days (c), and 50 days (d) stored under room temperature in dark under the sputtering current of 20 mA. TEM images of Pt NPs sputtered on grid for 1s, 5s and 30s under the sputtering current of 20 mA were given in Figure 2.3b, Figure S2, and S3 respectively.

Figures 2.7a and b are the STEM HAADF images of as-synthesized Pt sputtered at 20 mA and that after keeping for 30 days. After 30 days, the particle size slightly increased, around 0.4 nm. The inset in Figure 2.7a is a HRTEM image, which shows the lattice fringe of Pt NPs. The lattice fringe spacing of 2.27 Å was observed, corresponding to (111) plane of Pt.[42] It can be seen that the lattice fringes of Pt NP appeared across the whole particle, indicating that Pt NPs were entirely single

crystalline. And most of the produced Pt NPs are in single cluster form, not the aggregation of several clusters. XRD patterns confirmed the crystalline structure of the as-synthesized Pt where the line broadening is due to the small particle size (Figure S5). After keeping for 30 days, NP composed of some aggregated clusters were observed as shown in the inset (Figure 2.7b). Further, we noticed in HAADF images (Figure 2.7) that the number of free Pt atoms in PEG decreases with increasing of storage time. As previously shown in Figure 2.5, after 10 days of storage, the particle size of Pt sputtered at various currents was stable at 1.6 ± 0.3 nm (sputter current 10 mA) and 1.7 ± 0.4 nm (sputter current 20-50 mA) and exhibited almost no change as measured by normal TEM (Figure S6). It is noted that the normal TEM could not capture the present of Pt atoms as shown in HAADF dark field images (Figure 2.7). Therefore, the above results suggested that with time the free Pt atoms in PEG collided with Pt NPs or with themselves, thus contributed to the growth of the Pt NPs. Thus, running out free Pt atoms after sometime will lead to the stable size of Pt NPs (1.7 ± 0.4 nm) in PEG. Besides, we did not rule out the collision of Pt NPs with each other. This could occur and result to the polycrystal Pt NPs (aggregation of Pt NPs) as shown in the inset of Figures 2.7b, c, and d.

2.4 Conclusions

The results indicated that we can prepare highly uniform Pt NPs with size below 2.0 nm and narrow size distributions. Particle sizes were tailorable by varying the

sputtering current (5-50 mA) whereas negligible particle aggregation occurred in PEG during sputtering. Our finding showed that after 10 days, Pt NPs were slightly increased, of ca. 0.3~0.5 nm, in sizes due to the addition of free Pt atoms to the existing Pt NPs in PEG. Pt NPs were stable in PEG after 5 months with negligible particle aggregation, indicating the polymer matrix effectively stabilize NPs.

2.5 References

1. Dang, T. M. D.; Le, T. T. T.; Fribourg-Blanc, E.; Dang, M. C., Synthesis and optical properties of copper nanoparticles prepared by a chemical reduction method. Adv. Nat. Sci.: Nanosci. Nanotechno. 2011, 2 (1), 015009.

2. Tan, Y.; Dai, X.; Li, Y.; Zhu, D., Preparation of gold, platinum, palladium and silver nanoparticles by the reduction of their salts with a weak reductant-potassium bitartrate. J. Mater. Chem. 2003, 13 (5), 1069-1075.

3. Toshima, N.; Yonezawa, T., Bimetallic nanoparticles-novel materials for chemical and physical applications. New J. Chem. 1998, 22 (11), 1179-1201.

4. Eustis, S.; Hsu, H.-Y.; El-Sayed, M. A., Gold nanoparticle formation from photochemical reduction of Au^{3+} by continuous excitation in colloidal solutions. A proposed molecular mechanism. J. Phys. Chem. B 2005, 109 (11), 4811-4815.

5. Elsupikhe, R. F.; Ahmad, M. B.; Shameli, K.; Ibrahim, N. A.; Zainuddin, N., Photochemical reduction as a green method for the synthesis and size control of silver nanoparticles in κ-carrageenan. IEEE Trans. Nanotechno. 2016, 15 (2), 209-213.

6. Scaramuzza, S.; Zerbetto, M.; Amendola, V., Synthesis of gold nanoparticles in liquid environment by laser ablation with geometrically confined configurations: insights to improve size control and productivity. J. Phys. Chem. C 2016, 120 (17), 9453-9463.

7. Scaramuzza, S.; Agnoli, S.; Amendola, V., Metastable alloy nanoparticles, metal-oxide nanocrescents and nanoshells generated by laser ablation in liquid solution: influence of the chemical environment on structure and composition. Phys.

Chem. Chem. Phys. 2015, 17 (42), 28076-28087.

8. Torimoto, T.; Okazaki, K.-i.; Kiyama, T.; Hirahara, K.; Tanaka, N.; Kuwabata, S., Sputter deposition onto ionic liquids: Simple and clean synthesis of highly dispersed ultrafine metal nanoparticles. Appl. Phys. Lett. 2006, 89 (24), 243117.

9. Acsente, T.; Negrea, R.; Nistor, L.; Matei, E.; Grisolia, C.; Birjega, R.; Dinescu, G., Tungsten nanoparticles with controlled shape and crystallinity obtained by magnetron sputtering and gas aggregation. Mater. Lett. 2017, 200, 121-124.

10. Wender, H.; Migowski, P.; Feil, A. F.; Teixeira, S. R.; Dupont, J., Sputtering deposition of nanoparticles onto liquid substrates: Recent advances and future trends. Coordin. Chem. Rev. 2013, 257 (17), 2468-2483.

11. Čempel, D.; Nguyen, M. T.; Ishida, Y.; Tsukamoto, H.; Shirai, H.; Wang, Y.; Wu, K. C.-W.; Yonezwa, T., Au Nanoparticles Prepared Using a Coated Electrode in Plasma-in-Liquid Process: Effect of the Solution pH. J. Nanosci. Nanotechno. 2016, 16 (9), 9257-9262.

12. Hatakeyama, Y.; Morita, T.; Takahashi, S.; Onishi, K.; Nishikawa, K., Synthesis of gold nanoparticles in liquid polyethylene glycol by sputter deposition and temperature effects on their size and shape. J.Phys. Chem. C 2011, 115 (8), 3279-3285.

13. Ishida, Y.; Nakabayashi, R.; Matsubara, M.; Yonezawa, T., Silver sputtering into a liquid matrix containing mercaptans: the systematic size control of silver nanoparticles in single nanometer-orders. New J. Chem. 2015, 39 (6), 4227-4230.

14. Sumi, T.; Motono, S.; Ishida, Y.; Shirahata, N.; Yonezawa, T., Formation and

optical properties of fluorescent gold nanoparticles obtained by matrix sputtering method with volatile mercaptan molecules in the vacuum chamber and consideration of their structures. Langmuir 2015, 31 (14), 4323-4329.

15. Nguyen, M. T.; Yonezawa, T.; Wang, Y.; Tokunaga, T., Double target sputtering into liquid: A new approach for preparation of Ag–Au alloy nanoparticles. Mater. Lett. 2016, 171, 75-78.

16. Corpuz, R. D.; Ishida, Y.; Nguyen, M. T.; Yonezawa, T., Synthesis of Positively Charged Photoluminescent Bimetallic Au–Ag Nanoclusters by Double-Target Sputtering Method on a Biocompatible Polymer Matrix. Langmuir 2017, 33 (36), 9144-9150.

17. Nguyen, M. T.; Zhang, H.; Deng, L.; Tokunaga, T.; Yonezawa, T., Au/Cu Bimetallic Nanoparticles via Double-Target Sputtering onto a Liquid Polymer. Langmuir 2017, 33 (43), 12389-12397.

18. Aschenbrenner, O.; Supasitmongkol, S.; Taylor, M.; Styring, P., Measurement of vapour pressures of ionic liquids and other low vapour pressure solvents. Green Chem. 2009, 11 (8), 1217-1221.

19. Ishida, Y.; Udagawa, S.; Yonezawa, T., Growth of sputtered silver nanoparticles on a liquid mercaptan matrix with controlled viscosity and sputter rate. Colloids Surf. A: Physicochem. Eng. Asp. 2016, 498, 106-111.

20. Rauber, M.; Alber, I.; Müller, S.; Neumann, R.; Picht, O.; Roth, C.; Schökel, A.; Toimil-Molares, M. E.; Ensinger, W., Highly-ordered supportless three-dimensional nanowire networks with tunable complexity and interwire connectivity for device

integration. Nano lett. 2011, 11 (6), 2304-2310.

21. Shen, Q.; Jiang, L.; Zhang, H.; Min, Q.; Hou, W.; Zhu, J.-J., Three-dimensional dendritic Pt nanostructures: sonoelectrochemical synthesis and electrochemical applications. J. Phys. Chem. C 2008, 112 (42), 16385-16392.

22. Manikandan, M.; Hasan, N.; Wu, H.-F., Platinum nanoparticles for the photothermal treatment of Neuro 2A cancer cells. Biomater. 2013, 34 (23), 5833-5842.

23. Wang, C.; Daimon, H.; Onodera, T.; Koda, T.; Sun, S., A General Approach to the Size-and Shape-Controlled Synthesis of Platinum Nanoparticles and Their Catalytic Reduction of Oxygen. Angew. Chem. Int. Ed. 2008, 47 (19), 3588-3591.

24. Mostafa, S.; Behafarid, F.; Croy, J. R.; Ono, L. K.; Li, L.; Yang, J. C.; Frenkel, A. I.; Cuenya, B. R., Shape-dependent catalytic properties of Pt nanoparticles. J. Am. Chem. Soc. 2010, 132 (44), 15714-15719.

25. Chen, J.; Lim, B.; Lee, E. P.; Xia, Y., Shape-controlled synthesis of platinum nanocrystals for catalytic and electrocatalytic applications. Nano Today 2009, 4 (1), 81-95.

26. Hui, C.; Li, X.; Hsing, I.-M., Well-dispersed surfactant-stabilized Pt/C nanocatalysts for fuel cell application: dispersion control and surfactant removal. Electrochim. Acta 2005, 51 (4), 711-719.

27. Li, D.; Wang, C.; Tripkovic, D.; Sun, S.; Markovic, N. M.; Stamenkovic, V. R., Surfactant removal for colloidal nanoparticles from solution synthesis: the effect on catalytic performance. ACS Catal. 2012, 2 (7), 1358-1362.

28. Ramalingam, B.; Mukherjee, S.; Mathai, C. J.; Gangopadhyay, K.; Gangopadhyay, S., Sub-2 nm size and density tunable platinum nanoparticles using room temperature tilted-target sputtering. Nanotechno. 2013, 24 (20), 205602.

29. Andreazza, P.; Andreazza-Vignolle, C.; Rozenbaum, J.; Thomann, A.-L.; Brault, P., Nucleation and initial growth of platinum islands by plasma sputter deposition. Surf. Coating. Technol. 2002, 151, 122-127.

30. Yoshii, K.; Tsuda, T.; Arimura, T.; Imanishi, A.; Torimoto, T.; Kuwabata, S., Platinum nanoparticle immobilization onto carbon nanotubes using Pt-sputtered room-temperature ionic liquid. RSC Adv. 2012, 2 (22), 8262-8264.

31. Staszek, M.; Siegel, J.; Kolářová, K.; Rimpelová, S.; Švorčík, V., Formation and antibacterial action of Pt and Pd nanoparticles sputtered into liquid. Micro. Nano Lett. 2014, 9 (11), 778-781.

32. Hu, X.; Takai, O.; Saito, N., Simple synthesis of platinum nanoparticles by plasma sputtering in water. Jpn. J. Appl. Phys. 2013, 52 (1S), 01AN05.

33. Yoshii, K.; Tsuda, T.; Torimoto, T.; Kuwabata, S., Carbon composite with Pt nanoparticles prepared by Room-temperature ionic liquid-sputtering method. ECS Trans. 2010, 33 (7), 127-133.

34. Tsuda, T.; Kurihara, T.; Hoshino, Y.; Kiyama, T.; Okazaki, K.-i.; Torimoto, T.; Kuwabata, S., Electrocatalytic activity of platinum nanoparticles synthesized by room-temperature ionic liquid-sputtering method. Electrochem. 2009, 77 (8), 693-695.

35. Cha, I. Y.; Ahn, M.; Yoo, S. J.; Sung, Y.-E., Facile synthesis of carbon supported

metal nanoparticles via sputtering onto a liquid substrate and their electrochemical application. RSC Adv. 2014, 4 (73), 38575-38580.

36. Rioux, R.; Song, H.; Hoefelmeyer, J.; Yang, P.; Somorjai, G., High-surface-area catalyst design: synthesis, characterization, and reaction studies of platinum nanoparticles in mesoporous SBA-15 silica. J. Phys. Chem. B 2005, 109 (6), 2192-2202.

37. Kou, R.; Shao, Y.; Wang, D.; Engelhard, M. H.; Kwak, J. H.; Wang, J.; Viswanathan, V. V.; Wang, C.; Lin, Y.; Wang, Y., Enhanced activity and stability of Pt catalysts on functionalized graphene sheets for electrocatalytic oxygen reduction. Electrochem. Commun. 2009, 11 (5), 954-957.

38. Wang, Y.; Ren, J.; Deng, K.; Gui, L.; Tang, Y., Preparation of tractable platinum, rhodium, and ruthenium nanoclusters with small particle size in organic media. Chem. Mater. 2000, 12 (6), 1622-1627.

39. Chiang, Y.-D.; Lian, H.-Y.; Leo, S.-Y.; Wang, S.-G.; Yamauchi, Y.; Wu, K. C. W., Controlling Particle Size and Structural Properties of Mesoporous Silica Nanoparticles Using the Taguchi Method. J. Phys. Chem. C 2011, 115 (27), 13158-13165.

40. Tanaka, S. I.; Miyazaki, J.; Tiwari, D. K.; Jin, T.; Inouye, Y., Fluorescent platinum nanoclusters: synthesis, purification, characterization, and application to bioimaging. Angew. Chem. 2011, 123 (2), 451-455.

41. Wender, H.; de Oliveira, L. F.; Migowski, P.; Feil, A. F.; Lissner, E.; Prechtl, M. H.; Teixeira, S. R.; Dupont, J., Ionic liquid surface composition controls the size of

gold nanoparticles prepared by sputtering deposition. J. Phys. Chem. C 2010, 114 (27), 11764-11768.

42. Teranishi, T.; Hosoe, M.; Tanaka, T.; Miyake, M., Size control of monodispersed Pt nanoparticles and their 2D organization by electrophoretic deposition. J. Phys. Chem. B 1999, 103 (19), 3818-3827.

3. Pt/Cu alloy nanoparticles prepared by single target sputtering

3.1 Introduction

Pt nanoparticles (NPs) with a high surface-to-volume ratio are one of the most important classes of industrial catalysts.[1-3] However, Pt is highly expensive and its resources are limited. Meanwhile, in comparison to monometallic Pt NPs, Pt-based (Pt/Pd,[4] Pt/Au,[5-7] Pt/Ag,[8,9] Pt/Cu,[10-13] etc.) alloy NPs are recently attracting much attention as they include smaller contents of Pt and exhibit higher catalytic activities. Among these Pt-based alloy NPs, Pt/Cu alloy NPs are important as Cu is present in abundant quantities in the earth's crust and the addition of Cu can improve the catalytic properties of alloy NPs.[10-13] It has been found that a sample containing 25 at% Pt and 75 at% Cu exhibited superior catalytic activity and the highest anti-poisoning ability among the tested Pt/Cu bimetallic catalysts with Cu content in the range of 50% to 75%.[12]

The success of bimetallic NPs depends not only on the size and shape-controlled distribution but also on the method of preparation.[4,14,15-17] Usually, Pt/Cu alloy NPs are obtained by chemical reduction routes[10-12] using strong reducing agents11 or at high temperatures.[10,12,13] The particle sizes are often larger than 3 nm. Hence, developing innovative methods capable of yielding sufficiently pure and small NPs is desirable. Recently, bimetallic NPs synthesized by sputtering onto a liquid matrix have been reported.[14] NP synthesis by vacuum sputtering onto a liquid matrix is a

green method because it neither uses toxic reducing agents nor produces any by-products.[18,19] The method is very versatile in terms of controlling the size of the obtained NPs. In addition, choosing a liquid matrix with a good stabilizing ability can inhibit NP aggregation and help in controlling their growth. When a metal target is attacked by gaseous ions, metal atoms or clusters (aggregation of several atoms) are ejected; these collide with each other multiple times to form NPs. It is accepted that there occur no considerable collisions between the sputtered species in the gas phase at low gas pressures.[20,21] Thus, particle growth mainly occurs in the liquid phase. There are three possible growth mechanisms after particles land on a liquid surface during vacuum sputtering onto a liquid-particle collision, aggregation, and growth on the liquid surface; these NPs then fall into the bulk liquid and are stabilized. Alternatively, particles can fall into the bulk of the liquid without collision and grow on the liquid surface; however, collision and growth occur inside the bulk liquid. In another mechanism, particles grow both on the liquid surface and inside the bulk liquid. Parameters pertaining to the liquid, such as the surface tension, viscosity, temperature, and functional groups, determine the major growth mechanism. Wender et al. pointed out that both nucleation and growth of Au NPs occurred on the surfaces of several ionic liquids.[20] It was reported that the growth of Au NPs occurred on the liquid surface of castor oil at a low sputtering power and inside the liquid at a high sputtering power. Vanecht et al. reported evidence that Au NPs grow inside the ionic liquids and the growth was regulated by the viscosity of liquid as the particle sizes have a linear relationship with the viscosity.[21] Carette et al. pointed out that Ag NPs

grow inside ionic liquids after observing that chemical interactions between 1-butyl-3-methylimidazolium bis(trifluoromethylsulfonyl)-imide ([BMIM][TFSI]) molecules and Ag atoms are highly favored.[22] However, other studies reported that Au NPs grow on the surface as well as in the bulk of an ionic liquid; this result was postulated based on the observation that small Au NPs were obtained with ionic liquids of low surface tension and viscosity.[23] Hatakeyama et al. showed that increasing the temperature of polyethylene glycol (PEG) used as the liquid substrate for the sputtering of an Au target led to the formation of large Au NPs; they demonstrated that the growth of Au NPs in PEG was controlled by the diffusive velocity of the sputtered particles.[24] The exact growth mechanism of NPs synthesized by sputtering onto liquids is still a subject of discussion, especially the growth mechanism of NPs in liquid polymers. It is dependent not only on the liquids used but also on the type of metal/oxide NPs and how they are produced. Au/Ag,[25] Au/Pt,[26] and Au/Cu[27] alloy NPs have been prepared by sputtering a mixed target material onto an ionic liquid by the Torimoto group. Au/Ag,[28] Au/Cu,[29,30] and Au/Pd[31] alloy NPs synthesized by co-sputtering onto liquids have been reported. Au/Pd alloy NPs have also been prepared by sputtering alloy targets onto ionic liquids.[32] An interesting approach for the synthesis of Pt/Cu bimetallic NPs by sputtering onto TiO_2 nanotube arrays was described by Farsinezhad et al.[33] However, as far as we know, the synthesis of Pt/Cu alloy NPs by sputtering onto a liquid has not been reported yet. Different types of liquid matrices, such as ionic liquids,[22,23,25-27,31] polymers,[24,28,30,34-38] silicone oil,[39] and vegetable oil,[40] can be considered for the preparation of Pt/Cu alloy

NPs by sputtering. Recently, liquid PEG, a biocompatible and economic polymer has been proven to be a useful medium for the synthesis of Pt NPs via sputtering with negligible aggregation. The low vapor pressure of PEG makes vacuum sputter deposition possible. The surface tension and viscosity of PEG, especially PEG with a molecular weight of 600, can stabilize NPs.[37] However, the growth mechanism of sputtered alloy NPs, Pt/Cu in particular, in PEG is not yet known.

In the current study, for the first time ever, we synthesized Pt/Cu alloy NPs by sputtering a Pt/Cu alloy target onto PEG (M_W = 600) as the capture medium and systematically studied the influence of synthesis parameters on the particle size in order to elucidate the growth mechanism of Pt/Cu alloy NPs. Our results show that this synthesis method is a green approach for the preparation of stable colloidal Pt/Cu alloy NPs. The growth of Pt/Cu alloy NPs can be controlled by carefully selecting the deposition parameters, such as sputtering current, rotation speed of the stirrer, sputtering period, sputtering time, and the temperature of PEG. Our results prove that aggregation and growth of Pt/Cu NPs occur at the liquid polymer surface as well as inside the liquid polymer.

3.2 Experimental section

3.2.1 Preparation of Pt/Cu NPs

A Pt/Cu (1/1 (w/w), 1/3.09 (mol/mol)) alloy target (50 mm in diameter, Tanaka Precious Metals, Japan) was used to synthesize Pt/Cu NPs. PEG (M_W = 600, Junsei)

was degassed in an oil bath with continuous stirring at 80 °C in vacuum for 2 h and then put in a Petri dish (60 mm in diameter), which was placed in the sputter chamber horizontally. PEG was stirred using a stirrer at a set rotation speed. Before collecting Pt/Cu NPs, the Pt/Cu alloy target was pre-sputtered for 10 min to clean the target surface. A carbon-coated transmission electron microscopy (TEM) grid (Nisshin EM, Japan) or a glass substrate for XRD measurement was placed at the center of the Petri dish. The distance of target-PEG surface, target-carbon-coated TEM grid, and target-glass substrate was set at 50 mm. Sputtering was carried out in an inert Ar atmosphere at room temperature. The pressure of the vacuum chamber was kept constant at 2 Pa during the sputtering process. The metal target was cooled during sputtering using cooling ethanol (0 °C). The typical process parameters were as follows - sputtering current of 30 mA, 80 rpm rotation speed of the stirrer, 30 min of sputtering time, and PEG temperature of 30 °C.

3.2.2 Study of the particle growth mechanism

To investigate the growth mechanism of Pt/Cu alloy NPs during sputtering, the effects of process parameters on the formation of Pt/Cu NPs were studied, *i.e.*, by varying (1) sputtering current onto PEG and (2) using TEM grids at different sputtering times, varying the (3) rotation speed of the stirrer, (4) sputtering period, (5) sputtering time, and (6) temperature of PEG, as summarized in Table 3.1. The vapor pressure of PEG[24] is low enough for all the experiments in the present study. The

purpose of experimental sets (1)-(3) is to analyze the size of Pt/Cu NPs at different currents, the ability of PEG to inhibit the growth of Pt/Cu NPs, and the growth of Pt/Cu NPs after reaching the liquid surface. Experiments (4)-(6) are designed to differentiate growth on the PEG surface (experiment (4)) and in the bulk liquid (experiment (5) and (6)). This is based on our assumption that the growth of sputtered atoms/clusters on the PEG surface is governed by their collisions during their stay on the liquid surface before falling into to the bulk liquid. Therefore, reducing the sputtering period (30 min-5 s) and introducing a few seconds of non-sputtering between two sputtering periods for letting the particles fall from the liquid surface into the bulk liquid can help reduce particle size. Secondary growth and aggregation in bulk PEG are functions of the concentration of NPs in PEG, which is in turn related to the sputtering time and viscosity (dependent on PEG temperature). Thus, monitoring changes in the NP size with respect to these factors can help in understanding the growth of NPs inside bulk PEG.

Table 3.1 Summary of the experimental parameters

	Current (mA)	Substrate	Rotation speed (rpm)	Sputtering period	Sputtering time	Temperature (°C)
1	**5-50**	PEG	80	continuous	30 min	30
2	5-50	**PEG, TEM grid**	-	-	30 min, 1 s, 5 s	-
3	30	PEG	**0-160**	continuous	30 min	30
4	50	PEG	80	**continuous, 30 s, 15 s, 5 s**	30 min	30
5	30	PEG	80	continuous	**15 min-4 h**	30
6	30	PEG	80	continuous	30 min	**20-50**

3.2.3 Characterization

The particle size, size distribution, and morphology of Pt/Cu alloy NPs were investigated by TEM (JEOL JEM-2010 or JEOL-2000FX, 200 kV), high-resolution TEM (HR-TEM, JEOL JEM-ARM200F, 200 kV), and scanning TEM (STEM, JEOL JEM-ARM200F). The TEM, HR-TEM, and STEM samples were prepared by simply dipping carbon-coated grids into PEG dispersions containing NPs for a few seconds, immediately followed by dipping them into ethanol for a few minutes, and finally drying the grids in air at room temperature for a few minutes. The size and size distribution were obtained by measuring at least 300 particles at different areas of the grid using ImageJ and rounding up to the first decimal place. TEM-energy dispersive X-ray spectroscopy (EDX), STEM-EDX elemental mapping, STEM-EDX line

profiling, and X-ray fluorescence spectrometry (XRF, JSX-3100RII, JEOL) were conducted to verify the existence and composition of the Pt/Cu alloy NPs. Optical absorption spectra of the NPs were generated on a JASCO V-630 spectrophotometer using a 1 mm optical path quartz cuvette, immediately after sputter deposition. All the measurements were baseline corrected using a blank quartz cuvette without any PEG-NP dispersion. The crystalline structure of the NPs was determined using HR-TEM, STEM, and X-ray diffraction (XRD, Rigaku Mini Flex II, Cu Kα radiation, λ = 1.5418 Å). Samples for XRD analysis were prepared by adding acetone to Pt/Cu NPs in PEG dispersions followed by centrifuging several times; finally, the solid was dried under vacuum. XRD analysis was also performed on Pt/Cu samples prepared by sputtering a Pt/Cu alloy target directly onto XRD glass substrates for various sputtering times (30 s-5 min). The XRD patterns were recorded at a scan speed of 0.5°/min. The deposition rate of Cu was estimated by measuring the weight of the sputtered material obtained on an aluminum foil.

3.3 Results and discussion

First, we investigated the sputtered Pt/Cu NPs obtained in PEG to confirm that they are indeed alloy NPs; this was carried out using UV-Vis spectroscopy, XRD analysis, and STEM-EDX line profiles. The compositions of the target and sputtered materials were similar, as analyzed by XRF and TEM-EDX. Later, we studied the growth of Pt/Cu NPs after landing on the liquid PEG surface.

3.3.1 Composition, structure, and optical properties of the sputtered Pt/Cu NPs dispersed in PEG

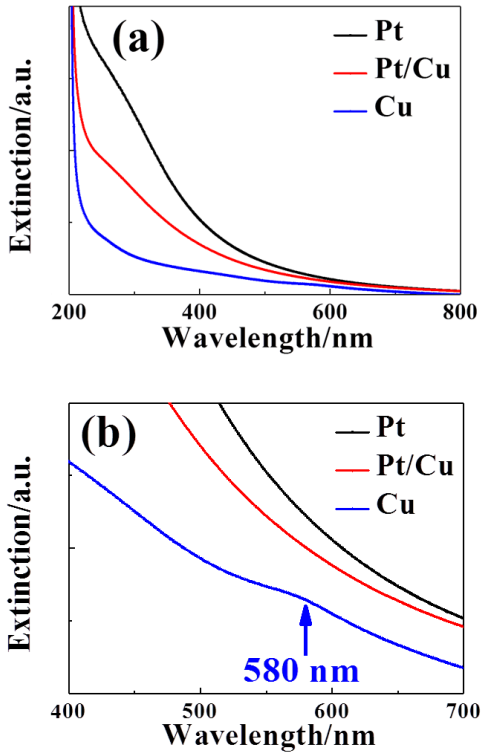

Figure 3.1 (a) UV-Vis absorption spectra of Pt (black curve), Pt/Cu (red curve), and Cu (blue curve) NPs obtained by continuous sputter deposition onto PEG at a sputtering current of 20 mA and (b) their respective enlarged spectra.

Figure 3.1a shows the UV-Vis absorption spectra of Pt, Pt/Cu, and Cu NPs and Figure 3.1b represents an enlarged view of these spectra. It can be clearly seen that PEG containing Cu NPs exhibits a broad peak with the center around 580 nm, which can be assigned to the surface plasmon resonance (SPR) of Cu NPs.[41] However, no plasmon absorption of Cu was detected in the dispersion of Pt/Cu bimetallic NPs under the same conditions, which reveals that it is not a physical mixture of Pt and Cu

NPs.

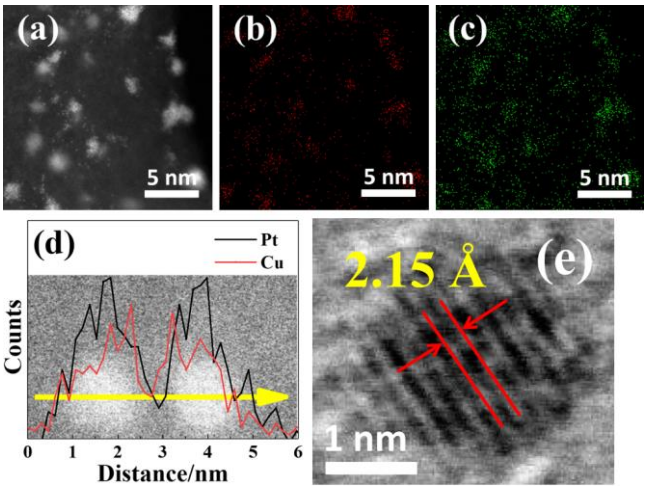

Figure 3.2 Pt/Cu NPs prepared by continuous sputtering onto PEG at a sputtering current of 50 mA for 30 min, with a rotation speed of 80 rpm at 30 °C. (a) HAADF-STEM image, corresponding EDX mapping images of (b) Pt L and (c) Cu K, (d) STEM-EDX line profile measured across two NPs; the inset shows the STEM-HAADF image of the analyzed NPs (the yellow arrow shows the scanning path for the line profile). (e) HR-TEM image of a Pt/Cu NP.

Table 3.2 shows the compositions of the NPs obtained by sputtering onto glass for 30 min (XRF) and onto TEM grids for 30 s (TEM-EDX). Different sputtering times were chosen for XRF and EDX analysis in order to obtain adequate signals at sputtering currents of 20 and 40 mA. As listed in Table 3.2, the composition of the resulting NPs was around 71 at.% Cu; it is clear that the NP composition was not affected by the sputtering current and time.

Table 3.2 XRF and EDX analyses of the sputtered materials

Current/mA	20	40
Cu at.%, XRF	69.9 ± 0.3	70.1 ± 0.6
Cu at.%, EDX	75.7 ± 5.3	71.6 ± 1.9

The high-angle annular dark field (HAADF)-STEM image and EDX elemental map (Figures 3.2a-3.2c) show that all the particles contain both Pt and Cu. The line profile in Figure 3.2d also shows that the NPs contain both Pt and Cu elements but no clear core-shell structures were formed, which demonstrates that the obtained NPs were Pt/Cu alloys. In the HR-TEM image (Figure 3.2e), the measured fringe spacing was 2.15 Å, which is in between that of Pt and Cu. The value is identical with the reported lattice spacing of the (111) plane of $Pt_{29}Cu_{71}$ (2.15 Å), implying that $Pt_{29}Cu_{71}$ alloy NPs were formed. The lattices cross through the whole particle, indicating single crystal formation. Alloy formation was further confirmed by XRD analysis (Figure 3.3). The (111) and (200) peaks of the Pt/Cu alloy target, sputtered Pt/Cu films on glass, and Pt/Cu NPs in PEG are located between those of Pt and Cu; no other peaks, which would indicate the presence of impurities, were detected. These results indicate that the sputtering of Pt/Cu alloy targets resulted in alloy products with a face-centered cubic crystal structure. [42] It can be noticed in Figure 3.3 that the (111) and (200) peaks became sharper and more intense when the sputtering time increased from 1 min to 5 min due to an increase in the size of Pt/Cu films and the Pt/Cu amount. The large line broadening observed in the XRD peak of Pt/Cu NPs sputtered onto PEG (red curve) is thought to be caused by the small particle size; a mean

crystalline size of ca. 3.2 nm was estimated using Scherrer's equation. Interestingly, the (111) peak position increases in the order of Pt/Cu NPs < Pt/Cu film-1 min < Pt/Cu film-5 min < Pt/Cu target. This is probably due to the oxidation of Cu which is more severe in small Pt/Cu NPs and thin film (1 min sputtering) compared to that in the thick film (5 min sputtering) and bulk Pt/Cu alloy target. The oxidation of the Pt/Cu NPs after purification and exposed to air resulted in slightly less Cu in metallic Pt/Cu alloy, thus the XRD peak of the NPs or thin film was slightly shifted to a lower angle than the that of the bulk Pt/Cu. Therefore, on the basis of the HR-TEM, STEM-EDX mapping, STEM-EDX line profile, and XRD results, we concluded that under the employed conditions, single crystalline $Pt_{29}Cu_{71}$ alloy can be generated via sputtering onto PEG. Hereafter, we refer to Pt29Cu71 alloy NPs as Pt/Cu NPs.

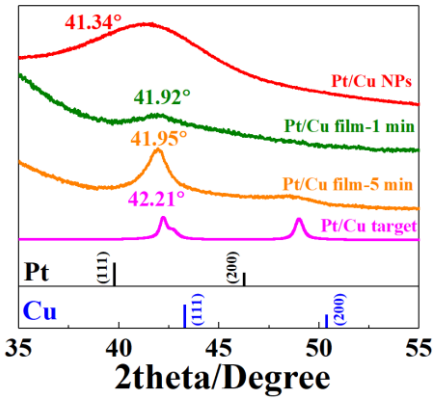

Figure 3.3 XRD profiles of a Pt/Cu alloy target (pink curve), Pt/Cu thin films sputtered on XRD glass substrates at a sputtering current of 50 mA for 5 min (orange curve) and 1 min (green curve), Pt/Cu NPs prepared by continuously sputtering onto PEG at a sputtering current of 30 mA with a rotation speed of 80 rpm for 4 h at 30 °C (red curve); the stick patterns represent the reference patterns of Cu (JCPDS number 04-0836) and Pt (JCPDS number 04-0802).

3.3.2 Growth mechanism of Pt/Cu NPs during sputtering

To study the growth mechanism of Pt/Cu NPs during sputtering, the effects of physical conditions, including (1) sputtering current, (2) substrate, (3) rotation speed of the stirrer, (4) sputtering period, (5) sputtering time, and (6) temperature of PEG, on the formation of Pt/Cu NPs were studied, as summarized in Table 3.1.

3.3.2.1 Effect of the sputtering current and substrate on particle size

Photographs of PEG dispersions of Pt/Cu NPs generated at various sputtering currents at 30 °C with a rotation speed of 80 rpm and their corresponding UV-Vis absorption spectra are shown in Figure 3.4. After sputtering, no films or aggregates were observed on the PEG surface. The color of the dispersions became darker when the sputtering current increased. The generated UV-Vis absorption spectra corroborate this observation; increasing the sputtering current resulted in a gradual increase in the UV-Vis absorption intensity. This may be attributed to an increase in the particle concentration. The appearance of a broad absorption band at 260 nm is indicative of the formation of Pt/Cu alloy NPs.[43] Absorption at shorter wavelengths is usually ascribed to the existence of smaller particles, while absorption at longer wavelengths corresponds to larger particles.[44] The absorption shoulder at 260 nm slightly shifted to longer wavelengths as the sputtering current increased, thus suggesting an increase in the particle size. Sputtering current is related to the sputtering rate, i.e., the number of atoms ejected from the metal target per unit time. Increasing the sputtering current produces a higher number of atoms, which results in a higher collision frequency.

Thus, bigger particles were obtained.

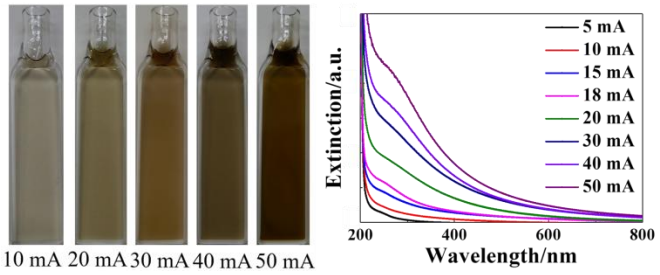

Figure 3.4 Photographs of PEG dispersions of Pt/Cu NPs under ambient light (left) and UV-Vis absorption spectra of the NPs (right) obtained by continuous sputter deposition onto PEG at different sputtering currents for 30 min at 30 °C with a rotation speed of 80 rpm.

The above hypothesis was verified by TEM analysis of Pt/Cu NPs in PEG dispersions. The TEM images and calculated particle sizes and size distributions are displayed in Figure 3.5. All the NPs were individual particles; the average size of the Pt/Cu NPs was found to increase with an increase in the sputtering current. As discussed previously, this is related to an increase in the sputtering rate.

Precipitation was not apparent in any of the samples when they were stored in the dark at room temperature for several months. Under similar conditions, Cu NPs dispersed in PEG precipitated after several weeks. This indicates that the Pt/Cu alloy NPs dispersed in PEG were highly stable when compared to monometallic Cu NPs. The particle size of the Pt/Cu sample prepared at a sputtering current of 30 mA increased by only 0.1 nm after storing in the dark at room temperature for 1 year (Figure S1), whereas Cu NPs growth happened after keeping for few hours.45 This

indicates negligible growth in Pt/Cu NPs after a sputtering cycle is completed, which is similar to the case of Pt NPs.[37] Thus, alloying of Cu with Pt improves the colloidal stability of the resulting NPs as compared to monometallic Cu NPs.

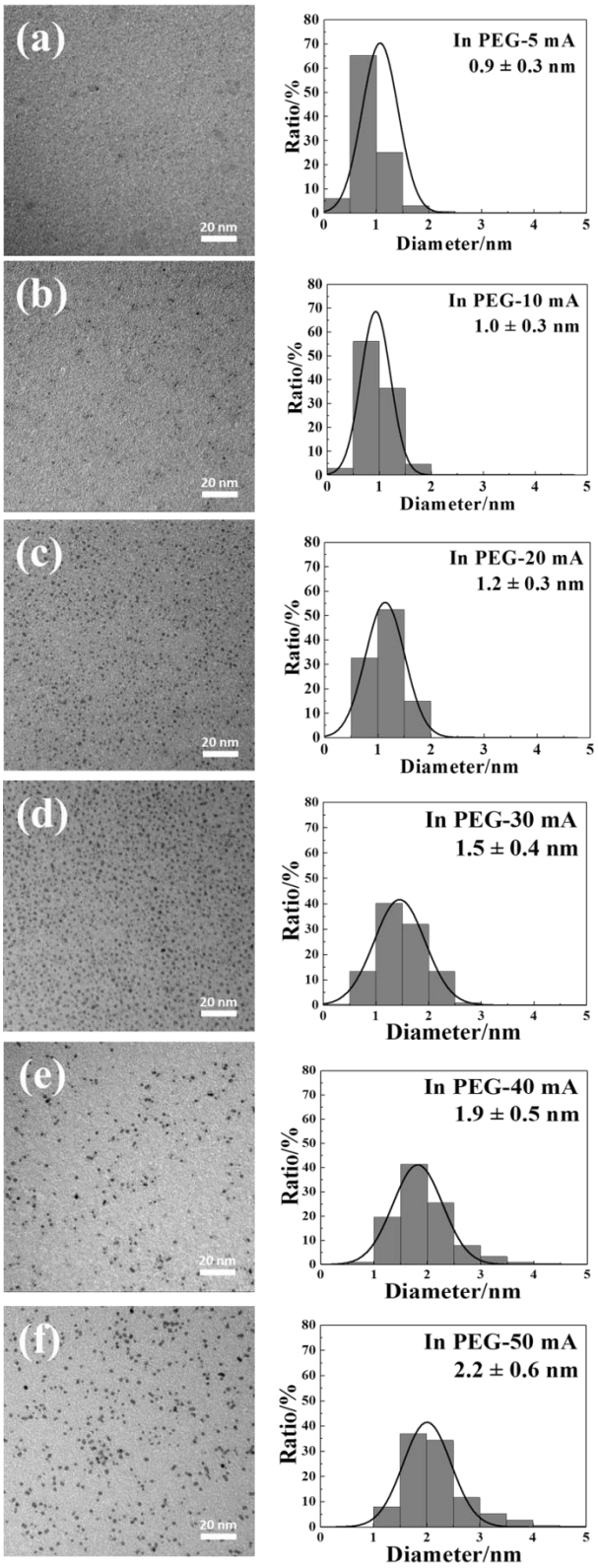

Figure 3.5 TEM images and size histograms of the NPs obtained by continuous sputtering onto PEG at different sputtering currents: (a) 5, (b) 10, (c) 20, (d) 30, (e) 40, and (f) 50 mA for 30 min at 30 °C with a rotation speed of 80 rpm.

To verify if agglomeration takes place after the clusters land on the surface of PEG, sputter deposition onto TEM grids was also conducted at different sputtering currents of 10-50 mA for different sputtering times of 1 s and 5 s. The particle sizes were estimated from TEM and STEM images.

Figure 3.6 shows the TEM images, particle sizes, and the respective histograms of Pt/Cu NPs obtained by sputtering onto a TEM grid for 5 s. Figure S2 shows the corresponding results of Pt/Cu NPs generated by sputtering onto a TEM grid for 1 s. The average size of Pt/Cu NPs increased from ca. 1.3 to 4.5 nm when the sputtering current increased from 10 (Figure 3.6a) to 50 mA (Figure 3.6e), corresponding to nanoparticle densities of approximately 6.9×10^4 (10 mA), 5.5×10^4 (30 mA) and 3.2×10^4 (50 mA) particles per μm^2. In other words, with an increase of the sputtering current, the number density of NPs decreases and average particle size increases. Thus, the growth of NPs on solid surface likely follows the island growth model for deposited film growth in vacuum sputter deposition. Pt/Cu NPs generated at low sputtering currents (10-30 mA) were spherical; roughly spherical NPs were obtained at a sputtering current of 40 mA and polycrystalline islands with a very broad size distribution were observed at a sputtering current of 50 mA. Further increase in the sputtering time led to the formation of large polycrystalline islands (Figure S3). This could be attributed to the fact that increasing the sputtering current (Figure S4) or sputtering time increased the number of Pt/Cu particles landing on the TEM grids. They cannot move on the solid substrate and thus increase the particle size by joining with each other.

The particle size vs. sputtering current tendency is shown in Figure 3.7. The particle size increased as the sputtering current increased, which implies that the particle size can be controlled in a narrow range by varying the sputtering current. We previously reported Pt NPs synthesized by this method,[37] where we observed that Pt/Cu NPs were slightly larger than Pt NPs. The Pt/Cu NPs obtained by sputtering onto PEG were larger than those obtained by sputtering onto a TEM grid (1 s), but smaller than those sputtered onto TEM grids for 5 s and 30 s. This suggests that the collision/aggregation and growth of sputtered Pt/Cu atoms and clusters occur to some extent after reaching the PEG surface. PEG helps in dispersing and stabilizing Pt/Cu NPs as well as in inhibiting individual small particle from growing to big sized particles and aggregations as observed in the case of NPs sputtered onto TEM grids for 5-30 s. It has been reported that smaller and more uniform Au NPs obtained in the ionic liquid with lower surface tension and lower viscosity.[23] On the other hand, it can also be assumed that a large number of oxygens in PEG coordinated with the surface of the NPs and assisted in their stabilization. Thus, we suggest that possibly the PEG chains coordinated with the metal particle surface and the viscosity of PEG led the formation of small particles with narrow size distributions.[24] We will revisit this point after discussing other results. On the basis of the above-mentioned results, we can conclude that after landing on the PEG surface, Pt/Cu NPs grew to a certain extent before being stabilized by PEG.

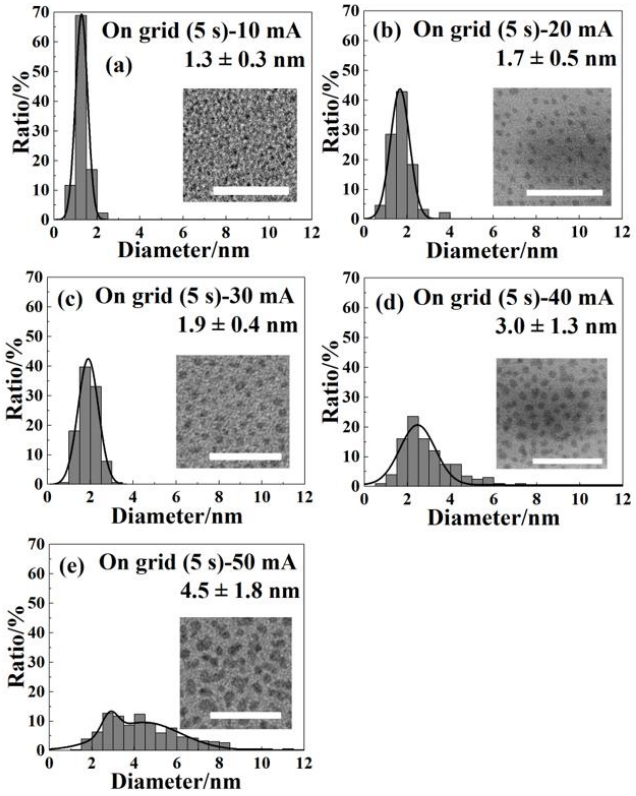

Figure 3.6 Size histograms of NPs obtained by sputtering onto TEM grids for 5 s at different sputtering currents: (a) 10 mA, (b) 20 mA, (c) 30 mA, (d) 40 mA, (e) 50 mA. The insets are corresponding TEM images; all scale bars are 20 nm.

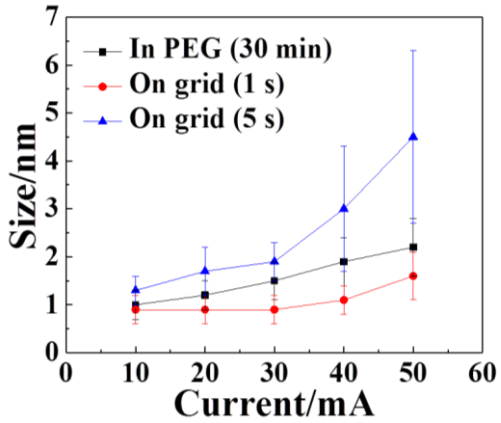

Figure 3.7 Relationship between the particle size and sputtering current. Continuous sputtering onto PEG (black) and TEM grids for 1 s (red) and 5 s (blue).

3.3.2.2 The effect of rotation speed of stirrer on particle size

Figure 3.8 shows the relationship between particle size and rotation speed of the stirrer. The corresponding TEM images, particle size distributions, and UV-Vis spectra of Pt/Cu NPs prepared at different rotation speeds of the stirrer (0-160 rpm) can be found in Figure S5. The other experimental conditions were as follows - sputtering current of 30 mA, PEG temperature of 30 °C, and sputtering time of 30 min. The TEM image and size distribution of Pt/Cu NPs produced at 80 rpm can be found in Figure 3.5d. Smaller Pt/Cu NPs with a narrow size distribution were generated at higher rotation speeds; this result agrees well with our previous study.[46] Increasing the rotation speed of the stirrer accelerates the diffusion of Pt/Cu atoms and clusters not only on the liquid surface but also inside the liquid, thus suppressing the accumulation of NPs on the liquid polymer surface and inside the liquid polymer, finally forming small particles. This result also confirms that Pt/Cu atoms, clusters, and NPs aggregated and grew after landing on PEG surface.

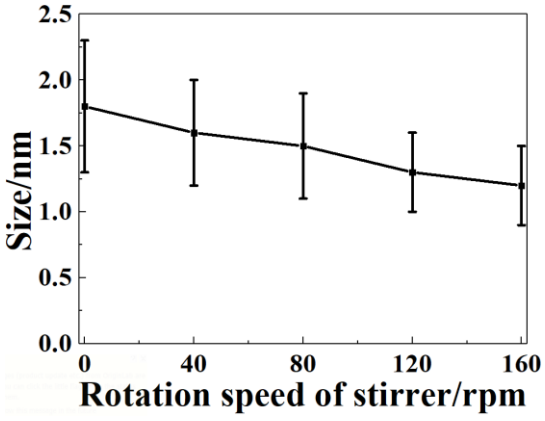

Figure 3.8 Relationship between particle size and rotation speed of the stirrer. The error bars represent the standard deviation of the particle size.

3.3.2.3 The effect of sputtering period on particle size

In order to find out whether particle growth occurs on the PEG surface, we kept the total sputtering constant, i.e., 30 min for having a fixed amount of metal atoms in the liquid and conducted discontinuous sputtering with sputtering periods of 30 s, 15 s, and 5 s, with a sputtering interval of 5 s (Figure 3.9a). For example, a sputtering period of 30 s means we conduct sputtering for 30 s followed by stopping sputtering for 5 s, with a total sputtering time of 30 min (Figure 3.9a). A stopping time of 5 s was chosen as it is long enough for a particle to fall below the PEG surface. In other words, 5 s is longer than the residence time of NPs on the PEG surface. This was deduced from Figure 3.7, where it was observed that Pt/Cu NPs in PEG are smaller than those obtained by sputtering onto a TEM grid for 5 s. If the particle growth occurs on the PEG surface, shortening the sputtering period thereby having a larger number of stopping time can allow particle fall through the PEG surface before collision and growth on the PEG surface. Hence, smaller particle size can be obtained as depicted in Figure 3.9b. The particle size and size-distribution results at different sputtering periods are shown in Figures 3.9c. The TEM image and size distribution obtained after continuous sputtering for 30 min are shown in Figure 3.5f and for discontinuous sputtering was shown in Figures 3.9d-e and S6. We found that the particle size decreased when shifting from continuous sputtering to discontinuous sputtering as expected; further, a shorter sputtering period resulted in a smaller particle size (Figure 3.9c). Thus, the growth of Pt/Cu NPs on PEG surfaces at short and long sputtering periods followed the illustration in Figure 3.9b. Particle growth on PEG surface was

inhibited more efficiently with a short sputtering period and consequently, the particle size decreased. This is an evidence of Pt/Cu NP growth on PEG surface.

3.3.2.4 The effect of sputtering time on particle size

Figure 3.10 presents the TEM images of Pt/Cu NPs generated in PEG by varying the sputtering time; other sputtering conditions were fixed at 30 mA, 30 °C, and 80 rpm. The TEM image and size distribution of the NPs obtained at a sputtering time of 30 min can be found in Figure 3.5d. The results of the present study reveal that with an increase in the sputtering time from 15 min to 2 h, the particle mean diameters and standard deviations of the Pt/Cu NPs gradually increased. At longer sputtering times (4 h), the size and aggregation of Pt/Cu NPs increased considerably. A broad size distribution was observed after 4 h of sputtering. Increasing the sputtering time can increase the concentration of Pt/Cu NPs inside PEG, which in turn increases the collision frequency among clusters or NPs, resulting in bigger particles. This indicates that aggregation and growth of Pt/Cu NPs occurred inside PEG. The formation of polycrystalline units as a result of particle aggregation and growth inside PEG could be clearly observed in the STEM image of Pt/Cu NPs synthesized over a sputtering time of 4 h (Figure 3.10e). Furthermore, the shoulder position of the UV-Vis spectrum of Pt/Cu NPs shifted to longer wavelengths as the sputtering time increased (Figure S7). This may be due to an increase in the particle size as observed in TEM.

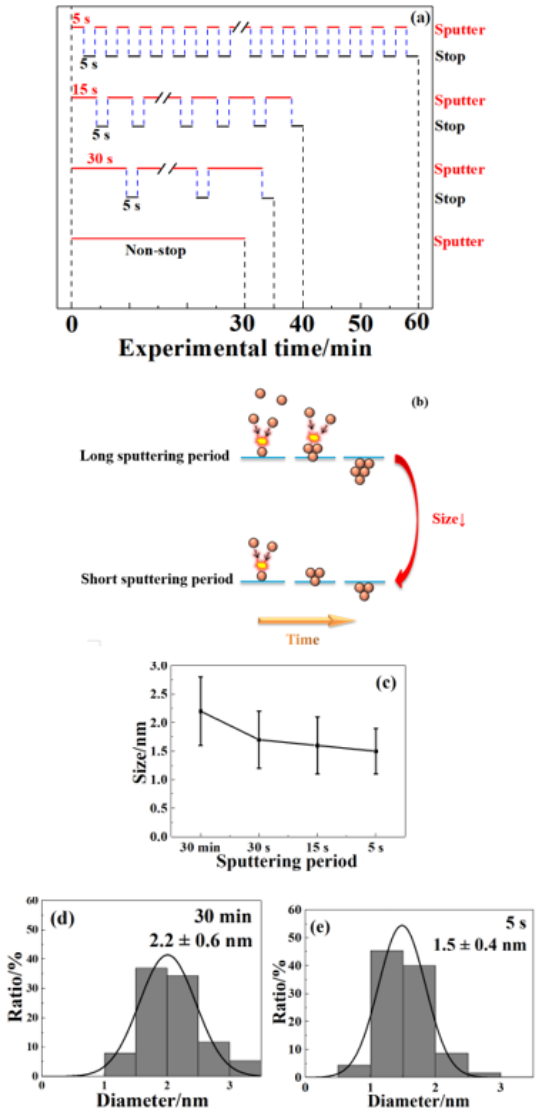

Figure 3.9 (a) A schematic illustration of different sputtering periods. (b) Schematic diagram illustrating our hypothesis of the growth of Pt/Cu NPs on the PEG surface at short and long sputtering periods. (c) Relationship between particle size and sputtering period. Size histograms of Pt/Cu NPs at a fixed sputtering current of 50 mA, rotation speed of 80 rpm, PEG temperature of 30 °C, and different sputtering periods of (d) 30 min and (e) 5 s. The total sputtering time (excluding 5 s stopping time between two sputtering periods) in all the cases was 30 min. The imag1e of Pt/Cu NPs prepared with the sputtering period of 30 min without interval is shown in Figure 3.5(f).

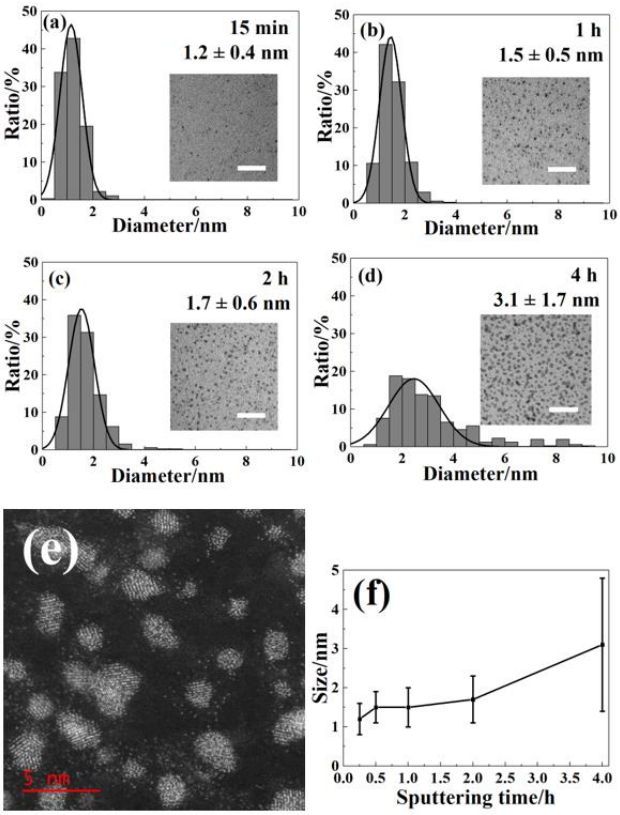

Figure 3.10 Size histograms of Pt/Cu NPs obtained by continuous sputtering onto PEG at a fixed sputtering current of 30 mA, PEG temperature of 30 °C, rotation speed of 80 rpm, and different sputtering times. (a) 15 min, (b) 1 h, (c) 2 h, and (d) 4 h. Insets are the corresponding TEM images, all the scale bars are 20 nm. (e) Corresponding STEM image at a sputtering current of 30 mA for 4 h. (f) Relationship between NP size and sputtering time. The TEM image and size distribution of the NPs obtained at a sputtering time of 30 min is shown in Figure 3.5(d).

Monometallic Pt[37] and Cu NPs also exhibited the same phenomenon, i.e., the particle size increased with an increase in the sputtering time from 30 min to 4 h (Figure S8). Among Cu, Pt, and Pt/Cu NPs, Cu NPs were the largest (5.3 ± 2.5 nm), while the sizes of Pt and Pt/Cu NPs were (2.7 ± 1.2 nm) and (3.1 ± 1.7 nm), respectively, after 4 h of sputtering at a sputtering current of 30 mA.

When the sputtering time was increased from 30 min to 4 h, it was observed that the increase in the average particle size of Cu NPs was the largest (0.11 Å/min), while Pt NPs and Pt/Cu NPs exhibited the same rate of increase (0.07-0.08 Å/min). Taking the difference in the sputtering yield of Pt and Cu into consideration, i.e., Cu has a lower sputtering yield than Pt (for 30 min sputtering, 9.7 mg (4.9×10^{-5} mol) of Pt^{37} and 2.4 mg (3.7×10^{-5} mol) of Cu were obtained at a sputtering current of 50 mA), the more pronounced effect of sputtering time on the size of Cu NPs when compared to Pt and Pt/Cu NPs indicates that Pt and Pt/Cu NPs are more stable in PEG unlike Cu NPs. Therefore, the type of metal is an important factor determining particle aggregation and growth in PEG.

3.3.2.5 The effect of PEG temperature on particle size

Pt/Cu NPs with an average size of ca. 1.5-1.6 nm were formed regardless of PEG temperature in the range of 20 to 50 °C (Figures 3.5d, S9). It is worth noting that the ratio of larger NPs to smaller NPs increased upon increasing PEG temperature; however, this increase is very small as shown in the size-distribution histograms. This result conflicts with a study on the synthesis of Au NPs by sputtering onto PEG, where it was found that the Au NP size increased from about 2 to 8 nm upon increasing PEG temperature from 20 to 60 °C.[24] The study pointed out that the stabilization effect of PEG is not strong enough to suppress the growth of Au NPs.

It has been reported that surface tension and viscosity affect particle aggregation and growth on the liquid surface and inside the liquid, respectively.[23,47] Changing the temperature of the liquid affects its surface tension and viscosity. The surface tension of PEG (M_W = 600) decreased from 45.76 to 39.86 dyn/cm with an increase in the temperature from 20 to 80 °C.[48] Thus, increasing the temperature from 20 to 50 °C is too small a change to cause drastic differences in the NP size due to growth on the PEG surface. However, the viscosity of PEG (M_W = 600) decreased significantly as the temperature increased from 20 to 50 °C from 167 to 43 cP.[24] Thus, increasing the PEG temperature results in only a slight decrease in surface tension but a significant decrease in viscosity. Therefore, the slight increase in the proportion of large Pt/Cu NPs may be attributed the growth of Pt/Cu NPs inside the liquid polymer. According to Hatakeyama et al., smaller Au particles are generated in an ionic liquid with low surface tension and viscosity.[23] However, in our case, the proportion of large particles slightly increased when the surface tension and viscosity of PEG were low. We suggest that this is because a low surface tension and viscosity lead to an increase in the diffusive velocities of the sputtered metal particles, which leads to an increase in the collision frequency, finally resulting in the formation of large particles. This phenomenon agrees well with our observation that when Cu NPs are sputtered onto PEG, the Cu NP size changed considerably (the average particle size was 3.0 ± 0.7 nm at 30 °C and 4.5 ± 1.8 nm at 50 °C (Figure S8 and Figure S10). However, we also observed that the size of Pt[37] and Pt/Cu NPs increased only negligibly. Therefore, it can be stated that PEG temperature affects the size of different metal NPs, such as Au,

Ag, Cu, Pt, and Pt/Cu, differently. As mentioned previously, the oxygen atoms of PEG coordinated with the surfaces of Au NPs and the -CH_2-CH_2- chains work as stabilizers by surrounding the NPs;[24] van der Waals interactions exist between PEG (M_W =3350) chains and Ag NPs.[49] One of the reasons for the higher colloidal stability of Pt and Pt/Cu NPs when compared to monometallic Cu and Au NPs may be due to the different interactions between different metal NPs and PEG. The degrees of aggregation and growth rates of different metal NPs are different under the same sputtering conditions. In fact, dispersions of Pt NPs[37] and Pt/Cu NPs in PEG were very stable after sputtering; there were no noticeable changes in their absorption spectra for several months when they were stored at room temperature in the dark, thus indicating that the PEG matrix is a good stabilizer for Pt and Pt/Cu NPs. However, as discussed previously, Cu NPs in PEG precipitated after several weeks and Au NPs in PEG precipitated after one week. This result agrees well with a previous report by Wender;[40] Au NPs and Ag NPs were prepared by sputtering onto castor oil and it was reported that the stabilization mechanisms for Au NPs and Ag NPs were different. Furthermore, PEG temperature in the range of 20 to 50 °C (50 °C is the upper limit of our device) does not seem to be wide enough to study its effect on the size of Pt/Cu NPs, or maybe it is because the number of particles is not high enough in the liquid for effective collision to form larger particles during sputtering. Therefore, we suggest that PEG is an effective capture medium for generating well-dispersed and stable Pt/Cu NPs with an average size of 1-3 nm over short sputtering times.

The UV-Vis spectra of Pt/Cu NP dispersions in PEG in Figure S9 shows that the shoulder positions did not change with respect to PEG temperature, indicating that the temperature of PEG did not affect the particle size, which is consistent with the TEM observations. Pt and Pt/Cu NPs were more stable than Cu NPs in PEG as demonstrated by the fact that Cu NPs aggregated severely while the sizes of Pt/Cu NPs and Pt NPs[37] were almost stable when the PEG temperature was increased from 20 to 50 °C (Figures S9 and S10).

Combined with our previous results, it can be concluded that particle growth occurs not only on PEG surface but also inside PEG and can be regulated by controlling the sputtering time, sputtering period, current, and stirring speed. Therefore, we can control particle growth by varying the experimental parameters that affect aggregation and growth of NPs on the liquid surface and inside the liquid. Under experimental conditions in the present study, we think that the temperature target is sufficiently maintained with circulating cooled ethanol and the increase in its temperature during sputtering for short time (below 30 min) and low sputtering currents (50 mA or less) is small and has negligible effect on the particle size (Figure S11). The influence of the target temperature on particle size can be studied in the future.

3.4 Conclusions

Stable Pt/Cu alloy NPs with diameters in the range of 1-3 nm and narrow size distribution were successfully synthesized at room temperature without using a reducing agent. Particle sizes could be tailored by varying the sputtering current, rotation speed of the stirrer, sputtering period, sputtering time, and PEG temperature. Compared with the samples sputtered onto TEM grids, particle growth could be inhibited to some extent using PEG as the capture medium without an additional stabilizing agent. It was found that decreasing the sputtering time, sputtering period, and sputtering current or increasing the rotation speed of the stirrer resulted in smaller Pt/Cu alloy NPs; there were no significant differences in the NP size with respect to the liquid matrix temperature (20-50 °C) over a sputtering period of 30 min. We proved that aggregation and growth of Pt/Cu alloy NPs occurred both on the PEG surface and inside the liquid bulk. Understanding the growth mechanism of NPs formed via sputtering onto liquid polymers allows good control over the size and shape of colloidal NPs and in achieving NPs with the desired properties. Our results indicate that the aggregation, growth, and colloidal stability of NPs during and after sputtering onto PEG are highly dependent on the metals used.

3.5 References

1. Godoi, D. R.; Villullas, H. M; Zhu, F.-C.; Jiang, Y.-X.; Sun, S.-G.; Guo, J.; Sun, L.; Chen, R. A Comparative Investigation of the Metal-support Interactions on the Catalytic Activity of Pt Nanoparticles for Ethanol Oxidation and Alkaline Medium. J. Power Sources 2016, 311, 81-90.

2. Silva, J. C. M.; Piasentin, R. M.; Spinacé, E. V.; Neto, A. O.; Baranova, E. A. The Effect of Antimony-tin and Indium-tin Oxide Supports on the Catalytic Activity of Pt Nanoparticles for Ammonia Electro-oxidation. Mater. Chem. Phys. 2016, 180, 97-103.

3. Hao, Y.; Wang, X.; Zheng, Y.; Shen, J.; Yuan, J.; Wang, A.-j.; Niu, L.; Huang, S. Uniform Pt Nanoparticles Incorporated into Reduced Graphene Oxides with MoO3 as Advanced Anode Catalysts for Methanol Electro-Oxidation. Electrochim. Acta 2016, 198, 127-134.

4. Toshima, N.; Yonezawa, T. Bimetallic nanoparticles-novel materials for chemical and physical applications. New J. Chem. 1998, 22, 1179-1201.

5. Hernández-Fernández, P.; Rojas, S.; Ocón, P.; Gómez de la Fuente, J.; San Fabián, J.; Sanza, J.; Pena, M.; García-García, F.; Terreros, P.; Fierro, J. Influence of the Preparation Route of Bimetallic Pt-Au Nanoparticle Electrocatalysts for the Oxygen Reduction Reaction. J. Phys. Chem. C 2007, 111, 2913-2923.

6. Suntivich, J.; Xu, Z.; Carlton, C. E.; Kim, J.; Han, B.; Lee, S. W.; Bonnet, N. p.; Marzari, N.; Allard, L. F.; Gasteiger, H. A. Surface Composition Tuning of Au-Pt Bimetallic Nanoparticles for Enhanced Carbon Monoxide and Methanol

Electro-oxidation. J. Am. Chem. Soc. 2013, 135, 7985-7991.

7. Selvarani, G.; Selvaganesh, S. V.; Krishnamurthy, S.; Kiruthika, G.; Sridhar, P.; Pitchumani, S.; Shukla, A. A Methanol-tolerant Carbon-supported Pt-Au Alloy Cathode Catalyst for Direct Methanol Fuel Cells and Its Evaluation by DFT. J. Phys. Chem. C 2009, 113, 7461-7468.

8. Zhao, D.; Yan, B.; Xu, B.-Q. Proper Alloying of Pt with Underlying Ag Nanoparticles Leads to Dramatic Activity Enhancement of Pt Electrocatalyst. Electrochem. Commun. 2008, 10, 884-887.

9. Xu, J.; Zhao, T.; Liang, Z. Synthesis of Active Platinum-silver Alloy Electrocatalyst toward the Formic Acid Oxidation Reaction. J. Phys. Chem. C 2008, 112, 17362-17367.

10. Shiraishi, Y.; Sakamoto, H.; Sugano, Y.; Ichikawa, S.; Hirai, T. Pt-Cu Bimetallic Alloy Nanoparticles Supported on Anatase TiO2: Highly Active Catalysts for Aerobic Oxidation Driven by Visible Light. ACS Nano 2013, 7, 9287-9297.

11. Xu, Z.; Zhang, H.; Liu, S.; Zhang, B.; Zhong, H.; Su, D. S. Facile Synthesis of Supported Pt-Cu Nanoparticles with Surface Enriched Pt as Highly Active Cathode Catalyst for Proton Exchange Membrane Fuel Cells. Int. J. Hydrogen Energ. 2012, 37, 17978-17983.

12. Jia, Y.; Su, J.; Chen, Z.; Tan, K.; Chen, Q.; Cao, Z.; Jiang, Y.; Xie, Z.; Zheng, L. Composition-tunable Synthesis of Pt–Cu Octahedral Alloy Nanocrystals from PtCu to PtCu3 via Underpotential-deposition-like Process and Their Electro-catalytic Properties. RSC Adv. 2015, 5, 18153-18158.

13. Xu, D.; Liu, Z.; Yang, H.; Liu, Q.; Zhang, J.; Fang, J.; Zou, S.; Sun, K. Solution-Based Evolution and Enhanced Methanol Oxidation Activity of Monodisperse Platinum-Copper Nanocubes. Angew. Chem. Int. Edit. 2009, 48, 4217-4221.

14. Nguyen, M. T.; Yonezawa, T. Sputtering onto a Liquid: Interesting Physical Preparation Method for Multi-metallic Nanoparticles. Sci. Technol. Adv. Mater. 2018, 19, 883-898.

15. Wender, H.; de Oliveira, L. F.; Migowski, P.; Feil, A. F.; Lissner, E.; Prechtl, M. H.; Teixeira, S. R.; Dupont, J. Ionic Liquid Surface Composition Controls the Size of Gold Nanoparticles Prepared by Sputtering Deposition. J. Phys. Chem. C 2010, 114, 11764-11768.

16. Shirai, H.; Nguyen, M. T.; Čempel, D.; Tsukamoto, H.; Tokunaga, T.; Liao, Y.-C.; Yonezawa, T. Preparation of Au/Pd Bimetallic Nanoparticles by a Microwave-Induced Plasma in Liquid Process. Bull. Chem. Soc. Jpn., 2017, 90, 279-285.

17. Yonezawa, T.; Čempel, D.; Nguyen, M. T. Microwave-Induced Plasma-In-Liquid Process for Nanoparticle Production. Bull. Chem. Soc. Jpn. 2018, 91, 1781-1798.

18. Torimoto, T.; Okazaki, K.-i.; Kiyama, T.; Hirahara, K.; Tanaka, N.; Kuwabata, S. Sputter Deposition onto Ionic Liquids: Simple and Clean Synthesis of Highly Dispersed Ultrafine Metal Nanoparticles. Appl. Phys. Lett. 2006, 89, 243117.

19. Ishida, Y.; Corpuz, R. D.; Yonezawa, T. Matrix Sputtering Method: a Novel Physical Approach for Photoluminescent Noble Metal Nanoclusters. Acc. Chem. Res. 2017, 50, 2986-2995.

20. Wender, H.; de Oliveira, L. F.; Feil, A. F.; Lissner, E.; Migowski, P.; Meneghetti,

M. R.; Teixeira, S. R.; Dupont, J. Synthesis of Gold Nanoparticles in a Biocompatible Fluid from Sputtering Deposition onto Castor Oil. Chem. Commun. 2010, 46, 7019-7021.

21. Vanecht, E.; Binnemans, K.; Seo, J. W.; Stappers, L.; Fransaer, J. Growth of Sputter-deposited Gold Nanoparticles in Ionic Liquids. Phys. Chem. Chem. Phys. 2011, 13, 13565-13571.

22. Carette, X.; Debièvre, B.; Cornil, D.; Cornil, J.; Leclère, P.; Maes, B.; Gautier, N.; Gautron, E.; El Mel, A.-A.; Raquez, J.-M. On the Sputtering of Titanium and Silver onto Liquids, Discussing the Formation of Nanoparticles. J. Phys. Chem. C 2018, 122, 26605-26612.

23. Hatakeyama, Y.; Okamoto, M.; Torimoto, T.; Kuwabata, S.; Nishikawa, K. Small-angle X-ray Scattering Study of Au Nanoparticles Dispersed in the Ionic Liquids 1-alkyl-3-methylimidazolium Tetrafluoroborate. J. Phys. Chem. C 2009, 113, 3917-3922.

24. Hatakeyama, Y.; Morita, T.; Takahashi, S.; Onishi, K.; Nishikawa, K. Synthesis of Gold Nanoparticles in Liquid Polyethylene Glycol by Sputter Deposition and Tempera-ture Effects on Their Size and Shape. J. Phys. Chem. C 2011, 115, 3279-3285.

25. Okazaki, K.-i.; Kiyama, T.; Hirahara, K.; Tanaka, N.; Kuwabata, S.; Torimoto, T. Single-step Synthesis of Gold–silver Alloy Nanoparticles in Ionic Liquids by a Sputter Deposition Technique. Chem. Commun. 2008, 691-693.

26. Suzuki, S.; Suzuki, T.; Tomita, Y.; Hirano, M.; Okazaki, K.-i.; Kuwabata, S.;

Torimoto, T. Compositional Control of AuPt Nanoparticles Synthesized in Ionic Liquids by the Sputter Deposition Technique. CrystEngComm 2012, 14, 4922-4926.

27. Suzuki, S.; Tomita, Y.; Kuwabata, S.; Torimoto, T. Synthesis of Alloy AuCu Nanoparticles with the L10 Structure in an Ionic Liquid Using Sputter Deposition. Dalton Trans. 2015, 44, 4186-4194.

28. Nguyen, M. T.; Yonezawa, T.; Wang, Y.; Tokunaga, T. Double Target Sputtering into Liquid: A New Approach for Preparation of Ag-Au Alloy Nanoparticles. Mater. Lett. 2016, 171, 75-78.

29. König, D.; Richter, K.; Siegel, A.; Mudring, A. V.; Ludwig, A. High-Throughput Fabrication of Au-Cu Nanoparticle Libraries by Combinatorial Sputtering in Ionic Liquids. Adv. Funct. Mater. 2014, 24, 2049-2056.

30. Nguyen, M. T.; Zhang, H.; Deng, L.; Tokunaga, T.; Yonezawa, T. Au/Cu Bimetallic Nanoparticles via Double-Target Sputtering onto a Liquid Polymer. Langmuir 2017, 33, 12389-12397.

31. Hirano, M.; Enokida, K.; Okazaki, K.-i.; Kuwabata, S.; Yoshida, H.; Torimoto, T. Composition-dependent Electrocatalytic Activity of AuPd Alloy Nanoparticles Prepared via Simultaneous Sputter Deposition into an Ionic Liquid. Phys. Chem. Chem. Phys. 2013, 15, 7286-7294.

32. Liu, C.; Cai, X.; Wang, J.; Liu, J.; Riese, A.; Chen, Z.; Sun, X.; Wang, S.-D. One-step Synthesis of AuPd Alloy Nanoparticles on Graphene as a Stable Catalyst for Ethanol Electro-oxidation. Int. J. Hydrogen Energ. 2016, 41, 13476-13484.

33. Farsinezhad, S.; Sharma, H.; Shankar, K. Interfacial Band Alignment for

Photocatalytic charge Separation in TiO2 Nanotube Arrays Coated with CuPt Nanoparticles. Phys. Chem. Chem. Phys. 2015, 17, 29723-29733.

34. Ishida, Y.; Nakabayashi, R.; Matsubara, M.; Yonezawa, T. Silver Sputtering into a Liquid Matrix Containing Mercaptans: the Systematic Size Control of Silver Nanoparticles in Single Nanometer-orders. New J. Chem. 2015, 39, 4227-4230.

35. Corpuz, R. D.; Ishida, Y.; Nguyen, M. T.; Yonezawa, T. Synthesis of Positively Charged Photoluminescent Bimetallic Au–Ag Nanoclusters by Double-Target Sputtering Method on a Biocompatible Polymer Matrix. Langmuir 2017, 33, 9144-9150.

36. Sumi, T.; Motono, S.; Ishida, Y.; Shirahata, N.; Yonezawa, T. Formation and Optical Properties of Fluorescent Gold Nanoparticles Obtained by Matrix Sputtering Method with Volatile Mercaptan Molecules in the Vacuum Chamber and Consideration of Their Structures. Langmuir 2015, 31, 4323-4329.

37. Deng, L.; Nguyen, M. T.; Yonezawa, T. Sub-2 nm Single-Crystal Pt Nanoparticles via Sputtering onto a Liquid Polymer. Langmuir 2018, 34, 2876-2881.

38. Chung, MW; Cha, I. Y.; Ha, M. G.; Na, Y.; Hwang, J.; Ham, H. C.; Kim, H.-J.; Henkensmeier, D.; Yoo, S. J.; Kim, J. Y. Enhanced CO2 Reduction Activity of Polyethylene Gly-col-modified Au Nanoparticles Prepared via Liquid Medium Sputtering. Appl. Catal. B: Environ. 2018, 237, 673-680.

39. Ishida, Y.; Sumi, T.; Yonezawa, T. Sputtering Synthesis and Optical Investigation of Octadecanethiol-protected Fluorescent Au Nanoparticles. New J. Chem. 2015, 39, 5895-5897.

40. Wender, H.; Gonçalves, R. V.; Feil, A. F.; Migowski, P.; Poletto, F. S.; Pohlmann, A. R.; Dupont, J.; Teixeira, S. R. Sputtering onto Liquids: from Thin Films to Nanoparticles. J. Phys. Chem. C 2011, 115, 16362-16367.

41. Wu, S.-H.; Chen, D.-H. Synthesis of High-concentration Cu Nanoparticles in Aqueous CTAB Solutions. J. Colloid. Interface Sci. 2004, 273, 165-169.

42. Denton, A. R.; Ashcroft, N. W. Vegard's Law. Phys. Rev. A 1991, 43, 3161.

43. Singh, H. P.; Gupta, N.; Sharma, S. K.; Sharma, R. K. Synthesis of Bimetallic Pt-Cu Nanoparticles and Their Application in the Reduction of Rhodamine B. Colloid. Surf. A 2013, 416, 43-50.

44. Haiss, W.; Thanh, N. T.; Aveyard, J.; Fernig, D. G. Determination of Size and Concentration of Gold Nanoparticles from UV-Vis Spectra. Anal. Chem. 2007, 79, 4215-4221.

45. Chau, Y.-T. R.; Deng, L.; Nguyen, M. T.; Yonezawa, T. Monitor the Growth and Oxidation of Cu-nanoparticles in PEG after Sputtering. MRS Adv. in press. DOI: 10.1557/adv.2019.55.

46. Ishida, Y.; Akita, I.; Sumi, T.; Matsubara, M.; Yonezawa, T. Thiolate-Protected Gold Nanoparticles Via Physical Approach: Unusual Structural and Photophysical Characteristics. Sci. Rep. 2016, 6, 29928.

47. Kuwabata, S.; Tsuda, T.; Torimoto, T. Room-temperature Ionic Liquid. A New Medium for Material Production and Analyses under Vacuum Conditions. J. Phys. Chem. Lett. 2010, 1, 3177-3188.

48. Korosi, G.; Kovats, E. S. Density and Surface Tension of 83 Organic Liquids. J.

Chem. Eng. Data 1981, 26, 323-332.

49. Shameli, K.; Bin Ahmad, M.; Jazayeri, S. D.; Sedaghat, S.; Shabanzadeh, P.; Jahangirian, H.; Mahdavi, M.; Abdollahi, Y. Synthesis and Characterization of Polyethylene Glycol Mediated Silver Nanoparticles by the Green Method. Int. J. Mol. Sci. 2012, 13, 6639-6650.

4. Pt/Au alloy nanoparticles prepared by double target sputtering

4.1 Introduction

Platinum (Pt) and gold (Au) nanoparticles (NPs) have been the subject of intense study, especially in catalysis.[1-7] In comparison with the monometallic counterparts, Pt/Au alloy NPs exhibit superior catalytic performances.[8,9] Although both Pt and Au have face-centered cubic (fcc) crystalline structure, Pt and Au are largely immiscible in the bulk phase diagram.[10] However, Pt/Au alloy NPs have been experimentally synthesized.[11,12] Their existence and alloy structures have also been supported by simulation based on molecular dynamics, which showed NPs (~6 nm) thermodynamically favor the formation of alloy structure.[13] Particle size, size distribution, morphology, composition, and stability, all play a very significant role in catalytic reactions. In addition, the homogeneous dispersion of Pt/Au alloy and its nanostructure lead to an excellent catalytic property.[14] Hence, there is much interest in the synthesis of Pt/Au alloy NPs. Usually, Pt/Au alloy NPs have been synthesized via chemical reduction methods.[15-18] However, NPs prepared by chemical reduction methods often use the reducing agents and contain byproducts which can influence the catalytic properties.[19] On the other hand, due to the different reduction potential of Pt and Au, core-shell structure or phase segregation has been observed.[20,21]

Sputter deposition[22-26] have attracted considerable interest for synthesizing metal alloy NPs. This is because metal alloy NPs can be formed via alloying of metal

atoms/clusters which detach from the metal target surface via sputtering.[27] Thus, there are fewer restrictions on materials and more freedom from different reduction potential. Pt/Au thin films have been prepared by co-sputtering onto Si substrate.[10] Instead of the traditional solid substrate,[10,22] using a liquid substrate for vacuum sputtering can be considered as a suitable method for obtaining alloy NPs with controllable size, shape, and composition.[28-29] Many kinds of liquids can be used as the matrix, such as ionic liquids,[30,31] vegetable oils,[32] silicone oil[33] and polymer.[34] Pt/Au alloy NPs have been synthesized by single target sputtering onto ionic liquid using mixed foil targets.[35] However, this method requires various targets with different composition for varying composition of the resulting alloy NPs. Thus, a sputtering system comprised of multiple targets for alloy formation would be ideal. Recently, sputtering onto polyethylene glycol (PEG, M_W = 600)[36-44] is considered as one of the green methods to synthesize NPs with desired properties. For example, we recently demonstrated that PEG can be used to stabilize Pt NPs and Pt/Cu alloy NPs.[36, 42] However, the preparation of Pt/Au alloy NPs using dual-target sputter deposition of Pt and Au bulk metals onto PEG has not been reported. Furthermore, the formation mechanism of Pt/Au alloy NPs synthesized by the vacuum sputtering onto liquids has not been fully understood. Especially the correlations of size, shape, composition, and atom concentration are rather ambiguous without systematic experimental estimation or simulation basics.

In the present paper, Pt/Au alloy NPs were prepared by sputtering onto PEG using Pt and Au targets at room temperature. The sputtering currents of two targets

were varied to investigate the relation of NP size, shape, composition and atomic concentration of Pt/Au NPs. We combined UV-vis spectrum, XRF, XRD, XPS, TEM, HR-TEM and STEM structural analysis with DFT calculation in order to elucidate the formation mechanism of Pt/Au NPs at the atomic scale. Our results showed that the size and shape of the Pt/Au alloy NPs are significantly dependent on the Pt/Au atomic ratio. This relation can be explained by the different formation energy of metals and atomic concentration among NPs and clusters. Note that the current approach is a general method, which can be reproduced for preparing other bimetallic NPs.

4.2 Experimental Section

4.2.1 Preparation of Pt/Au NPs

PEG (M_W = 600, Junsei, Japan) was stirred (900 rpm) under vacuum in an oil bath at 80 °C for 2 h to remove water and gases, then put into a Petri dish with a diameter of 60 mm which was located horizontally in the center of magnetron sputtering vacuum chamber, a stirrer was put under the PEG surface. PEG was under stirring (80 rpm) during sputtering. Pt (99.99% in purity, 50 mm in diameter, Tanaka Precious Metals, Japan) and Au (99.99% in purity, 50 mm in diameter, Tanaka) targets were used in this co-sputtering deposition, and elemental ratios were controlled by adjusting the sputtering current to each sputtering target. PEG and carbon-coated Cu transmission electron microscopy (TEM) grids (Nisshin EM, Japan) were used as the substrate for sputtering experiments. When a TEM grid was used as the substrate, it

was put in the center of the Petri dish. The center of the surface of PEG and of TEM grids was located at a distance of 110 mm from the two metal targets. The schematic illustration of the synthesis of Pt/Au alloy NPs via co-sputtering onto PEG is depicted schematically in Figure S1. After several times of gas-changing with inert Ar to remove O_2, the pressure of vacuum chamber was kept constant at 2 Pa. Cooling ethanol of 0 °C was used for cooling the metal target temperature during sputtering. In all the sputtering experiments, prior to collect NPs, Pt and Au targets were sputtered for 10 min to clean the target surface. During this period removable shutters located in front of metal targets and liquid polymer were used to prevent the materials from dropping onto the liquid polymer. Sputtering onto PEG was conducted for 30 min to 4 h while sputtering onto TEM grid was conducted for 1 to 30 s. The sputtering system was equipped with a thermocouple and a temperature control system to keep the substrate temperature at 30 °C.

4.2.2 Characterization

UV-vis spectrum was measured immediately after sputter deposition by JASCO V-630 spectrophotometer using a quartz cuvette having 1 mm optical path. All measurements were baseline corrected using empty quartz cuvette. Size and shape were observed by TEM (JEOL JEM-2010 and JEOL JEM-2000FX, 200 kV). High-resolution TEM (HR-TEM) and scanning TEM (STEM) images were obtained using a JEOL JEM-ARM200F, operating at 200, 120, and 80 kV. Samples for TEM,

HR-TEM, and STEM analysis were prepared by dipping a grid into PEG dispersion for a few seconds, then immediately dipping into ethanol for a few minutes to remove the excess amount of PEG, and finally drying in the air at room temperature for a few minutes. Size and size distribution were collected from TEM, HR-TEM, and STEM images by measuring approximately 300 particles in at least three different regions of the grid using ImageJ software. Crystal structure of NPs was evaluated using high-angle annular dark-field (HAADF)-STEM and X-ray diffraction (XRD, Rigaku Mini Flex II, Cu Ka radiation, λ = 1.5418 Å, scan speed of 0.5°/min). XRD samples were prepared by adding fumed silica into PEG-NPs dispersion to capture NPs and then centrifuged with methanol multiple times for isolating fumed silica supported NPs from PEG. The X-ray intensities for all samples were plotted as a function of 2 theta and were normalized. Elemental mapping using energy-dispersive X-ray spectroscopy (EDX) coupled with STEM and X-Ray Fluorescence (XRF, JSX-3100RII, JEOL) were carried out to verify the existence of Pt/Au alloy NPs and their composition. Particle composition distribution was examined with STEM-EDX line profile. Surface composition and surface chemical state of the samples were determined using a JEOL JPS-9200 X-ray photoelectron spectroscopy (XPS) device equipped with a monochromatic Al Kα X-ray source with 1486.6 eV operating at 100 W under ultrahigh vacuum (~ 5.0×10^{-7} Pa) conditions. The binding energy of Si 2p from the Si wafer substrate was used for charge correction. XPS samples were prepared by adding carbon black into PEG-NPs dispersion to capture NPs and then centrifuged with acetone several times for isolating carbon black supported NPs from

PEG, then dried under vacuum. XPS was also carried out on the Pt/Au NPs sputtered directly onto Si wafer. The weight of the sputtered material obtained on an aluminum foil under the same sputtering conditions was measured to estimate the amount of sputtered metal in PEG.

4.2.3 Computational methods

Density functional theory (DFT) calculations were carried out to investigate the interaction between PEG and NPs. All calculations are finished by GPAW, which is a real-space grid-based all-electron DFT code implemented in the projector augmented-wave formalism. In calculations, for simplifying the calculation, similar to the previous report, [45] OH-CH_2-CH_2-OH molecules was used by shortening the -CH_2-CH_2- chain to represent PEG (M_w = 600). And Au (Pt) (111) surface structure which consists of five Au (Pt) layers was used to represent NPs. And Perdew-Burke-Ernzerhof (PBE) functional was used for exchange-correlation, k-meshes of (3×3×1) was adopted for sampling Brillouin zones. The interaction of PEG with Au (Pt) surface was modeled by approaching PEG molecule close to surface to for a monodentate configuration. The configuration was relaxed until the maximum atomic force is less than 0.05eV/ Å.

The adsorption energy (E_{ad}) was calculated by

$$E_{ad}=E_{PEG+surface}-E_{PEG}-E_{surface} \quad (1)$$

Where $E_{PEG+surface}$ is the energy of the system containing PEG and Au (Pt)

surface. E_{PEG} and $E_{surface}$ are the energy of isolated PEG molecule and Au (Pt) surface, respectively.

To elucidate the growth of Pt/Au NPs, DFT calculations were also performed to study the formation energy of different metal clusters. According to the previous reports,[46,47] three reported stable Au (Pt) nanostructures were chosen, they are Pt_{20}, Au_{20}, Au_{25}, and a series nanostructures Pt_1Au_{24},Pt_2Au_{23}. Pt_1Au_{24} and Pt_2Au_{23} with a similar structure of Au_{25} were created.[46] For each structure, it was set at a large unit cell of (30×30×30) $Å^3$ to avoid the interaction with structure in neighboring cell. And in these calculations only Gamma point is used for sampling Brillouin zones and all atoms were relaxed until the atomic force is less than 0.05eV/Å.

The formation energies (E_f) of Pt_{20}, Au_{20}, Au_{25}, $Pt1Au_{25}$, and Pt_2Au_{23} are calculated by

$$E_f = E_{total} - nE_{ref} \quad (2)$$

Where E_{total} is the energy of a nanocluster in vacuum, n is the number of atoms in nanocluster, and E_{ref} is the energy of one Pt or Au atom in bulk.

4.3 Results and discussion

4.3.1 Pt/Au alloy NPs formed by simultaneous sputter deposition onto liquid PEG.

We found that using double head sputtering and liquid PEG, co-sputtering of Pt and Au is the most effective way to obtain alloy NPs. NPs produced by sputtering

onto PEG using different procedures (Table 4.1) were studied, that is, sputtering of only Pt (I), only Au (II), physical mixture of Pt and Au (III), step-wise sputtering of Pt then Au (IV) and Au then Pt (V), and co-sputtering of Pt and Au (VI).

Figure 4.1 shows the UV-vis absorption spectra of the NPs dispersion obtained by different preparation methods (Table 4.1). The corresponding TEM and STEM images can be found in Figures 4.2d and S2. The UV-vis spectrum of Pt NPs (I) exhibits monotonically increasing absorbance as wavelength decreased as reported.[36,48] UV-vis spectrum of Au NPs (II) shows the localized surface plasmon resonance (LSPR) peak at 542 nm and absorption at longer wavelength, which indicates the presence of Au and large agglomerate (Figure S2). The physical mixture (III) and step-wise sputtered samples (IV and V) of Pt and Au shows the LSPR absorption of Au around 542 nm.[32] The existence of Au was also confirmed by TEM (Figure S2) and EDX, in which, large agglomeration of 100 at.% Au and small Pt NPs co-exist. It has been reported that there is no LSPR peak of Pt/Au alloy NPs in UV-vis spectra while the absorbance of Pt/Au alloy NPs is monotonically increasing toward shorter wavelength.[35] Thus, step-wise sputtering of Pt and Au onto PEG (IV and V) resulted in physical mixtures of Pt and Au NPs, not alloy or core@shell NPs as it has been reported for AuPd alloy NPs,[48] Ag@Au and Ag@Pd core@shell structure[31] synthesized by successive sputtering of two metal targets onto ionic liquids. In contrast, co-sputtering (VI) onto PEG produced uniform Pt/Au NPs of 2.9 nm and LSPR peak at 542 nm was not observed in the UV-vis spectrum of the sample. The disappearance of plasmon resonance band is not due to the formation of small NPs (<

2 nm)[49] but owing to the presence of Pt in the bimetallic Pt/Au NPs, suppressing the LSPR peak of Au.[50] The results suggest the formation of Pt/Au alloy NPs by simultaneous sputtering.

Table 4.1 Summary of different preparation methods.

Preparation methods	**I**	**II**	**III**	**IV**	**V**	**VI**
Pt current/mA	50	0	50	50 (1^{st} sputter)	50 (2^{nd} sputter)	50
Au current/mA	0	50	50	50 (2^{nd} sputter)	50 (1^{st} sputter)	50
Note	Sputtering only Pt	Sputtering only Pt	Physical mixture of (I) and (II)	Stepwise sputtering	Stepwise sputtering	Co-sputtering

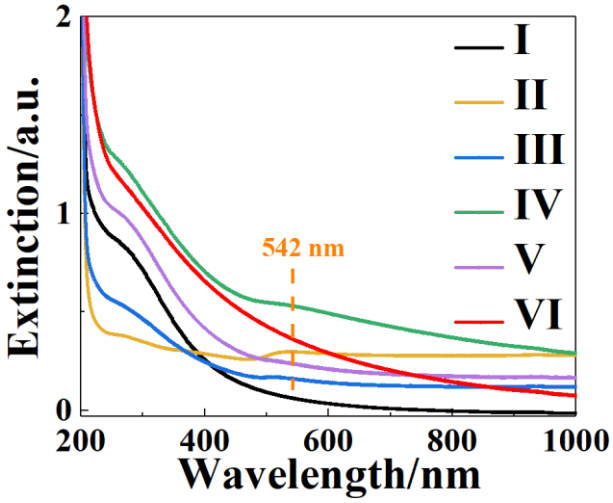

Figure 4.1 UV-vis absorption spectra of samples obtained by sputtering of only Pt (I), only Au (II), physical mixture of (I) and (II) samples (III), sputtering Pt target for 30 min followed by sputtering Au target for 30 min (IV), sputtering Au target for 30 min followed by sputtering Pt target for 30 min (V), and simultaneous sputtering of Pt and Au for 30 min (VI).

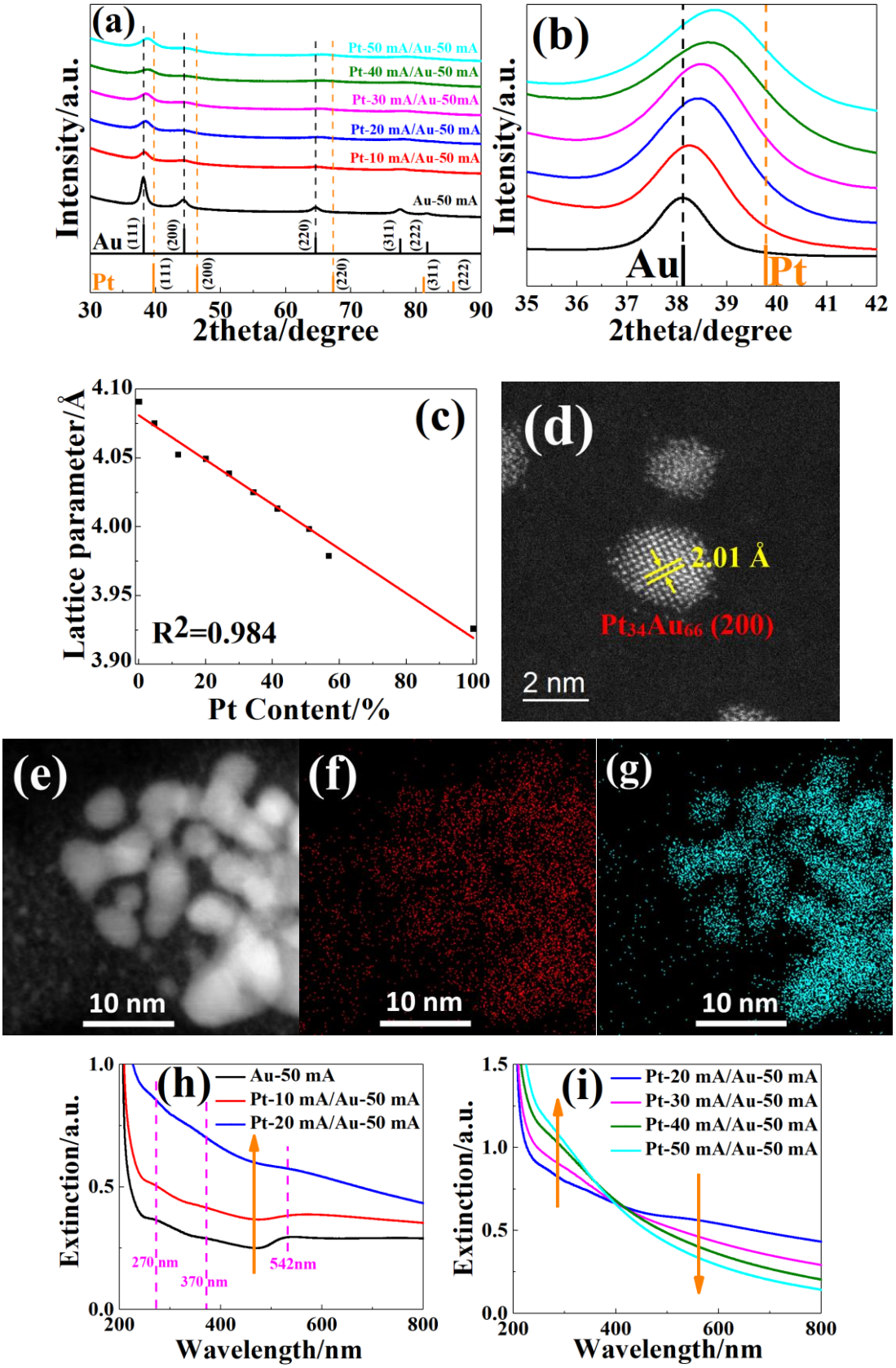

Figure 4.2 XRD patterns of Pt/Au NPs obtained via sputtering onto PEG under various sputtering current of Pt target from 0 (black), 10 (red), 20 (blue), 30 (pink), 40 (green) and

50 mA (cyan) while keeping sputtering current of Au target constant at 50 mA (a). XRD patterns in (a) in range of 2θ from 35.0° to 42° (b). Stick patterns are the reference patterns of Pt (JCPDS #04-0809) and Au (JCPDS #04-0784). The relation between the lattice parameter and Pt at. % of the bimetallic NPs (c); the data collecting from the samples of Pt-50 mA/Au-40 mA (41 at.% Pt), Pt-50 mA/Au-30 mA (51 at.% Pt), Pt-40 mA/Au-20 mA (57 at.% Pt), and Pt-50 mA-4 h (100 at.% Pt) were also used in this graph. HAADF-STEM image (JEOL JEM-ARM200F, operating at 200 kV) of Pt/Au NPs obtained by sputtering onto PEG under sputtering current of Pt-50 mA/Au-50 mA (d). HAADF-STEM image (JEOL JEM-ARM200F, operating at 120 kV) of Pt/Au NPs obtained by sputtering onto PEG under sputtering current of Pt-20 mA/Au-50 mA (e), corresponding STEM EDX-mapping images of Pt L (f) and Au L (g), UV-Vis absorption spectra of PEG-NPs dispersions produced by co-sputtering onto PEG using different sputtering current of Pt target from 0-20 mA (h) and 20-50 mA (i) while keeping sputtering current of Au target constant at 50 mA.

The bimetallic Pt/Au NPs prepared via co-sputtering onto PEG using various sputtering currents of Pt target, that is, 0 to 50 mA, while keeping sputtering current of Au target constant at 50 mA were collected and analyzed with XRD (Figure 4.2). XRD results (Figure 4.2a) reveal that all samples exhibited five characteristic diffraction peaks corresponding to the (111), (200), (220), (311), and (222) planes of fcc structure. The diffraction peaks of the Pt/Au alloy NPs located between the reference peaks of pure Pt and Au as shown in Figure 4.2a and 4.3b. This indicates the

formation of solid solution Pt/Au NPs. The (111) peaks of Pt/Au NPs (Figure 4.2b) shifted to higher 2θ angles in the direction from Au (111) peak to Pt (111) peak with increasing sputtering current of Pt. Such a shift can be caused by the difference in atomic radius of Pt and Au atoms in the substitutional Pt/Au solid solution and the increase in Pt content in the bimetallic NPs. Lattice parameters of Pt/Au NPs, calculated based on the measured 2θ values of (111) diffraction lines, were plotted in Figure 4.2c as a function of Pt at. % in Pt/Au NPs determined using XRF (Figure 3). The lattice constant of Pt/Au NPs is in between that of Pt (3.92 Å) and Au (4.08 Å) and exhibited a linear relationship with the Pt composition. This consists well with Vegard's law[51] as well as similar with reported results for Pt/Au alloy,[52] suggesting solid solution alloy formation in our samples. The broad peaks in Figure 4.2a-b demonstrate that the particles were nanocrystalline of average 3-10 nm (Figure S3) as also observed in TEM (Figure 4.3). The XRD peaks of Pt/Au NPs are broader compared with that of Au NPs which is owing to the smaller size of the Pt/Au NPs compared with the Au NPs (Figures S2 and 4.3).

Figure 4.2d is the STEM image of the sample that obtained by sputtering onto PEG with the sputtering current of Pt-50 mA/Au-50 mA. As shown in Figure 4.2d, the crystalline plane of the NPs can be observed, demonstrating an excellent crystallinity of Pt/Au alloy in the particle and the lattice spacing was 2.01 Å, corresponding to (200) plane of $Pt_{34}Au_{66}$. The HAADF-STEM images of NPs obtained by sputtering onto a TEM grid (Figure S4) also indicate simultaneous sputtering of Pt and Au leads to a random Pt/Au alloy. STEM-EDX mapping of Pt/Au with bigger sizes (sputtering

current of Pt and Au are 20 and 50 mA, respectively) shows the similar result (Figure 4.2e-g). No significant segregation of Pt and Au takes place in large agglomeration. However, it is noteworthy that there were Pt/Au NPs near the agglomeration which contains higher Pt content suggesting the elemental distribution was not homogenous in the samples that have agglomeration.

The presence of large aggregation of particles and big sized particles in Au-rich samples (Pt < 20 at.%, *e.g.* sputtering current of Au is 50 mA and sputtering currents of Pt are 20 mA) is also inferred from the existence of the LSPR of Au at 542 nm and absorbance in the long wavelength, that is, more than 550 nm, of the agglomerates in UV-vis spectra (Figure S5b and Figure 4.2h). On the other hand, there was neither LSPR peak of Au nor a clear absorbance in long wavelength for samples of more than 20 at.% Pt prepared using the sputtering current of 30-50 mA for Pt and sputtering current of 50 mA for Au target (Figure 4.2i). The absorption in short wavelength, 280 nm, increased and the absorption in long wavelength region, > 550 nm, decreased with increasing of Pt ratio, confirming the formation of individual Pt/Au alloy NPs with higher Pt content. This is consistent with XRD results (Figure 4.2a and 4.2b).

In our study, no precipitates inside the PEG liquid of all samples could be observed by the naked eye right after synthesis. However, PEG-Au dispersion tends to aggregate/precipitate with time whereas Pt/Au NPs dispersed in PEG appear to be fairly stable (Figure S5c), and the higher the Pt content, the more stable the dispersion. Namely, increasing Pt content will increase the stability of PEG-Pt/Au dispersion. A lot of articles also reported that the stability of Pt/Au NPs was enhanced by alloying

Au with Pt.[46]

4.3.2 Relation among the size, shape, and composition of the prepared NPs

A systematic study was conducted by keeping sputtering current for one target constant and varying the sputtering current for the other target from 0 to 50 mA. The TEM images, particle size, and the Pt at. % based on the XRF measurement of the resulting NPs are shown in Figure 4.3. Nominal Pt/Au atomic ratio measured from XRF is similar to that on the particle surface measured from XPS (Table S1). Noted that the statistical size distribution cannot be readily collected from the TEM images for the agglomeration. Two important tendencies were observed in the obtained NPs: (1) increasing Pt ratio in alloy sample result in termination of particle agglomeration and formation of individual NPs with a smaller size, and (2) the size and the composition of NPs are highly correlated for various couples of sputtering currents used in this study wherein NPs with similar composition have the same size.

It is observed that when keeping the sputtering current of Pt constant, *e.g.*, 50 mA, an increase in sputtering current of Au resulted in bigger NPs (Figures 3 and 4a-e). This is a common sense because using higher sputtering current produces more metal atom and cluster for the growth of particles. A similar phenomenon was also commonly observed for monometallic NPs prepared via sputtering onto liquids.[36] In contrast, when sputtering current of Au was kept constant, for example 50 mA, an

increase in the sputtering current of Pt from 0 mA to 50 mA resulted in the morphology changes from agglomeration state (sputtering current of Pt from 0 to 30 mA) to individual particle state (sputtering current of Pt from 30 to 50 mA) with a decrease in particle size (Figure 4e-g). A similar tendency was observed in other cases (other rows in Figure 4.3) when keeping the sputtering current of Au constant and increasing the sputtering current of Pt. It is well-known that increasing the sputtering current of Pt also increases the amount of Pt atoms/clusters in the liquid. However, different from what observed when increasing sputtering current of Au, an increase in the amount of Pt atoms/clusters did not make the bimetallic Pt/Au alloy NPs bigger but terminated the formation of agglomeration and reduced the particle sizes (Figures 5 and S3). Over all, it was observed in Figure 4.3 that severe aggregation and large size particles occurred in Au and Au rich samples with Pt less than 16 at. % (left side of Figure 4.3). Only individual NPs without aggregation were observed when there was more than 27 at.% of Pt. Figure 4.5 shows the relation of particle size and Pt atomic percentage for samples that contain individual NPs as seen in Figure 4.3. It is obvious that the size decreased in the order of Au NPs > Pt/Au NPs > Pt NPs, which is in good agreement with the previous results,[32, 50] and smaller Pt/Au NPs contained more Pt. These results strongly indicate the particle size and whether the resulting Pt/Au alloy is individual particle or aggregate were determined by the composition, that is, Pt/Au atomic ratio, rather than the sputtering currents themselves which determine the amounts of atoms/clusters and particles in the liquid at present conditions. In other words, under a certain concentration of NPs in PEG (sputtering

currents 50 mA or less and sputtering time of 30 min), the particle size and agglomeration state are a function of particle composition.

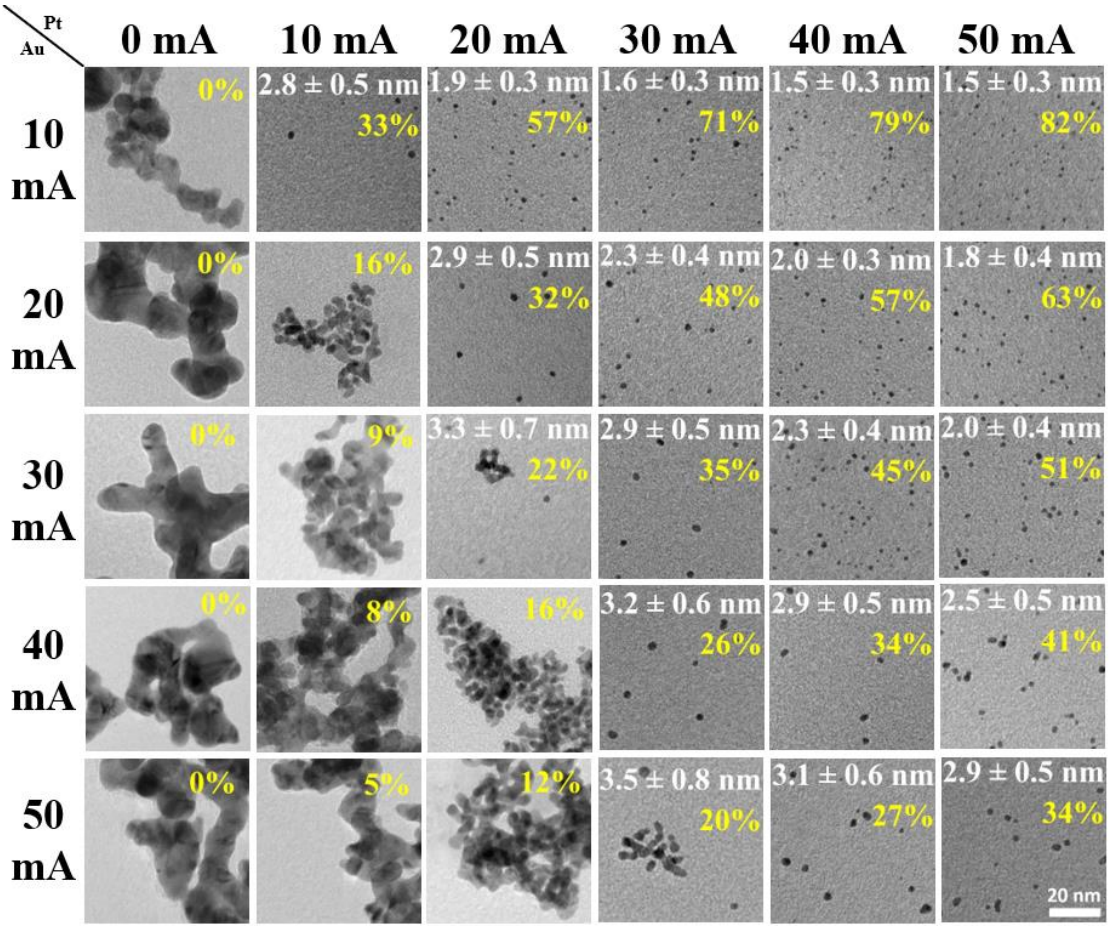

Figure 4.3 TEM images of NPs dispersed in PEG obtained by sputtering onto PEG using different sputtering currents of Pt and Au targets (0-50 mA). Particles in the same column were obtained using the same sputtering current for Pt with increasing sputtering current for Au from top to bottom. Particles in the same row were obtained using the same sputtering current for Au with an increase of sputtering current for Pt from left to right. Numbers as insets show particle size (in white text) and composition (in yellow text) of the bimetallic Pt/Au NPs in term of Pt at. %. The scale bar in the image is 20 nm.

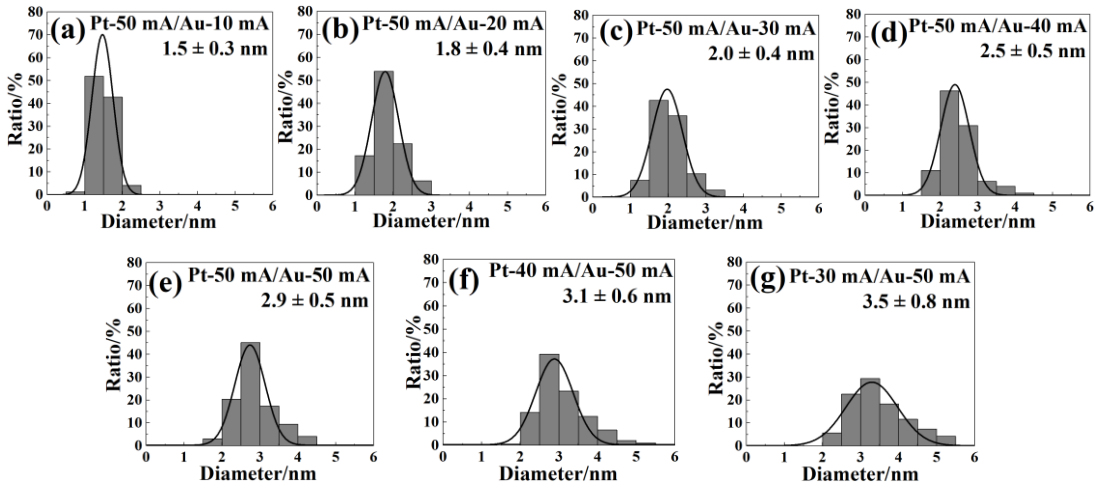

Figure 4.4 Size distributions of NPs obtained by sputtering onto PEG using different sputtering currents of Au target: 10 (a), 20 (b), 30 (c), 40 (d), 50 mA (e) while keeping sputtering current of Pt target constant at 50 mA, and using different sputtering currents of Pt target: 40 mA (f) and 30 mA (g) while keeping sputtering current for Au target constant at 50 mA.

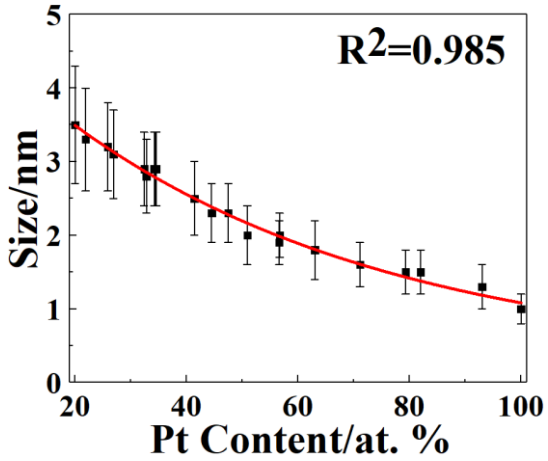

Figure 4.5 Relation between NP size and Pt atomic content, the fitting curve is based on the Boltzmann model. The R^2 value for the nonlinear fit of the data is 0.985. The data collecting from the samples of Pt-50 mA/Au-5 mA (93 at. % Pt) and Pt-50 mA (100 at. % Pt) were also used in this graph.

We also found Pt can terminate agglomeration of Ag particles (Figure S6) and agglomeration disappeared when Au alloy with Ag or Cu (Figure S7). Similar phenomena were also reported by other groups, for example, Hirano *et al.* and Chang *et al.* showed the size of Pd/Au bimetallic NPs decreased when Pd content increased.[54,55] However, correlations of size and composition in the above-mentioned studies are rather ambiguous and the underlying reasons have not been elucidated.

The second aspect in size-composition dependency is that Pt/Au NPs exhibited the same size for the same composition no matter the sputtering current used.

Figure S8 shows histograms of NP size obtained for samples with Pt of about 32-35 at.% (Figure 4.3) obtained with various sputtering current for Au and Pt target. Corresponding photographs of PEG-NPs dispersions and UV-Vis spectra can be found in Figure S9. It can be seen from Figure 4.3, NPs having close-to-spherical shape, an average size of 2.9 nm and a standard deviation of 0.5 nm (Figure S8) were observed without the formation of large agglomerates in all cases despite the sputtering current of both Pt and Au targets increased from 10 mA to 50 mA. Namely, with increasing the total amount of metal by increasing the sputtering current, the size and size distribution of particles with the same nominal composition are basically preserved. It seems that the size of the metal NPs is mainly controlled by Pt/Au atomic ratio rather than by the sputtering current under investigated conditions: sputtering onto PEG for 30 min and the upper limit of sputtering current is 50 mA. Similar results were observed for particles of 57 at.% Pt (sputtering currents Au-10 mA/Pt-20 mA, Au 20-mA/Pt-40 mA) and of 45-48 at. % Pt (Au-30 mA/Pt-40 mA, Au

20-mA/Pt 30-mA) as shown in Figure 4.3. However, in our previous study, under similar sputtering conditions, that is, sputtering time of 30 min and sputtering current in the range of 10 to 50 mA, larger Pt NPs and Pt/Cu NPs were obtained when applying a higher sputtering current.[36,42]

In order to check the concentration range of metal in PEG that the NPs exhibit the same size for the same composition as shown in Figure 4.3 and Figure S8, we measured the amount of metal deposited onto PEG for 30 min at various sputtering currents, that is, Pt-10 mA/Au-10 mA, Pt-20 mA/Au-20 mA, Pt-30 mA/Au-30 mA, Pt-40 mA/Au-40 mA, and Pt-50 mA/Au-50 mA. The results (Table S2) indicate that 5.6 mg metal was produced in 10 cm^3 of PEG at the highest sputtering current of 50 mA and for that amount of metal, Pt/Au NPs with a composition of 34 at.% Pt can preserve their size of 2.9 ± 0.5 nm. In order to increase the amount of metals in PEG and see if secondary aggregation and growth occurred, a longer time of sputtering was used for two samples, that is, Pt-20 mA/Au-20 mA and Pt-50 mA/Au-50 mA. Sputtering for 4 h with sputtering currents of 20 mA for Pt and Au produced 12 mg of metal in PEG which is double the amount of metals sputtered at 50 mA for 30 min (Table S2). The NPs appeared in individual with maintaining an average particle size of 2.9 nm, but their size distribution became wider compared with that of the samples sputtered for 30 min using sputtering currents 20 and 50 mA (Figure S10). This suggests growth of NPs for a higher amount of sputtered metals with the same Pt/Au ratio. More obvious secondary aggregation and growth were observed for sample sputtered at 50 mA with total of 44.8 mg of metal in PEG (Figure S10) wherein NP

size was 4.5 ± 1.8 nm. These results remind us that the same composition results in the similar size should be restricted in a certain condition wherein the amounts of metal in 10 cm^3 PEG below 5.6 mg (*e.g.* sputtering time of 30 min, sputtering current no more than 50 mA). Longer sputtering time, that is, 4 h, could give enough high particle concentration for effective collision, consequently, the difference in particle size for the same composition could be detected.

However, in the 30 min-sputtering, the obtained particles were single crystals, whereas the obtained particles of 4 h-sputtering of Pt-50 mA/Au-50 mA were polycrystals (Figure S10c), indicating the secondary growth occurs. Thus, the results above-mentioned is a clear indication that there is a relation exists among size, composition, and atom concentration in the first growth of particle.

4.3.3 Possible formation mechanism.

The above experimental results of co-sputtering of Pt/Au show a strong correlation of compositions, sizes and shapes. We have found the capability of Pt to terminate the agglomeration of Au, producing smaller Pt/Au NPs at higher content of Pt, and for certain range of metal concentration in PEG, NPs having the same composition showed the same size. To elucidate the underlying reasons for the formation of Pt/Au NPs, DFT calculation, STEM-EDX mapping, and line profile were carried out.

4.3.3.1 High Au content results in agglomeration and high Pt content results in small alloy particle size

As we observed that Cu[42] and Au NPs (Figure S5c) in PEG aggregated and finally precipitated after keeping for several days whereas Pt in PEG were very stable in PEG even after keeping for two years, which drives us to consider that the interactions between different metal NPs and PEG are different. If the interaction between Pt atoms and PEG is favorable compared with Au atoms, we can expect that Pt NPs can be well protected, the growth of Pt NPs and NPs with high Pt content in PEG during sputtering or storage should be very slow. To get the insights into the chemical interactions between the different NPs and PEG, DFT calculation were carried out, the structures and results are shown in Figure S11 and Table 4.2. It seems that PEG molecule adsorbed more favorably on Pt than Au because the calculated adsorption energy of PEG-Pt is almost twice larger compared with the PEG-Au (0.20 eV vs 0.12 eV) and the bond length of O-Pt atom is shorter than O-Au atom (2.424 Å vs 3.133 Å). Furthermore, in the same Pt/Au ratio structure, it also appears that PEG molecule energetically prefer to adsorb on Pt compared with Au because when PEG molecule adsorb on Pt atom, the calculated adsorption energy is higher compared with the that of Au atom (0.19 eV vs 0.07 eV and 0.11 eV vs 0.09 eV) and the bond length of O-Pt atom is shorter than O-Au atom (2.483 Å vs 2.756 Å and 3.010 Å vs 2.797 Å). Based on these results, we suggest that it is because that Pt clusters can be well protected by PEG compared with Au clusters, clusters with high Pt content are difficult to grow, results in the formation of small particle, while clusters with high

Au content will easily grow during sputtering, as a result, larger particle formed; when Au content higher than 84% (at.%), agglomeration formed.

Table 4.2 DFT calculated adsorption energy and bond length between the model PEG molecule and different surfaces.

Structure	Adsoption atom	Adsorption energy (eV)	Bond length of O-metal atom (Å)
Pt	(a) PEG adsorbed on Pt	-0.20	2.424
Pt/Au (One Pt atom substituted by one Au atom in structure (a))	(b) PEG adsorbed on Pt	-0.19	2.483
	(c) PEG adsorbed on Au	-0.07	2.756
Au	(d) PEG adsorbed on Au	-0.12	3.133
Pt/Au (One Au atom substituted by one Pt atom in structure (d))	(e) PEG adsorbed on Au	-0.09	3.010
	(f) PEG adsorbed on Pt	-0.11	2.797

However, when sputtering onto solid substrate (TEM grid), we also find increasing Pt content results in the formation of smaller particle. Figures S12-S15 show that STEM images of NPs prepared by sputtering onto TEM grid for 1 s under various sputtering currents of Pt for each sputtering current of Au (0, 20, 40, and 50 mA). When only Au was sputtered for 1 s at sputtering current from 20 to 50 mA, both Au atoms and NPs were observed. The sizes of Au NPs increase with increasing the sputtering current (Figures S13a, S14a, and S15a). When only Pt was sputtered for 1 s at 10 mA only Pt atoms were observed on the TEM grid (Figure S12). An increase

in sputtering current of Pt to 20 mA resulted in the formation of Pt nanoclusters and NPs aside from Pt atoms. When the sputtering current of Pt was increased from 20 to 50 mA, more Pt NPs and less Pt atoms were observed. The sizes of Pt NPs also increase with increasing the sputtering current, which is similar to Au.

When the sputtering current of Au was set at 20 mA and applying current on Pt target, the particle sizes decrease when the sputtering current of Pt was increased from 0 to 10 mA and then increase when the sputtering current of Pt was further increased to 50 mA (Figure S13). Similar results were also observed when the sputtering current of Au was set as 40 and 50 mA whereas sputtering current of Pt was increased from 10 to 50 mA (Figures S14 and S15).

By sputtering onto TEM grid for a longer time, that is 30 s, the particle sizes also decrease first (Figure S16a-c), then increase, and finally, particles agglomerate severely (Figure S16d-f) when keeping the sputtering current of Au as 50 mA and increasing the sputtering current of Pt from 0 to 50 mA. The phenomenon was observed for Pt/Au sputtered onto the TEM grid for various sputtering times from 1 to 30 s (Figure S17). The decrease in the particle size of Pt/Au NPs first when increasing the sputtering of Pt from 0 to 20 mA occurred in all the cases. We also found similar results for co-sputtering of Au and another metal target such as Cu and Ag. The increase of particle size and severe agglomeration by sputtering for a long time or at high sputtering currents is due to the attachment and growth of a large number of sputtered atoms/clusters particles on the solid substrate where they cannot move freely. The decrease in particle size for an increase in the sputtering current of the second

target in co-sputtering, on the other hand, is evidence of the interaction and alloying of two types of metal elements. Combined with the results obtained by sputtering onto PEG, we can conclude that even a small amount of Pt can induce a pronounced change of particle size via alloying with Au.

Our DFT calculation result shows that formation energy, E_f, of Pt_{20} and Au_{20} with a structure of 20 atoms are 28.81 and 12.66 eV respectively, where their corresponding structural model can be found in the reference.[49] The results indicate that Pt_{20} has higher formation energy than Au_{20}. Moreover, it has been reported that in clusters with a fixed number of Pt atoms, the formation energy of the cluster decreases with the increase of the number of Au atoms,[56] whereas, in clusters with a fixed number of Au atoms, the formation energy of the cluster increases with the increase of the number of Pt atoms.[56] The reduction of the formation energy makes the NP formation become easier. As a result, a larger particle can be formed when more Au is in the particle to reduce the formation energy. On the other hand, when more Pt is in the particle, to increase the formation energy of the particle, the size of the particle should be smaller. From this point of view, we can explain our experimental result illustrated in Figure 4.6. When the sputtering current of Au is increased, more Au atoms can be ejected, leading to a higher content of Au in the NPs, and thus larger NPs can be obtained. On the other hand, when the sputtering current of Pt is increased, more Pt atoms can be ejected, thereby the formation energy of NPs will be increased, making the NP formation more difficult. Thus, the smaller NPs containing a smaller number of Pt atoms per particles can be formed. The result is

illustrated in Figure 4.6.

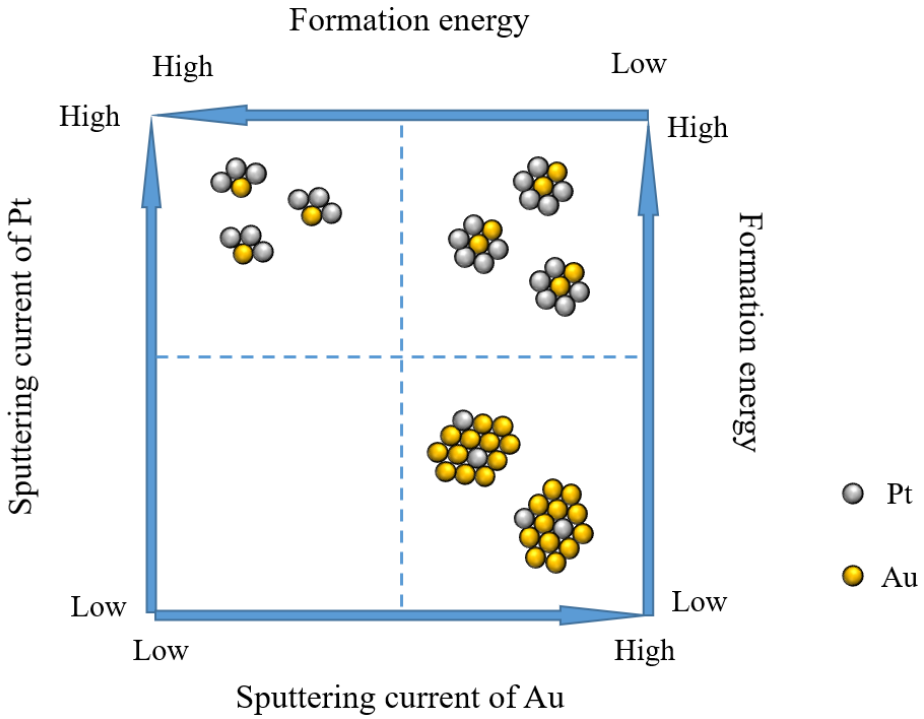

Figure 4.6 Schematic diagram illustrates the relation of sputtering current, formation energy, and particle size: when Pt content is increased, the formation energy of the particles is increased, and hence this results in the formation of smaller particles.

4.3.3.2 Same nominal composition gives a similar alloy particle size

The experimental results reveal an interesting finding that the particles with the same nominal composition have similar sizes for various pairs of sputtering currents. To explain for each nominal composition why higher sputtering currents, which produce more metal atoms for particle growth, do not result in larger particle size, we consider several factors. The elemental distribution in individual nanoparticle can be

inhomogeneous. This is at least observed in the agglomeration rich in Au (Figure 4.2). The cohesive energy and surface energy of Pt are higher than that of Au, suggesting that Au can be preferentially orient toward the surface.[47,57] If this occurs during particle formation and growth, the particles tend to grow bigger and form agglomerates as observed in Au rich samples. On the other hand, because the formation energy of Pt is higher than that of Au and higher Pt content on the particle surface can stop the particle growth, we suspect that the growth of particle can be stopped when the Pt/Au atomic ratio on the surface is higher than the average atomic ratio.

We could not trace the growth process of Pt/Au particles, but STEM-EDX mapping and line profile (Figure 4.7, Table 4.3) of Pt/Au NPs obtained in PEG provide an evidence in support for the contention that a slightly higher Pt/Au atomic ratio is obtained for surface as compared to the nominal bulk values. Thus it could be concluded that a random alloy structure with Pt-rich surface is formed in Pt-50 mA/Au-50 mA sample. Although the use of co-sputtering deposition appears to prevent the segregation of the two metals into separate particles, metal mobility within these particles, changing in surface atomic distribution during particle growth, and the subsequent surface-enrichment effect cannot be ruled out. Aside from Pt/Au NPs with Pt rich on the surface, we also found Pt/Au NPs with homogeneous element distribution.

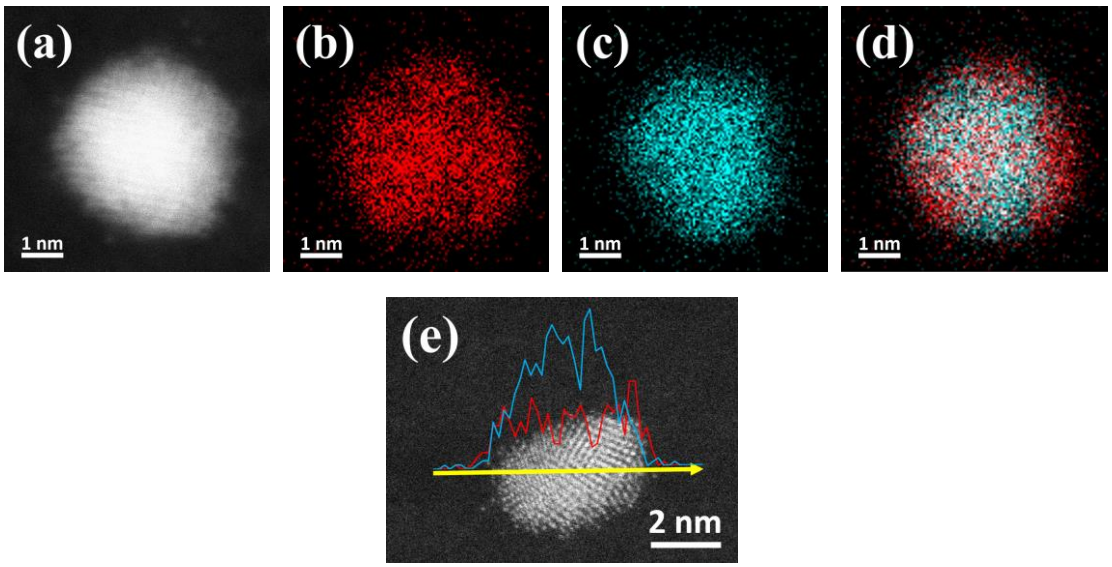

Figure 4.7 HAADF image (a) and EDX mapping results of the sample obtained by sputtering onto PEG at sputtering current of Pt-50 mA/Au-50 mA for Pt L (b), Au L (c), and overlap image of Pt and Au (d). EDX-line profile results (e) of the Pt L (red line)/Au L (blue line) for another nanoparticle of the sample. ((a)-(d) were obtained by JEOL JEM-ARM200F, operating at 80 kV, (e) were obtained by JEOL JEM-ARM200F, operating at 200 kV.)

Table 4.3 EDX results of particle shown in Figure 4.11a-d.

	Site		
	center	edge (0.5 nm from the surface)	average
Composition (Pt at.%)	32.63	52.47	37.16

We do not know the exact reason for the surface rich Pt. To shed some light on the interaction between Pt and Au atoms we have conducted illustrative calculations of the formation energy of model Au_{25},[46] Pt_1Au_{24}, and Pt_2Au_{23} clusters in which the position of Pt atoms can be inside or on the surface of the clusters (Figure 4.8). From our previous report,[36] not only NP but also small clusters and free atom were obtained. Thus, we can believe that the initial cluster can be the formation of a few atoms. Therefore, although Au_{25}, Pt_1Au_{24}, and Pt_2Au_{23} clusters are smaller than NPs obtained in our experiments, they are sufficient to investigate the relation between formation energy and alloy affect. Figure 4.8 shows the DFT optimized model of Au_{25} (Figure 4.8a), Pt_1Au_{24} clusters (Pt atom on the surface (Figure 4.8b) and Pt atom in the center (Figure 4.8c)), and Pt_2Au_{23} clusters (Pt atoms on the surface (Figure 4.8d) and Pt atoms in the center (Figure 4.8e)). DFT results are summarized in Table 4.4. The formation energies of Pt_1Au_{24} and Pt_2Au_{23} cluster are higher than Au_{25}, this can be attributed to the much higher cohesive energy of Pt than that of Au. The formation energy of the structure where Pt atom on the surface is slightly lower than that of Pt atom in the center, suggesting the clusters prefer the structures that Pt stays on the surface of the cluster. This is consistent with the EDX-mapping and line profile results, however, different from the result in the reported paper.[56]

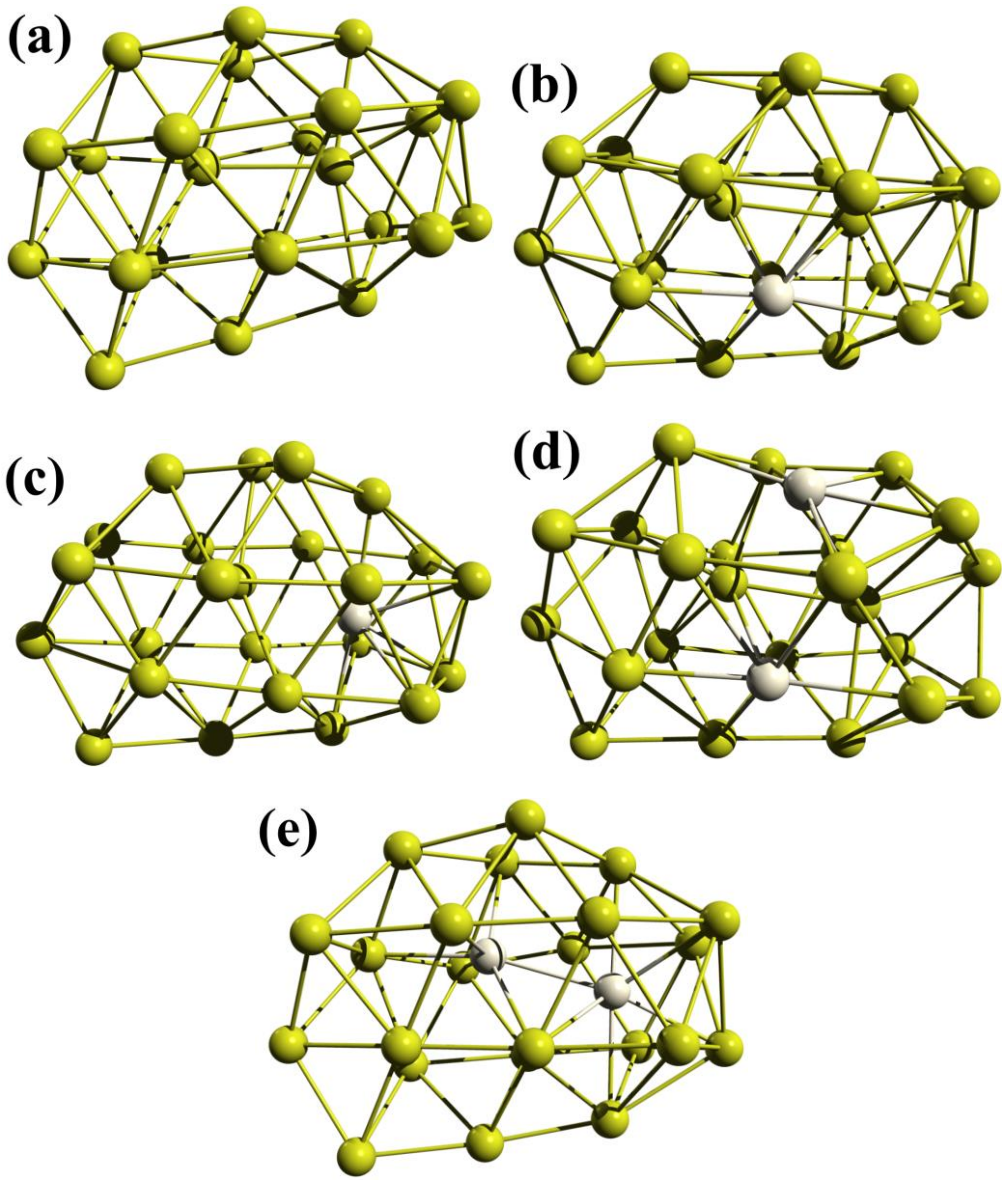

Figure 4.8 DFT-simulated Au_{25} (a), Pt_1Au_{24} with Pt atom on the surface (b), Pt_1Au_{24} with Pt atom in the center (c), Pt_2Au_{23} with Pt atoms on the surface (d), and Pt_2Au_{23} with Pt atoms in the center (e) clusters. Au and Pt atoms are shown in yellow and gray respectively.

Table 4.4 Formation energy of different structures of Au_{25}, Pt_1Au_{24}, and Pt_2Au_{23}.

Structure	Formation energy (eV)	Note
Au_{25}	16.80	-
Pt_1Au_{24}	17.13	Pt atom on the surface
Pt_1Au_{24}	17.16	Pt atom in the center
Pt_2Au_{24}	17.68	Pt atoms on the surface
Pt_2Au_{24}	17.77	Pt atoms in the center

Combined with the discussion of interaction between different metal atoms and PEG molecule, we suggest a possible formation process as shown in Figure 4.9. Since PEG adsorb on Pt atom stronger than Au atom, the NP formed by colliding with the part which contain high Au content on the small clusters selectively, as a result, the surface of the NP will increase as grow, corresponding to the fact that Pt atom prefers to stay on the surface of the NP. When Pt/Au ratio on the surface of the particle reaches to a certain value, it needs a lot of energy to form a bigger particle which cannot be satisfied in the present situation, as a result, the growth stops. Therefore, particle with same Pt/Au ratio results in similar size even the sputtering current varied.

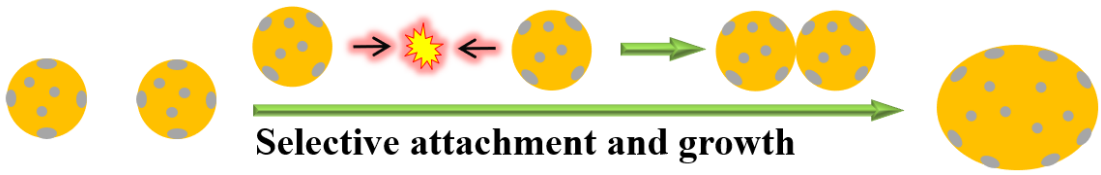

Figure 4.9 Schematic illustration for the formation of Pt/Au alloy NPs by sputtering deposition of Pt and Au onto PEG.

Consequently, based on the experimental results and calculation results, we conclude that particles with same nominal composition had similar size can be caused by slightly higher Pt content on the particle surface compared with the inside of the particles. Therefore, although increasing the sputtering current can create higher amount of sputtered materials, the high Pt content on the particle surface still make the particle growth become more difficult, and stop the growth at a certain size.

4.4 Conclusions

In summary, we have successfully demonstrated that the well-controlled Pt/Au alloy NPs with tunable composition was fabricated at room temperature by means of a co-sputtering method, despite the fact that the bulk metals exhibit a miscibility gap. The formation mechanism of Pt/Au NPs was investigated for the first time.

In our approach, the control of particle size, morphology, composition, and alloy formation was obtained by simply control of the sputtering parameter at the present experimental conditions. Our results show that the composition of Pt and Au can be modulated from ca. 20 to 100 atom % Pt in individual Pt/Au alloy NPs. In addition, the shape of the NPs generated at high Pt content (Pt at.% > 27%) is spherical, the shape irregularity increases with an increase of the Au content. A decrease in the particle size with increasing Pt content is observed and particles with the same composition have similar sizes. The STEM-EDS results show that in comparison to the nominal composition, there are more Pt existing in the edge of the nanoparticle

and more Au existing in the center of the nanoparticle. The formation mechanism of alloy NPs, especially Pt/Au alloy NPs, in co-sputtering system was elucidated for the first time. Size, shape, and agglomeration degree of Pt/Au NPs are key points for their applications. Our findings in the relation among particle size, particle composition, and agglomeration state of the formed NPs with respect to their composition can shed light into the formation mechanism of Au-based and Pt-based alloy NPs and have profound implications to the design of Au-based and Pt-based alloys in liquid. The atomic-level alloy of Pt/Au NPs with variable and controllable sizes are expected to be useful as effective catalysts for various reactions.

4.5 References

1. Choi, K. M.; Na, K.; Somorjai, G. A.; Yaghi, O. M., Chemical environment control and enhanced catalytic performance of platinum nanoparticles embedded in nanocrystalline metal–organic frameworks. J. Am. Chem. Soc. 2015, 137(24), 7810-7816.

2. Taylor, M. J.; Durndell, L. J.; Isaacs, M. A.; Parlett, C. M.; Wilson, K.; Lee, A. F.; Kyriakou, G., Highly selective hydrogenation of furfural over supported Pt nanoparticles under mild conditions. Appl. Catal. B 2016, 180, 580-585.

3. Liu, S.; Tian, N.; Xie, A.-Y.; Du, J.-H.; Xiao, J.; Liu, L.; Sun, H.-Y.; Cheng, Z.-Y.; Zhou, Z.-Y.; Sun, S.-G., Electrochemically seed-mediated synthesis of sub-10 nm tetrahexahedral Pt nanocrystals supported on graphene with improved catalytic performance. J. Am. Chem. Soc. 2016, 138(18), 5753-5756.

4. Hvolbæk, B.; Janssens, T. V.; Clausen, B. S.; Falsig, H.; Christensen, C. H.; Nørskov, J. K., Catalytic activity of Au nanoparticles. Nano Today 2007, 2(4), 14-18.

5. Peng, S.; Lee, Y.; Wang, C.; Yin, H.; Dai, S.; Sun, S., A facile synthesis of monodisperse Au nanoparticles and their catalysis of CO oxidation. Nano Res. 2008, 1(3), 229-234.

6. Zhang, P.; Qiao, Z.-A.; Jiang, X.; Veith, G. M.; Dai, S., Nanoporous ionic organic networks: stabilizing and supporting gold nanoparticles for catalysis. Nano Lett. 2015, 15(2), 823-828.

7. Yonezawa, T.; Toshima, N., Polymer- and micelle-protected gold/platinum bimetallic systems. Preparation, application to catalysis for visible-light-induced

hydrogen evolution, and analysis of formation process with optical methods. J. Mol. Catal. 1993, 83, 167-181.

8. Zhao, L.; Thomas, J. P.; Heinig, N. F.; Abd-Ellah, M.; Wang, X.; Leung, K., Au-Pt alloy nanocatalysts for electro-oxidation of methanol and their application for fast-response non-enzymatic alcohol sensing. J. Mater. Chem. C 2014, 2(15), 2707-2714.

9. Bian, H.; Nguyen, N. T.; Yoo, J.; Hejazi, S.; Mohajernia, S.; Müller, J.; Spiecker, E.; Tsuchiya, H.; Tomanec, O.; Sanabria-Arenas, B. E., Forming a highly active, homogeneously alloyed AuPt co-catalyst decoration on TiO2 nanotubes directly during anodic growth. ACS Appl. Mater. Interfaces 2018, 10(21), 18220-18226.

10. Brown, B.; Wolter, S. D.; Stoner, B. R.; Glass, J. T., Alloying effects of cosputtered gold-platinum thin films on the oxygen reduction reaction in acidic electrolyte. J. Electrochem. Soc. 2008, 155(8), B852-B859.

11. Zhang, J.; Chen, G.; Guay, D.; Chaker, M.; Ma, D., Highly active PtAu alloy nanoparticle catalysts for the reduction of 4-nitrophenol. Nanoscale 2014, 6 (4), 2125-2130.

12. Zhou, S.; Jackson, G. S.; Eichhorn, B., AuPt Alloy Nanoparticles for CO-Tolerant Hydrogen Activation: Architectural Effects in Au-Pt Bimetallic Nanocatalysts. Adv. Funct. Mater. 2007, 17(16), 3099-3104.

13. Xiao, S.; Hu, W.; Luo, W.; Wu, Y.; Li, X.; Deng, H., Size effect on alloying ability and phase stability of immiscible bimetallic nanoparticles. Eur. Phys. J. B 2006, 54(4), 479-484.

14. Mihut, C.; Descorme, C.; Duprez, D.; Amiridis, M. D., Kinetic and spectroscopic characterization of cluster-derived supported Pt–Au catalysts. J. Catal. 2002, 212(2), 125-135.

15. Xu, J.; Zhao, T.; Liang, Z.; Zhu, L., Facile preparation of AuPt alloy nanoparticles from organometallic complex precursor. Chem. Mater. 2008, 20(5), 1688-1690.

16. Gu, W.; Deng, X.; Jia, X.; Li, J.; Wang, E., Functionalized graphene/Fe3O4 supported AuPt alloy as a magnetic, stable and recyclable catalyst for a catalytic reduction reaction. J. Mater. Chem. A 2015, 3(16), 8793-8799.

17. Chan-Thaw, C. E.; Chinchilla, L. E.; Campisi, S.; Botton, G. A.; Prati, L.; Dimitratos, N.; Villa, A., AuPt Alloy on TiO_2: A Selective and Durable Catalyst for l-Sorbose Oxidation to 2-Keto-Gulonic Acid. ChemSusChem 2015, 8(24), 4189-4194.

18. Wu, W.; Tang, Z.; Wang, K.; Liu, Z.; Li, L.; Chen, S., Peptide templated AuPt alloyed nanoparticles as highly efficient bi-functional electrocatalysts for both oxygen reduction reaction and hydrogen evolution reaction. Electrochim. Acta 2018, 260, 168-176.

19. Li, D.; Wang, C.; Tripkovic, D.; Sun, S.; Markovic, N. M.; Stamenkovic, V. R., Surfactant removal for colloidal nanoparticles from solution synthesis: the effect on catalytic performance. ACS Catal. 2012, 2(7), 1358-1362.

20. Wanjala, B. N.; Luo, J.; Fang, B.; Mott, D.; Zhong, C.-J., Gold-platinum nanoparticles: alloying and phase segregation. J. Mater. Chem. 2011, 21(12), 4012-4020.

21. Bian, T.; Zhang, H.; Jiang, Y.; Jin, C.; Wu, J.; Yang, H.; Yang, D., Epitaxial growth

of twinned Au-Pt core-shell star-shaped decahedra as highly durable electrocatalysts. Nano Lett. 2015, 15(12), 7808-7815.

22. Zhao, J.; Baibuz, E.; Vernieres, J.; Grammatikopoulos, P.; Jansson, V.; Nagel, M.; Steinhauer, S.; Sowwan, M.; Kuronen, A.; Nordlund, K., Formation mechanism of Fe nanocubes by magnetron sputtering inert gas condensation. ACS Nano 2016, 10(4), 4684-4694.

23. Izumi, R.; Yao, Y.; Tsuda, T.; Torimoto, T.; Kuwabata, S., Oxygen reduction electrocatalysts sophisticated by using Pt nanoparticle-dispersed ionic liquids with electropolymerizable additives. J. Mater. Chem. A 2018, 6(25), 11853-11862.

24. Liu, C.-H.; Mao, B.-H.; Gao, J.; Zhang, S.; Gao, X.; Liu, Z.; Lee, S.-T.; Sun, X.-H.; Wang, S.-D., Size-controllable self-assembly of metal nanoparticles on carbon nanostructures in room-temperature ionic liquids by simple sputtering deposition. Carbon 2012, 50(8), 3008-3014.

25. Nguyen, M. T.; Yonezawa, T., Sputtering onto a liquid: interesting physical preparation method for multi-metallic nanoparticles. Sci. Tech. Adv. Mater. 2018, 19(1), 883-898.

26. Ishida, Y.; Corpuz, R. D.; Yonezawa, T., Matrix Sputtering Method: a Novel Physical Approach for Photoluminescent Noble Metal Nanoclusters. Acc. Chem. Res. 2017, 50(12), 2986-2995.

27. Suzuki, S.; Tomita, Y.; Kuwabata, S.; Torimoto, T., Synthesis of alloy AuCu nanoparticles with the L1 0 structure in an ionic liquid using sputter deposition. Dalton Trans. 2015, 44(9), 4186-4194.

28. Sugioka, D.; Kameyama, T.; Kuwabata, S.; Yamamoto, T.; Torimoto, T., Formation of a Pt-Decorated Au Nanoparticle Monolayer Floating on an Ionic Liquid by the Ionic Liquid/Metal Sputtering Method and Tunable Electrocatalytic Activities of the Resulting Monolayer. ACS Appl. Mater. Interfaces 2016, 8(17), 10874-10883.

29. König, D.; Richter, K.; Siegel, A.; Mudring, A. V.; Ludwig, A., High-Throughput Fabrication of Au-Cu Nanoparticle Libraries by Combinatorial Sputtering in Ionic Liquids. Adv. Funct. Mater. 2014, 24(14), 2049-2056.

30. Wender, H.; de Oliveira, L. F.; Migowski, P.; Feil, A. F.; Lissner, E.; Prechtl, M. H.; Teixeira, S. R.; Dupont, J., Ionic liquid surface composition controls the size of gold nanoparticles prepared by sputtering deposition. J. Phys. Chem. C 2010, 114(27), 11764-11768.

31. Liu, C.-H.; Chen, X.-Q.; Hu, Y.-F.; Sham, T.-K.; Sun, Q.-J.; Chang, J.-B.; Gao, X.; Sun, X.-H.; Wang, S.-D., One-pot environmentally friendly approach toward highly catalytically active bimetal-nanoparticle-graphene hybrids. ACS Appl. Mater. Interfaces 2013, 5(11), 5072-5079.

32. Wender, H.; de Oliveira, L. F.; Feil, A. F.; Lissner, E.; Migowski, P.; Meneghetti, M. R.; Teixeira, S. R.; Dupont, J., Synthesis of gold nanoparticles in a biocompatible fluid from sputtering deposition onto castor oil. Chem. Commun. 2010, 46(37), 7019-7021.

33. Ishida, Y.; Sumi, T.; Yonezawa, T., Sputtering synthesis and optical investigation of octadecanethiol-protected fluorescent Au nanoparticles. New J. Chem. 2015, 39(8), 5895-5897.

34. Sumi, T.; Motono, S.; Ishida, Y.; Shirahata, N.; Yonezawa, T., Formation and optical properties of fluorescent gold nanoparticles obtained by matrix sputtering method with volatile mercaptan molecules in the vacuum chamber and consideration of their structures. Langmuir 2015, 31(14), 4323-4329.

35. Suzuki, S.; Suzuki, T.; Tomita, Y.; Hirano, M.; Okazaki, K.-i.; Kuwabata, S.; Torimoto, T., Compositional control of AuPt nanoparticles synthesized in ionic liquids by the sputter deposition technique. CrystEngComm 2012, 14(15), 4922-4926.

36. Deng, L.; Nguyen, M. T.; Yonezawa, T., Sub-2 nm Single-Crystal Pt Nanoparticles via Sputtering onto a Liquid Polymer. Langmuir 2018, 34(8), 2876-2881.

37. Nguyen, M. T.; Zhang, H.; Deng, L.; Tokunaga, T.; Yonezawa, T., Au/Cu Bimetallic Nanoparticles via Double-Target Sputtering onto a Liquid Polymer. Langmuir 2017, 33(43), 12389-12397.

38. Cha, I. Y.; Ahn, M.; Yoo, S. J.; Sung, Y.-E., Facile synthesis of carbon supported metal nanoparticles via sputtering onto a liquid substrate and their electrochemical application. RSC Adv. 2014, 4(73), 38575-38580.

39. Nguyen, M. T.; Yonezawa, T.; Wang, Y.; Tokunaga, T., Double target sputtering into liquid: A new approach for preparation of Ag–Au alloy nanoparticles. Mater. Lett. 2016, 171, 75-78.

40. Ishida, Y.; Akita, I.; Sumi, T.; Matsubara, M.; Yonezawa, T., Thiolate–Protected Gold Nanoparticles Via Physical Approach: Unusual Structural and Photophysical Characteristics. Sci. Rep. 2016, 6, 29928.

41. Hatakeyama, Y.; Morita, T.; Takahashi, S.; Onishi, K.; Nishikawa, K., Synthesis of

gold nanoparticles in liquid polyethylene glycol by sputter deposition and temperature effects on their size and shape. J. Phys. Chem. C 2011, 115(8), 3279-3285.

42. Deng, L.; Nguyen, M. T.; Mei, S.; Tokunaga, T.; Kudo, M.; Matsumura, S.; Yonezawa, T., Preparation and growth mechanism of Pt/Cu alloy nanoparticles by sputter deposition onto a liquid polymer. Langmuir 2019, 35(25), 8418-8427.

43. Chau, Y.-t. R.; Deng, L.; Nguyen, M. T.; Yonezawa, T., Monitor the Growth and Oxidation of Cu-nanoparticles in PEG after Sputtering. MRS Adv. 2019, 4(5-6), 305-309.

44. Chung, M. W.; Cha, I. Y.; Ha, M. G.; Na, Y.; Hwang, J.; Ham, H. C.; Kim, H.-J.; Henkensmeier, D.; Yoo, S. J.; Kim, J. Y., Enhanced CO2 reduction activity of polyethylene glycol-modified Au nanoparticles prepared via liquid medium sputtering. Appl. Catal. B 2018, 237, 673-680.

45. Carette, X., Debièvre, B., Cornil, D.,Cornil, J., Leclère, P., Maes, B., Gautier, N., Gautron, E., Mel, A. E., Raquez, J., On the Sputtering of Titanium and Silver onto Liquids, Discussing the Formation of Nanoparticles. The Journal of Physical Chemistry C 2018, 122(46): 26605-26612.

46. De Bas, B. S.; Ford, M.; Cortie, M., Low energy structures of gold nanoclusters in the size range 3–38 atoms. Journal of Molecular Structure: THEOCHEM 2004, 686(1-3), 193-205.

47. Selvarani, G.; Selvaganesh, S. V.; Krishnamurthy, S.; Kiruthika, G.; Sridhar, P.; Pitchumani, S.; Shukla, A., A methanol-tolerant carbon-supported Pt− Au alloy cathode catalyst for direct methanol fuel cells and its evaluation by DFT. J. Phys.

Chem. C 2009, 113(17), 7461-7468.

48. Zhang, H.; Toshima, N., Synthesis of Au/Pt bimetallic nanoparticles with a Pt-rich shell and their high catalytic activities for aerobic glucose oxidation. J. Colloid Interface Sci. 2013, 394, 166-176.

49. Liu, C.-H.; Liu, R.-H.; Sun, Q.-J.; Chang, J.-B.; Gao, X.; Liu, Y.; Lee, S.-T.; Kang, Z.-H.; Wang, S.-D., Controlled synthesis and synergistic effects of graphene-supported PdAu bimetallic nanoparticles with tunable catalytic properties. Nanoscale 2015, 7(14), 6356-6362.

50. Alvarez, M. M.; Khoury, J. T.; Schaaff, T. G.; Shafigullin, M. N.; Vezmar, I.; Whetten, R. L., Optical absorption spectra of nanocrystal gold molecules. J. Phys. Chem. B 1997, 101(19), 3706-3712.

51. Scott, R. W.; Wilson, O. M.; Oh, S.-K.; Kenik, E. A.; Crooks, R. M., Bimetallic palladium− gold dendrimer-encapsulated catalysts. J. Am. Chem. Soc. 2004, 126(47), 15583-15591.

52. Denton, A. R.; Ashcroft, N. W., Vegard's law. Phys. Rev. A 1991, 43(6), 3161.

53. Schrinner, M.; Proch, S.; Mei, Y.; Kempe, R.; Miyajima, N.; Ballauff, M., Stable bimetallic gold–platinum nanoparticles immobilized on spherical polyelectrolyte brushes: synthesis, characterization, and application for the oxidation of alcohols. Adv. Mater. 2008, 20(10), 1928-1933.

54. Hirano, M.; Enokida, K.; Okazaki, K.-i.; Kuwabata, S.; Yoshida, H.; Torimoto, T., Composition-dependent electrocatalytic activity of AuPd alloy nanoparticles prepared via simultaneous sputter deposition into an ionic liquid. Phys. Chem. Chem. Phys.

2013, 15(19), 7286-7294.

55. Chang, J.-B.; Liu, C.-H.; Liu, J.; Zhou, Y.-Y.; Gao, X.; Wang, S.-D., Green-chemistry compatible approach to TiO_2-supported PdAu bimetallic nanoparticles for solvent-free 1-phenylethanol oxidation under mild conditions. Nano-Micro Lett. 2015, 7(3), 307-315.

56. Ge, Q.; Song, C.; Wang, L., A density functional theory study of CO adsorption on Pt-Au nanoparticles. Comput. Mater. Sci. 2006, 35 (3), 247-253.

5. General conclusion

This study demonstrates that highly dispersed and stable monometallic and bimetallic NPs can be synthesized by sputter deposition method. In the second chapter, we proposed to use sputtering of Pt onto PEG to study the size, fine structure, and growth of the obtained Pt NPs. Various sputter currents were used to finely tailor particle size in sub-2 nm range, i.e. 0.9-1.4 nm, with high uniformity. The as-synthesized Pt NPs were found to have single crystal structure instead of aggregation of several Pt clusters. We further found that beside the Pt NPs, in the as-prepared dispersion there are Pt atoms and this contribute to the subsequent growth of Pt to certain stable sizes (1.6-1.7 nm) in PEG. Noticeably, the dispersion in PEG was colloidal stable for more than 5 months. Thus, the findings of this study can advance the current interdisciplinary research in using physical vacuum technique and chemistry for control particle size and understand the growth of the sputtered NPs.

In chapter 3, we proposed to use sputtering of a Pt/Cu alloy target onto liquid polyethylene glycol, PEG, and solid substrate for the study of the size, fine structure, and growth of Pt/Cu alloy NPs of ca. 0.9 nm to 3.1 nm. Sputtering parameters related to the particle growth, i.e., substrate, sputtering current, stirring speed, sputtering period, sputtering time, and PEG temperature, have been varied systematically and their impact on particle size have been observed and evaluated. The results clearly evidenced the growth process of Pt/Cu after landing on the PEG surface. In particular, cluster growth occurred to some extent on the PEG surface in a short time, then the

alloy Pt/Cu NPs experienced further growth in the bulk liquid, and finally the formed NPs were stabilized in the liquid PEG for long time storage, i.e., a year. When sputtering was divided into multiple short periods (few seconds) with an interval between two periods, the particle size decreases compared with long periods sputtering (tens of seconds to 30 min). On the other hand, high sputtering current, a lower stirring speed, and a long sputtering time produced larger Pt/Cu NPs and aggregates instead of small single-crystalline NPs. These key findings allowed us to differentiate the growth of Pt/Cu alloy NPs on the liquid polymer surface and inside the bulk liquid polymer for the first time. These fundamental understandings lead to the fine control and manipulation of the desired particle size. Furthermore, comparison of the Pt/Cu, Pt, and Cu NPs obtained via sputtering onto PEG shed light on the elemental dependent nanoparticle growth and stability. This result is important as a guide for the study of co-sputtering for multiple metal alloy NPs wherein the interactions of particles of different metal elements on the liquid surface and inside the liquid influence in not only the size but also composition of the obtained NPs.

The fourth chapter aimed to finely control size and composition of Pt/Au alloy NPs by using double target sputtering. We found that Pt/Au alloy NPs were successfully obtained in a wide range of composition and sizes by appropriate control of the sputtering conditions. The particle size, morphology, composition, and alloy formation are strongly correlated. That is, NPs generated at high Pt content (Pt at.%>27%) are spherical and well-dispersed whereas the irregularity and aggregation of particles increase with high Au content. Increasing Pt content results in a smaller

Pt/Au NPs. Further, Pt/Au NPs with the same composition have similar sizes for various pairs of sputtering currents applying on Pt and Au targets. The formation mechanism and growth of Pt/Au NPs are elucidated by a combination of experimental results and DFT calculation for the first time. DFT calculation indicates that PEG molecule energetically prefers to adsorb on Pt compared with Au is the cause of the smaller particle size associated with high Pt content. On the other hand, both experimental and simulation results reveal that the surface rich Pt can be attributed for the capability of stopping particle growth, leading to the same size of NPs with the same composition despite using higher sputtering currents. Our findings in the relation among particle size, particle composition, and aggregation state of the formed NPs with respect to its composition can shed light into the formation mechanism of Au-based and Pt-based alloy NPs. The atomic-level alloy of variable-size and size-controlled Pt/Au NPs are expected to be useful as effective catalysts for various reactions.

Appendix I. Supplementary information for chapter 2

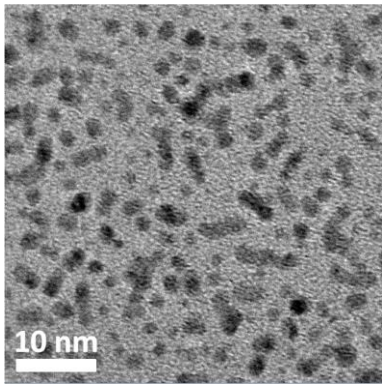

Figure S1. TEM image of NPs obtained by sputtering onto PEG under sputtering current of 50 mA for 2 h.

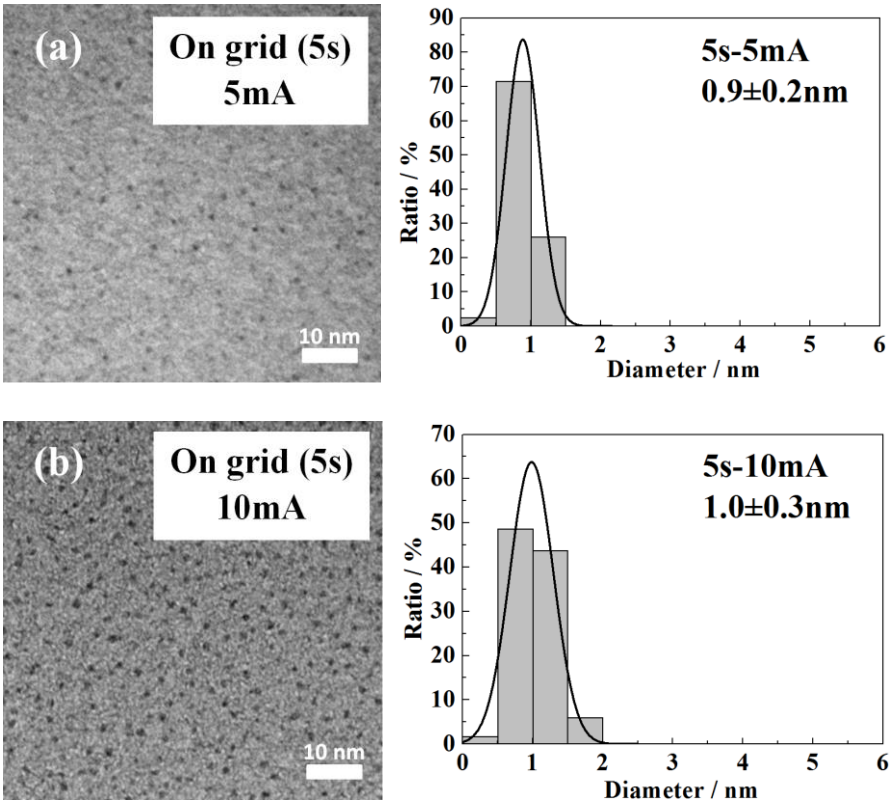

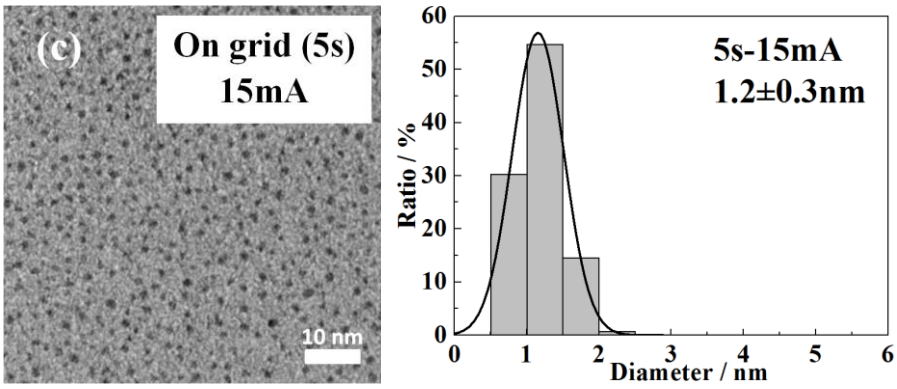
(c)
On grid (5s)
15mA
10 nm
5s-15mA
1.2±0.3nm
Ratio / %
Diameter / nm

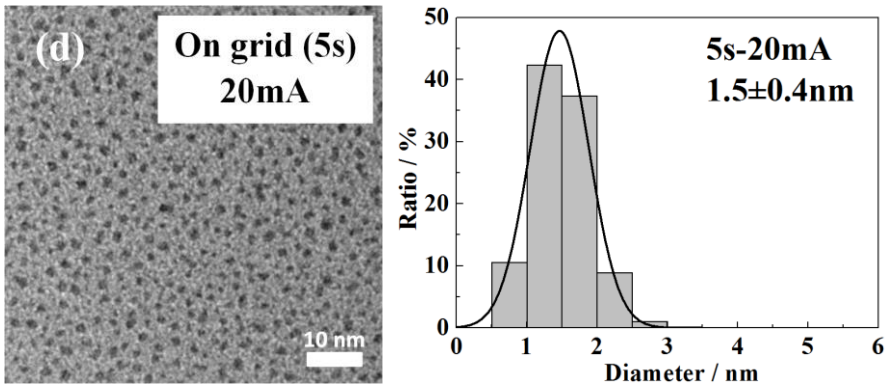
(d)
On grid (5s)
20mA
10 nm
5s-20mA
1.5±0.4nm
Ratio / %
Diameter / nm

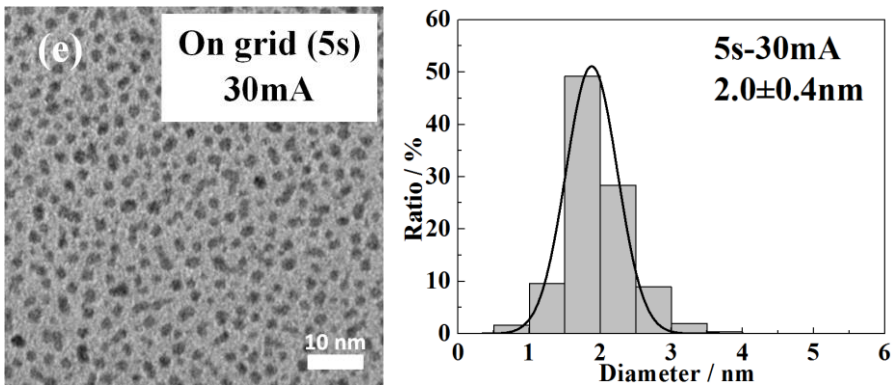
(e)
On grid (5s)
30mA
10 nm
5s-30mA
2.0±0.4nm
Ratio / %
Diameter / nm

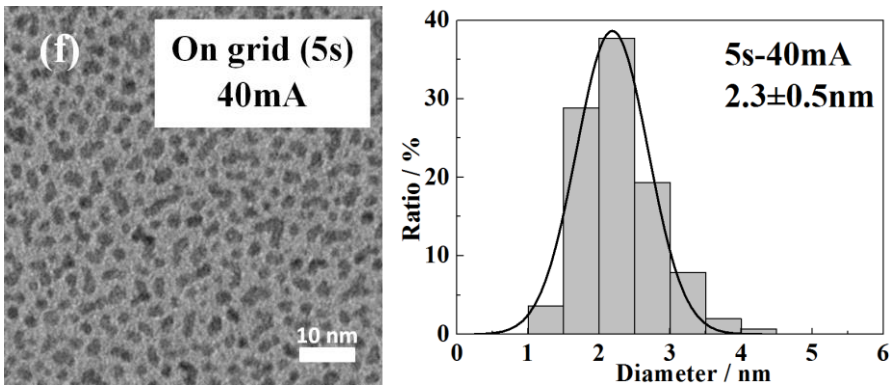
(f)
On grid (5s)
40mA
10 nm
5s-40mA
2.3±0.5nm
Ratio / %
Diameter / nm

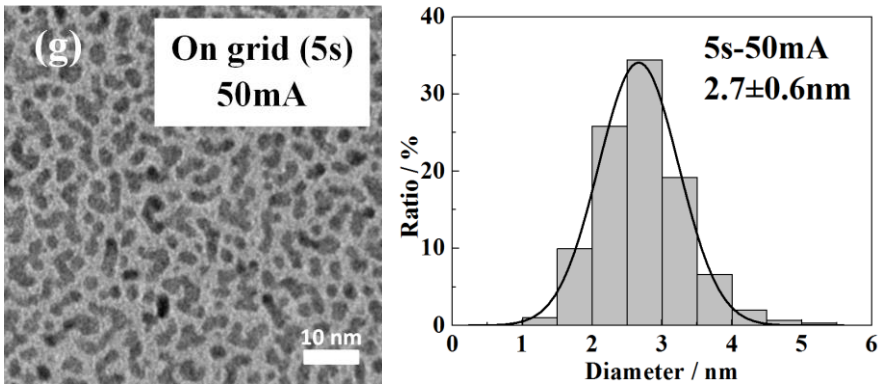

Figure S2. TEM images and size distributions of NPs obtained by sputtering on TEM grid for 5 s under sputtering current of (a) 5 mA, (b) 10 mA, (c) 15 mA, (d) 20 mA, (e) 30 mA, (f) 40 mA, (g) 50 mA.

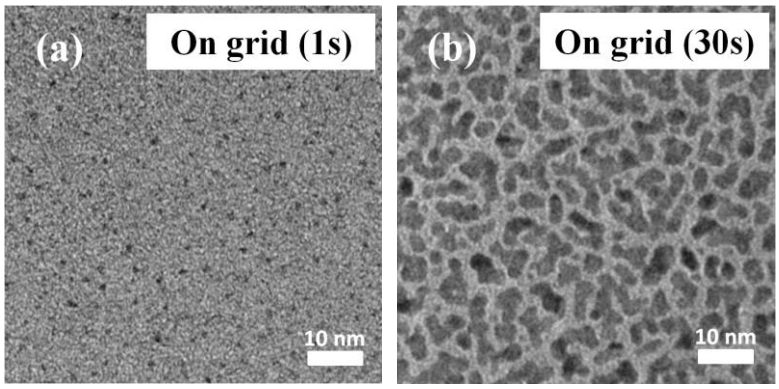

Figure S3. TEM images of NPs obtained by sputtering on TEM grid for (a) 1 s and (b) 30 s under sputtering current of 20 mA.

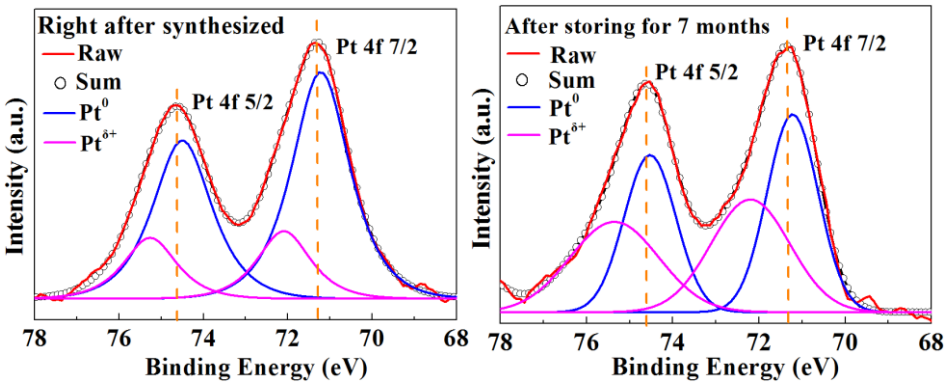

Figure S4. XPS spectra of as-synthesized and 7 months stored Pt NPs. The surface atomic content of Pt(0) decrease from 77 at.% in as-synthesized sample to 52 at.% after 7 months storage.

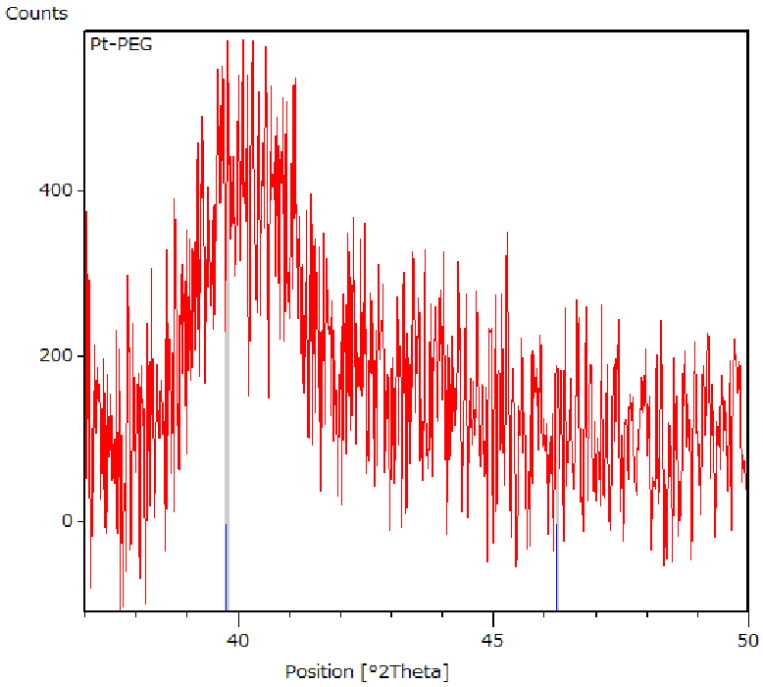

Figure S5. XRD pattern of Pt NPs obtained in PEG after 30 min sputtering using a current of 50 mA. The stick pattern is the reference of Pt (PDF number 04-0809)

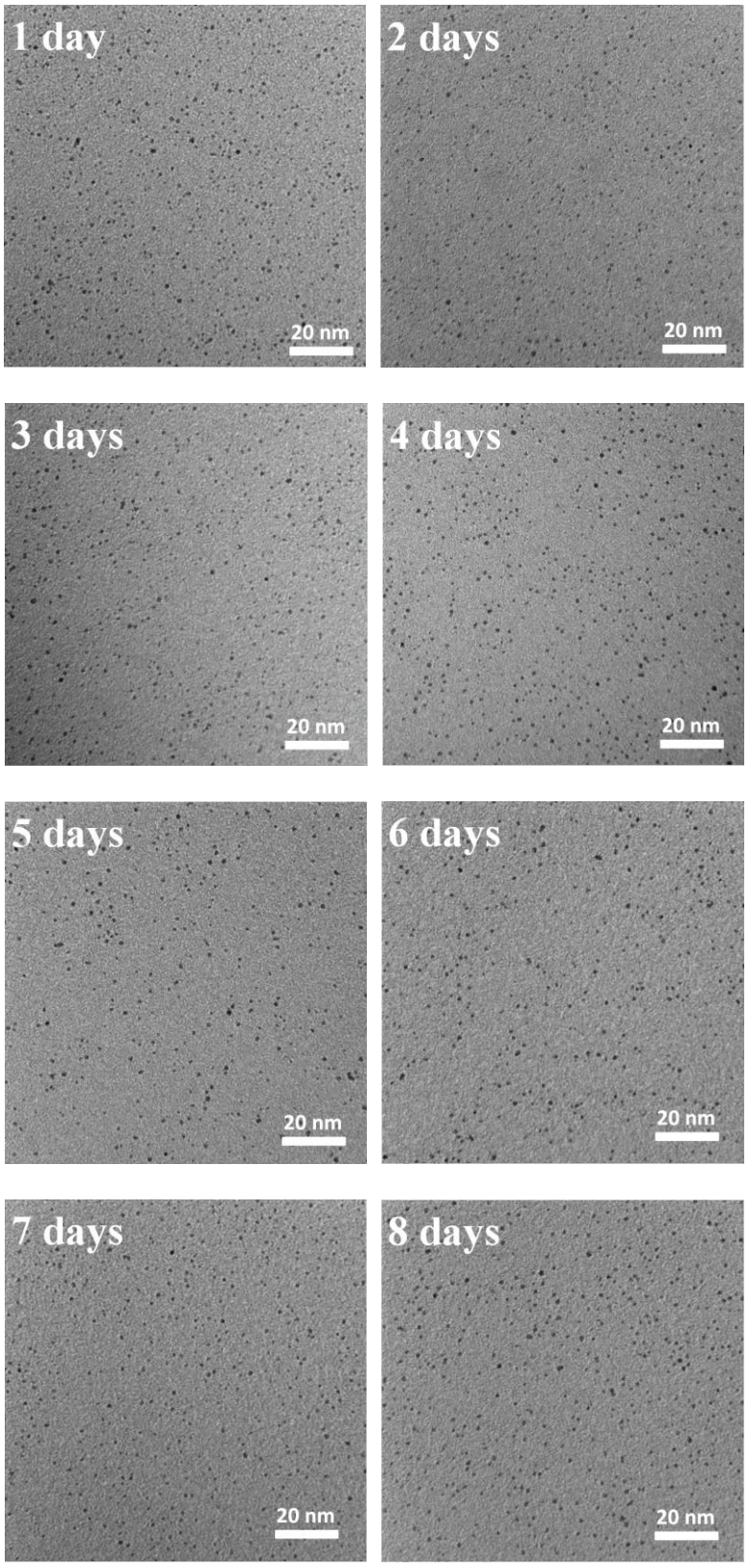
1 day
20 nm
2 days
20 nm
3 days
20 nm
4 days
20 nm
5 days
20 nm
6 days
20 nm
7 days
20 nm
8 days
20 nm

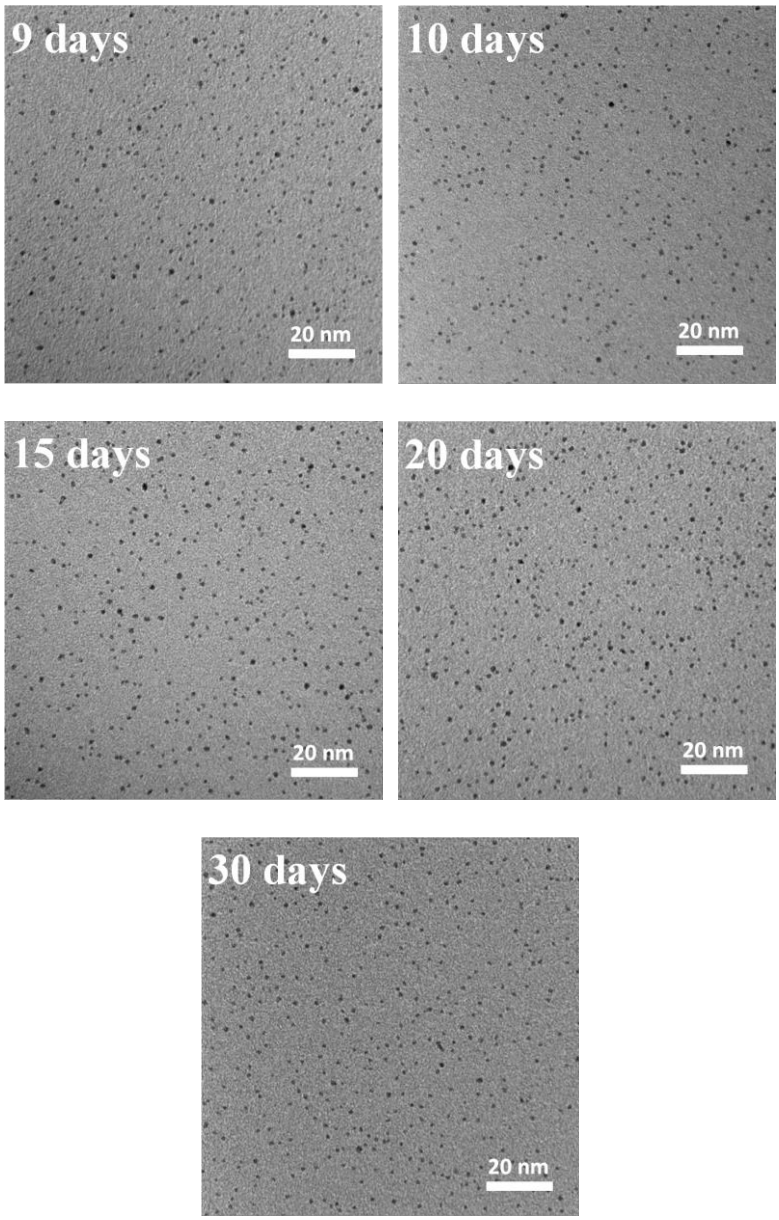

Figure S6. TEM images of sputtered Pt NPs using sputtering current of 20 mA for 30 min onto PEG then the dispersion was stored in dark at room temperature for 1-30 days.

Appendix II. Supplementary information for Chapter 3

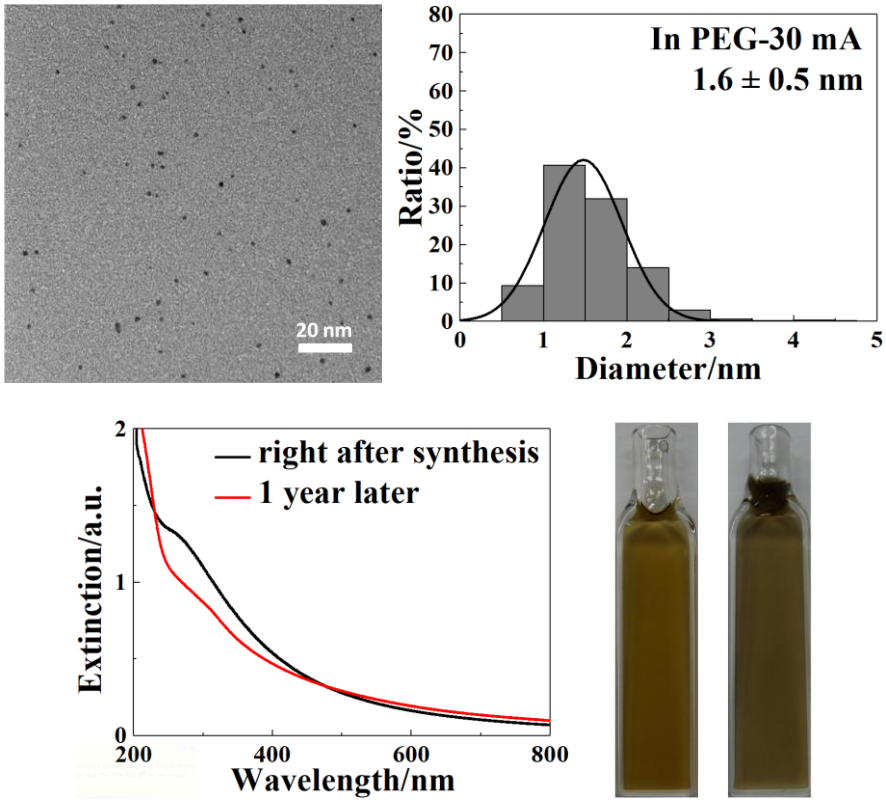

Figure S1. TEM image of NPs after keeping for 1 year obtained by continuously sputtering onto PEG under sputtering current of 30 mA and corresponding size distribution, UV-Vis spectra and photographs of PEG-NPs dispersion (left: right after synthesis and right: one year later) under room light.

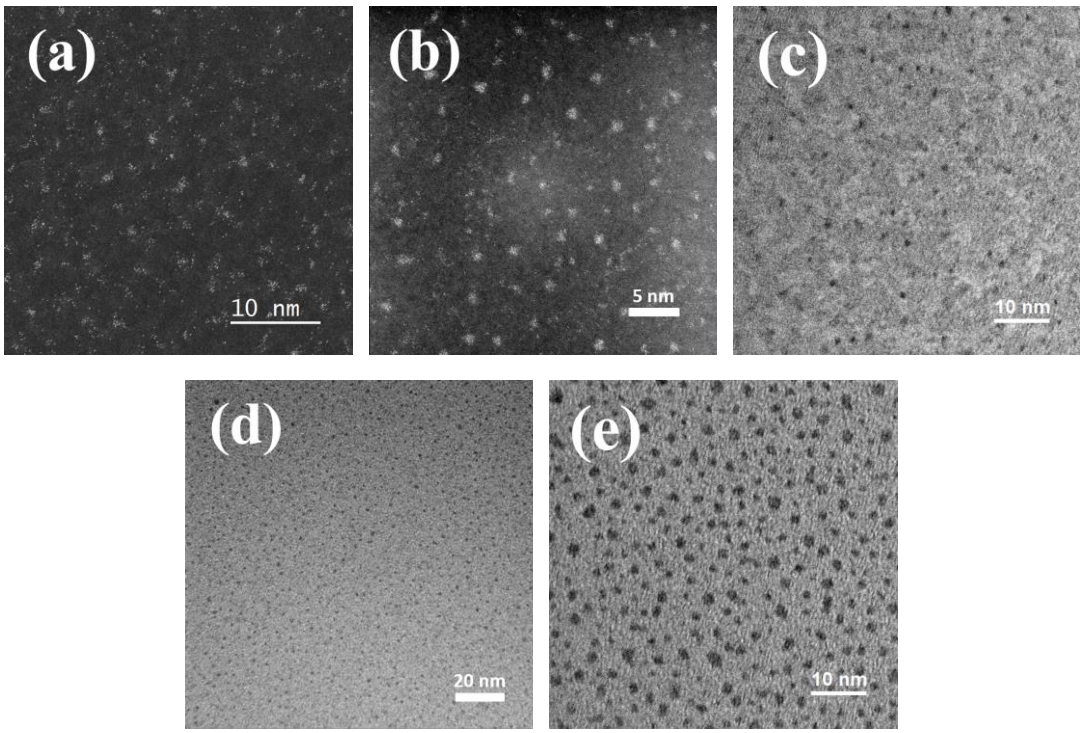

Figure S2. TEM, HR-TEM and STEM images of NPs obtained by sputtering onto TEM grid for 1 s under sputtering current of (a) 10 mA (STEM), (b) 20 mA (STEM), (c) 30 mA (HR-TEM), (d) 40 mA (TEM) (e) 50 mA (HR-TEM).

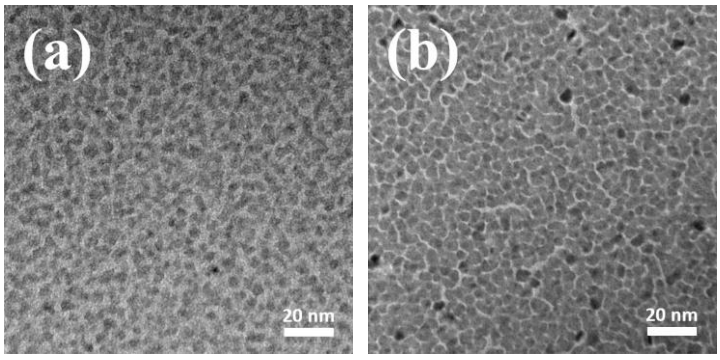

Figure S3. TEM images of NPs obtained by sputtering onto TEM grid under sputtering current of 30 mA for 30 s (a) and 60 s (b).

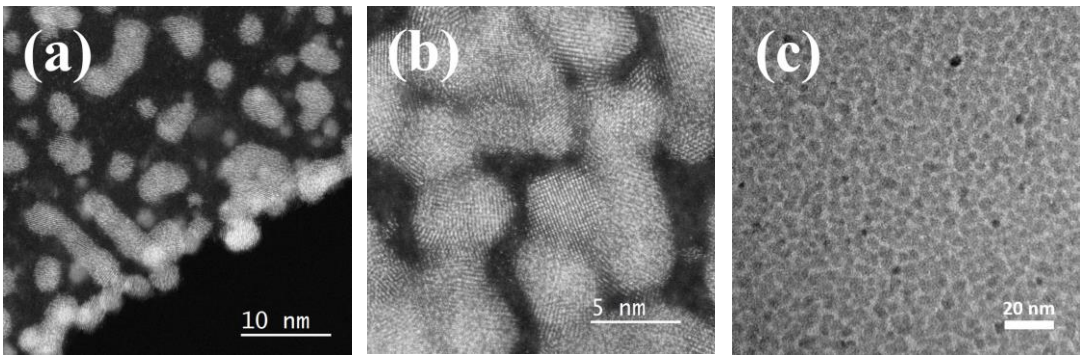

Figure S4. Images of NPs obtained by sputtering onto TEM grid for 30 s under sputtering current of (a) 20 mA (STEM), (b) 40 mA (STEM) and (c) 50 mA (TEM).

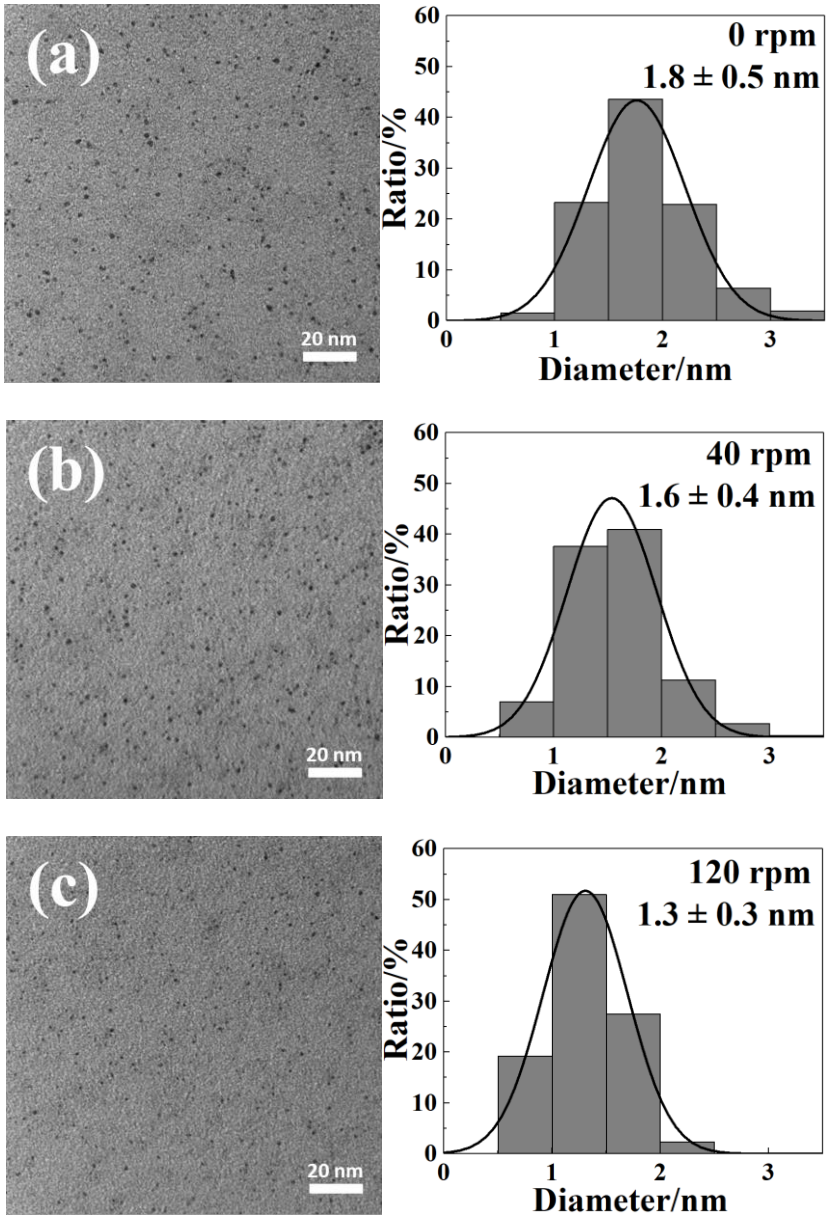

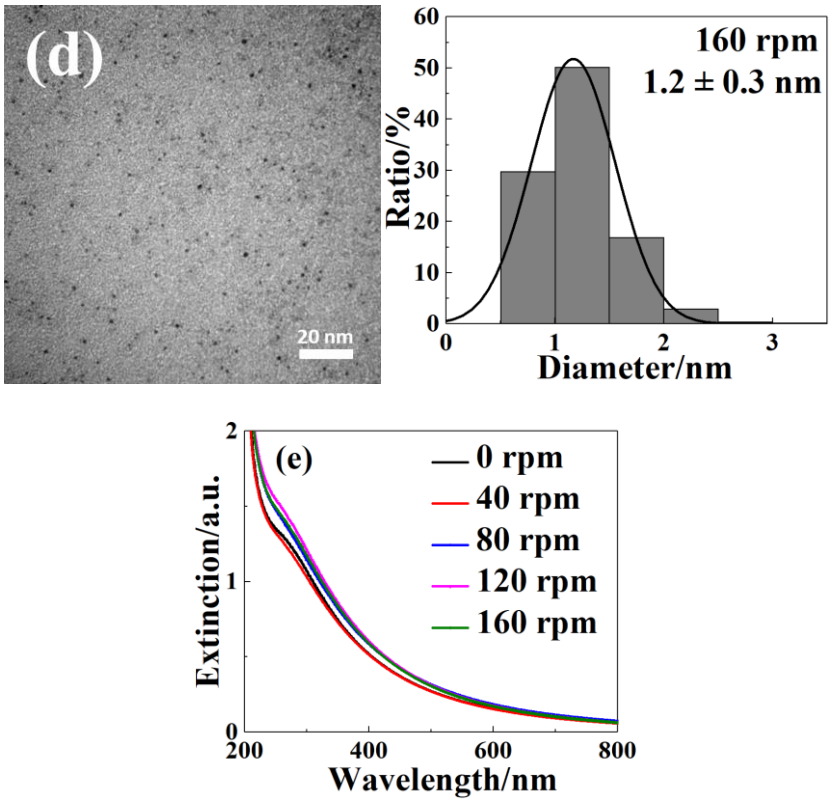

Figure S5. TEM images and size histograms of Pt/Cu NPs obtained by continuous sputtering onto PEG at a fixed sputtering current of 30 mA at 30 °C for 30 min at different rotation speeds of the stirrer. (a) 0, (b) 40, (c) 120, and (d) 160 rpm. The image and size histogram of Pt/Cu NPs prepared at the rotation speed of 80 rpm is shown in Figure 4.5(d). (e) Corresponding UV-Vis absorption spectra of Pt/Cu NPs obtained by sputter deposition onto PEG with sputtering current of 30 mA for 30 min at 30 °C with a rotation speed of 0 rpm (black curve), 40 rpm (red curve), 80 rpm (blue curve), 120 rpm (pink curve) and 160 rpm (green curve).

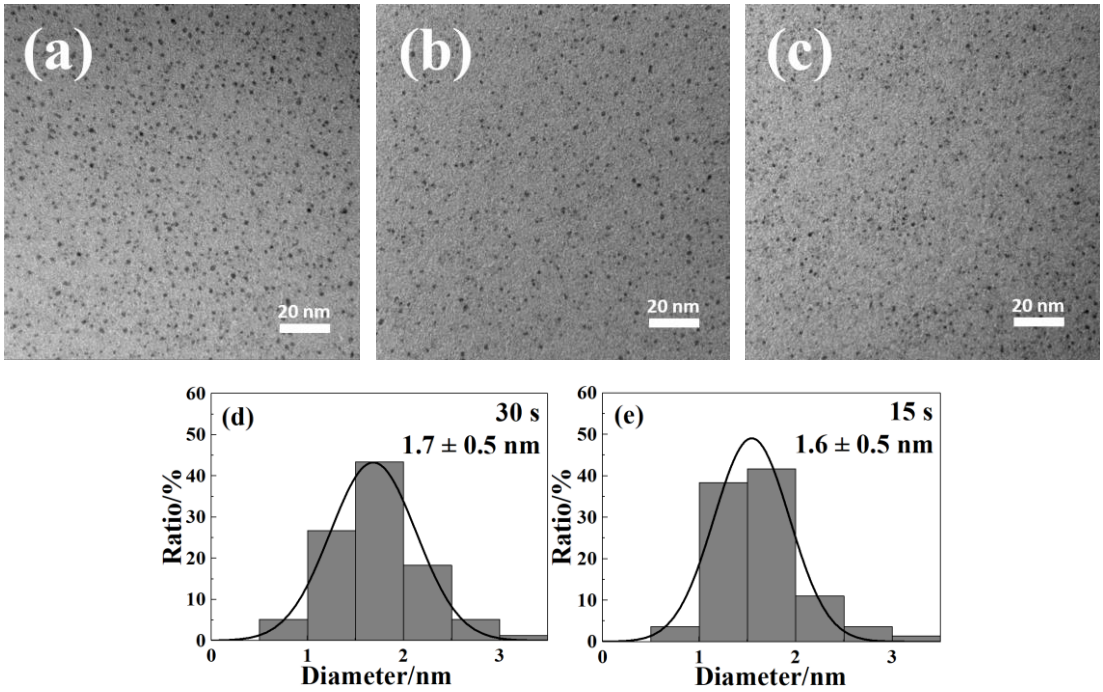

Figure S6. TEM images of Pt/Cu NPs at a fixed sputtering current of 50 mA, rotation speed of 80 rpm, PEG temperature of 30 °C, and different sputtering periods of (a) 30, (b) 15, and (c) 5 s. and corresponding size histogram at sputtering periods of (d) 30 s and (e)15 s.

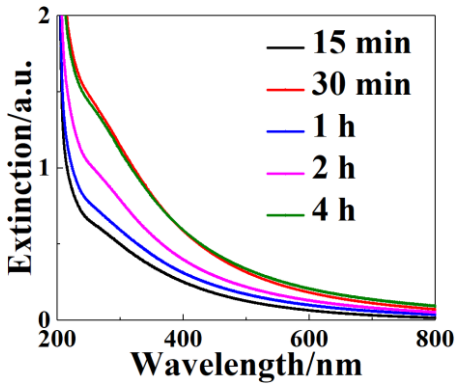

Figure S7. UV-Vis absorption spectra of Pt/Cu NPs obtained by sputter deposition onto PEG with sputtering current of 30 mA at 30 °C with rotation speed of 80 rpm for 15 min (black curve), 30 min (red curve), 1 h (blue curve), 2 h (pink curve) and 4 h (green curve). Samples sputtered for 1, 2 and 4 h were diluted 3, 5 and 7 times respectively using PEG before measuring UV-Vis spectra.

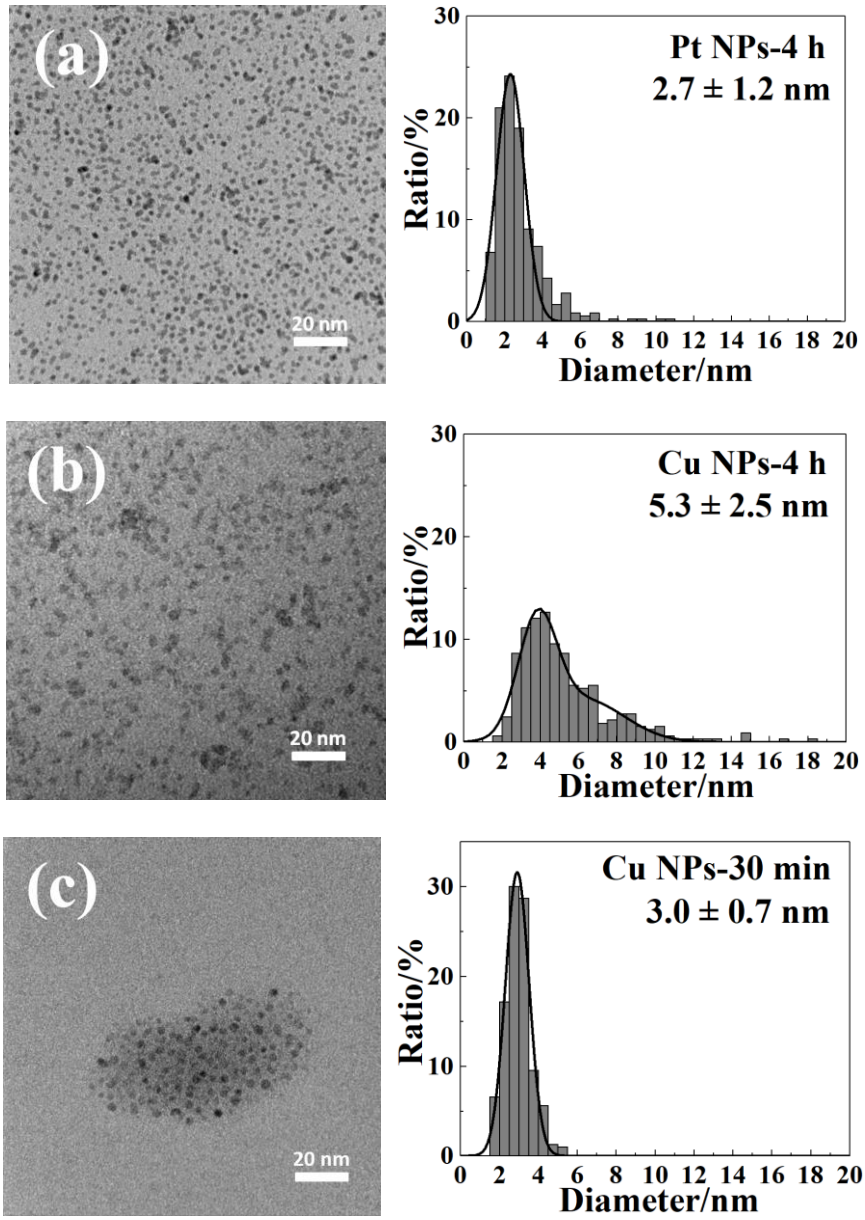

Figure S8. TEM images of Pt NPs (a) and Cu NPs (b) obtained by continuously sputtering onto PEG for 4h, and Cu NPs obtained by continuously sputtering onto PEG for 30 min (c) at a fixed sputtering current of 30 mA, at 30 °C, rotation speed of 80 rpm and corresponding size distribution.

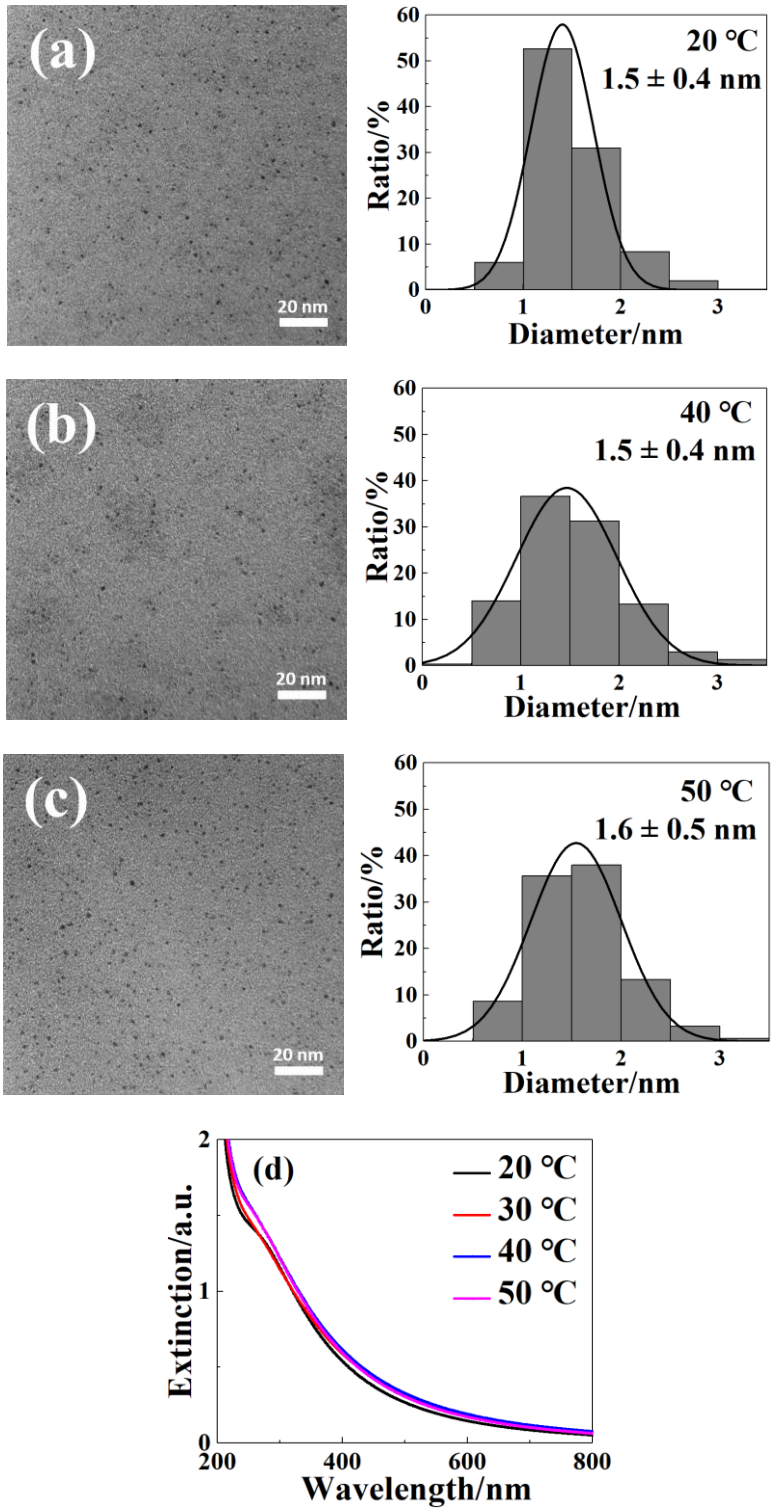

Figure S9. TEM images and the corresponding size histograms of Pt/Cu NPs obtained by continuous sputtering onto PEG at a fixed sputtering current of 30 mA and rotation speed of 80 rpm for 30 min at different PEG temperatures: (a) 20, (b) 40, and (c) 50 °C. (d) Corresponding UV-Vis absorption spectra of Pt/Cu NPs.

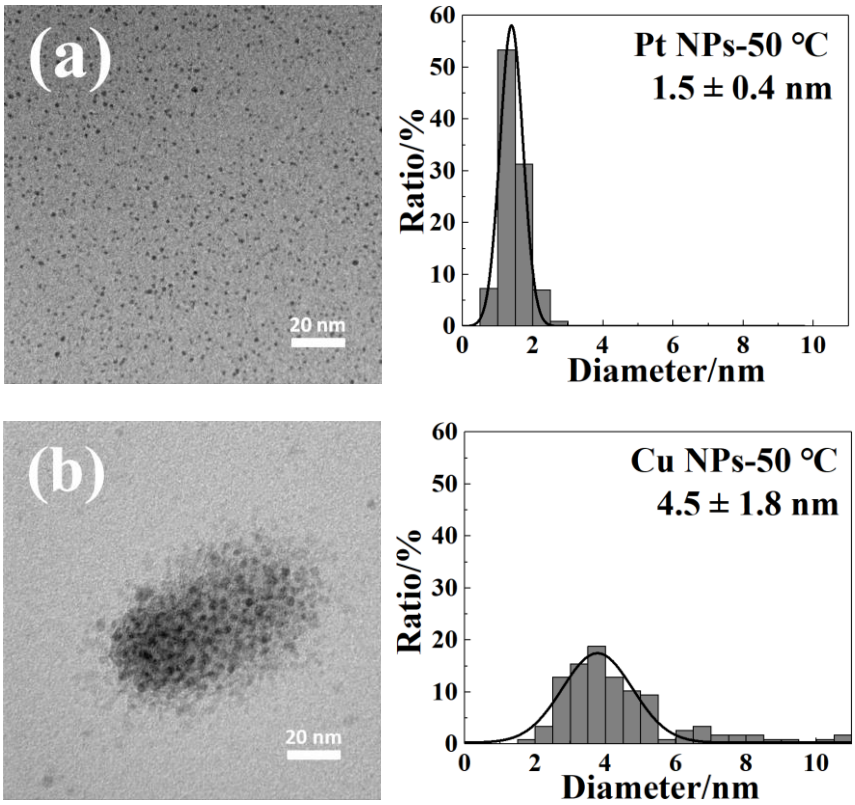

Figure S10. TEM images of Pt NPs (a) and Cu NPs (b) obtained by sputtering onto PEG under sputtering current of 30 mA at 50 °C with rotation speed of 80 rpm for 30 min and corresponding size distribution.

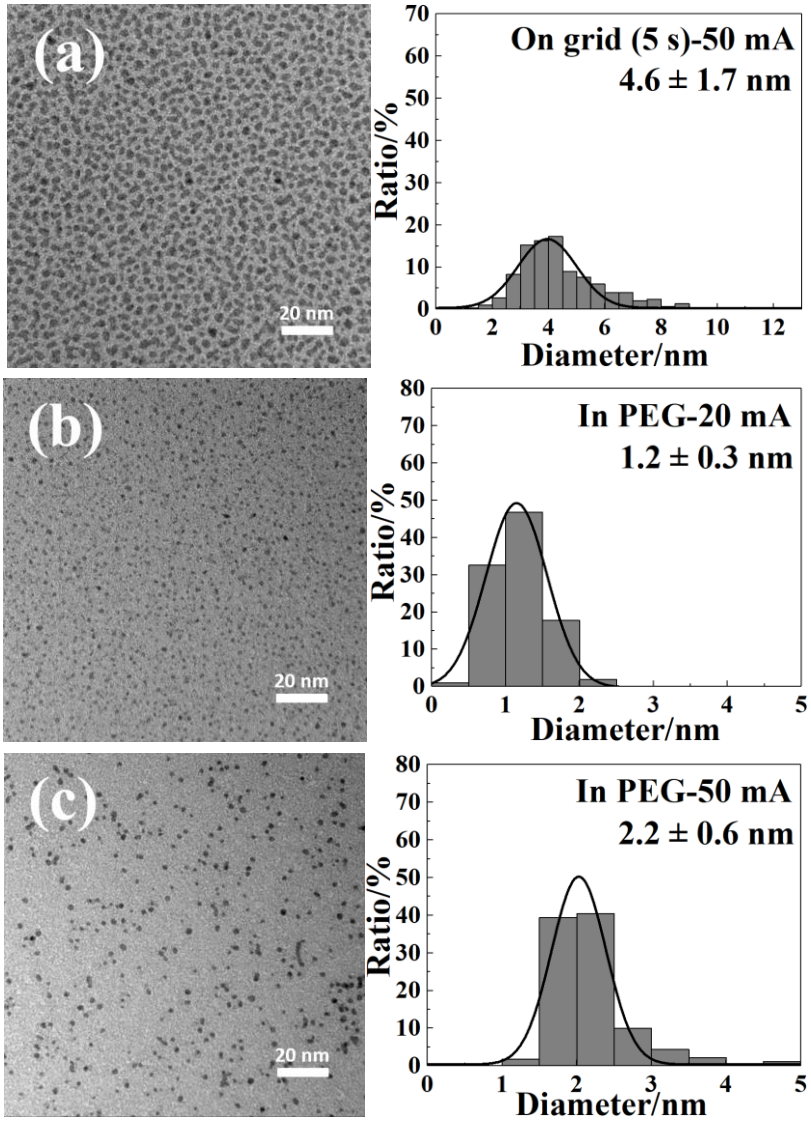

Figure S11. TEM images and size histograms of the NPs obtained by sputtering onto TEM grid for 5 s using circulating cooled ethanol at -10 °C for the target (a), continuous sputtering onto PEG at different sputtering currents: (b) 20 and (c) 50 mA for 30 min at 30 °C with a rotation speed of 80 rpm without using circulating cooled ethanol. The obtained particle size shows negligible differences compared to that of the samples (Figures 6e, 5c, and 5f) sputtered using circulating cooled ethanol 0 °C for the target while keeping other sputtering parameters constant.

Appendix III. Supplementary information for chapter 4

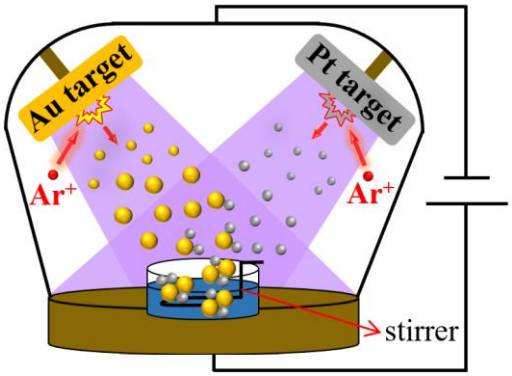

Figure S1. Schematic illustration of the synthesis of Pt/Au alloy NPs via double target sputtering onto PEG.

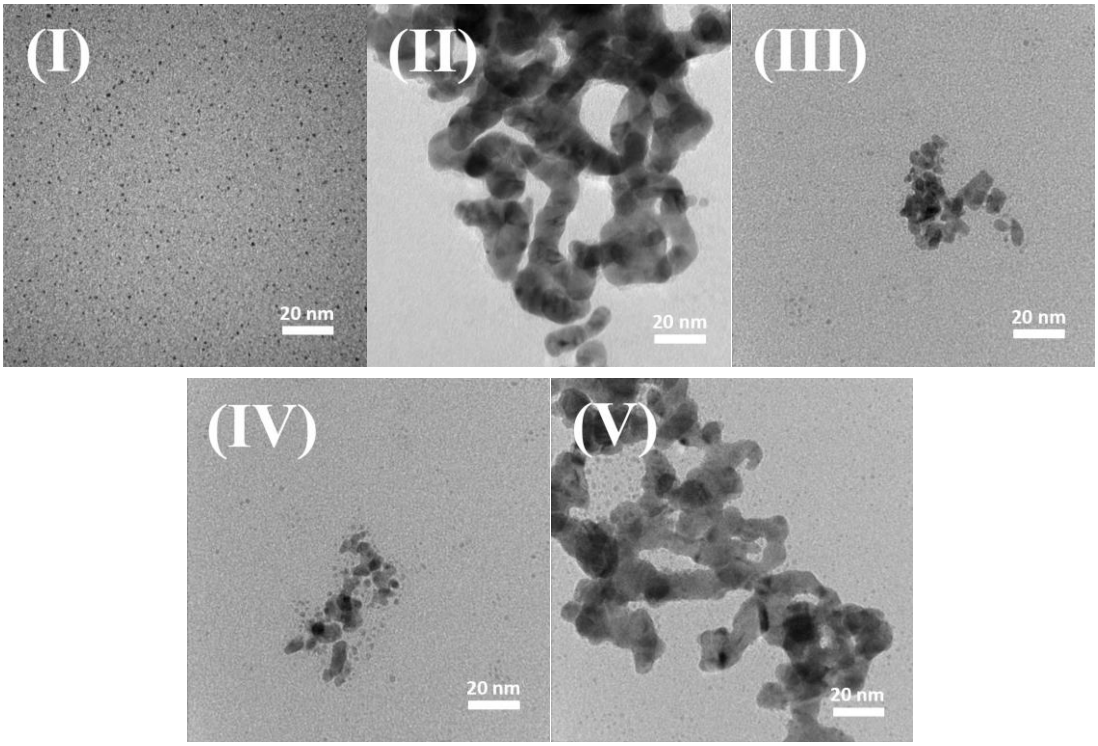

Figure S2. TEM images of Pt (I), Au (II), PEG-Pt NPs dispersion mixed with PEG-Au NPs dispersion (III), sputter Pt target for 30 min followed by sputtering Au target for 30 min (IV), and sputter Au target for 30 min followed by sputtering Pt target for 30 min (V).

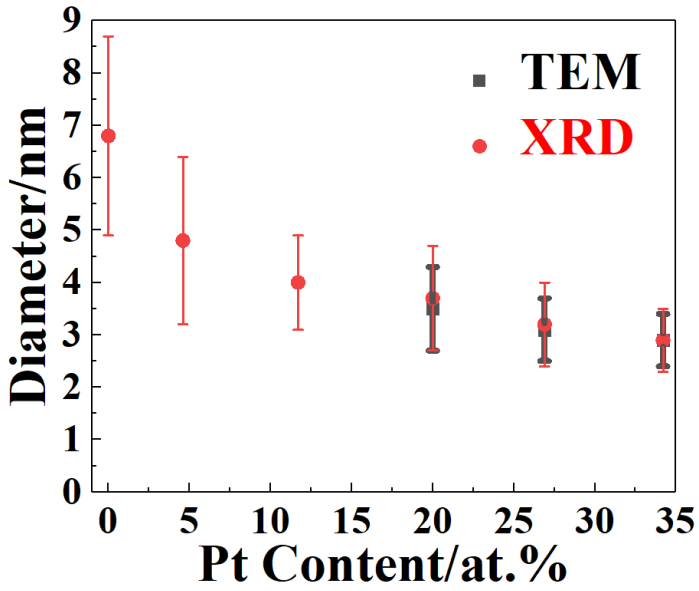

Figure S3. Changes in crystallite diameter and particle diameter with changes in proportion of Pt (at.%) in NPs. Crystallite diameter of Pt/Au NPs, calculated based on the measured 2θ values of (111) and (200) diffraction lines.

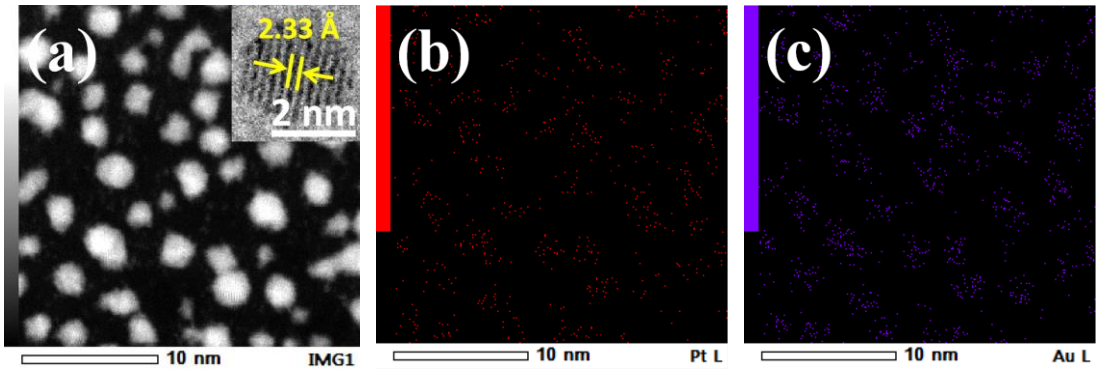

Figure S4. HAADF-STEM image of NPs obtained by sputtering onto TEM grid under sputtering current of Au (50 mA) / Pt (50 mA) for 5 s (a), STEM EDX-mapping images of Pt (b) and Au (c). ((a)-(c) were obtained by JEOL JEM-ARM200F, operating at 200 kV)

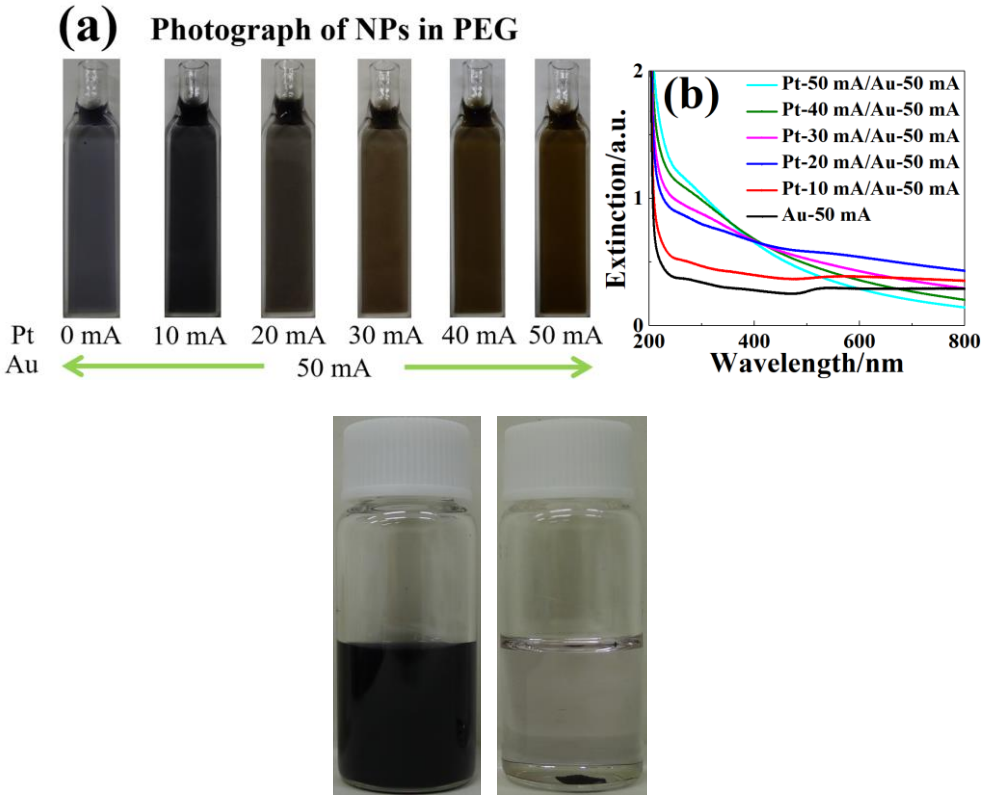

Figure S5. Photograph of PEG-dispersions produced by co-sputtering onto PEG using different sputtering current of Pt target from 0-50 mA while keeping sputtering current of Au target constant at 50 mA under ambient light (a), and corresponding UV-vis absorption spectra of PEG NPs dispersions (b), and photograph of PEG-Au NPs dispersions obtained by sputtering Au target onto PEG using sputtering current of 50 mA, right after synthesis (left) and after keeping in the dark at room temperature for several weeks (right) (c).

Table S1. XPS data on the atomic percentage of Pt in the sputtered materials prepared by sputtering onto Si wafer for 30min under sputtering current of Pt target from 0 to 50 mA while keeping sputtering current of Au target constant at 50 mA.

Pt current / mA	0	10	20	30	40	50
Pt at. %, XPS	0.0	3.5	9.8	18.2	27.3	34.1 (33.8*)

*The Pt/Au atomic ratio of the sample generated by sputtering onto PEG at the sputtering current of Pt-50 mA/Au-50 mA was also checked by XPS.

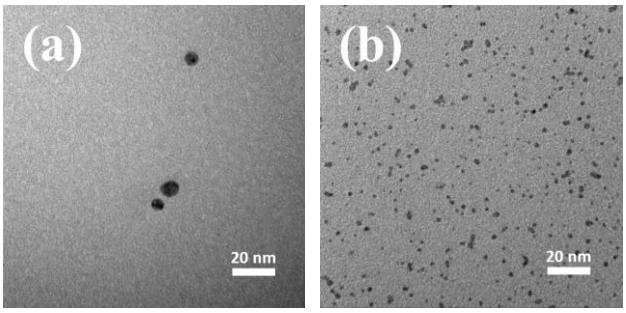

Figure S6. TEM images of PEG-NPs dispersion obtained by Ag-50 mA (a) and Pt-50 mA/Ag-50 mA (b) sputtering onto PEG.

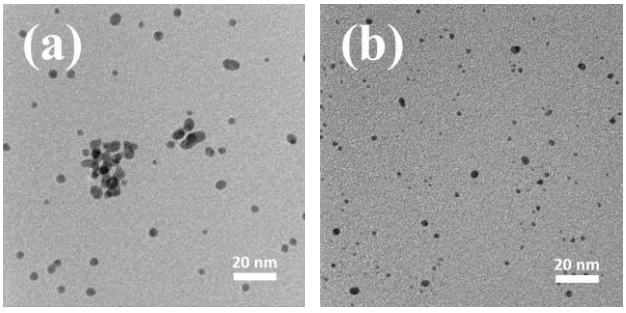

Figure S7. TEM images of PEG-NPs dispersion obtained by Ag-50 mA/Au-50 mA (a) and Cu-50 mA/Au-50 mA (b) sputtering onto PEG.

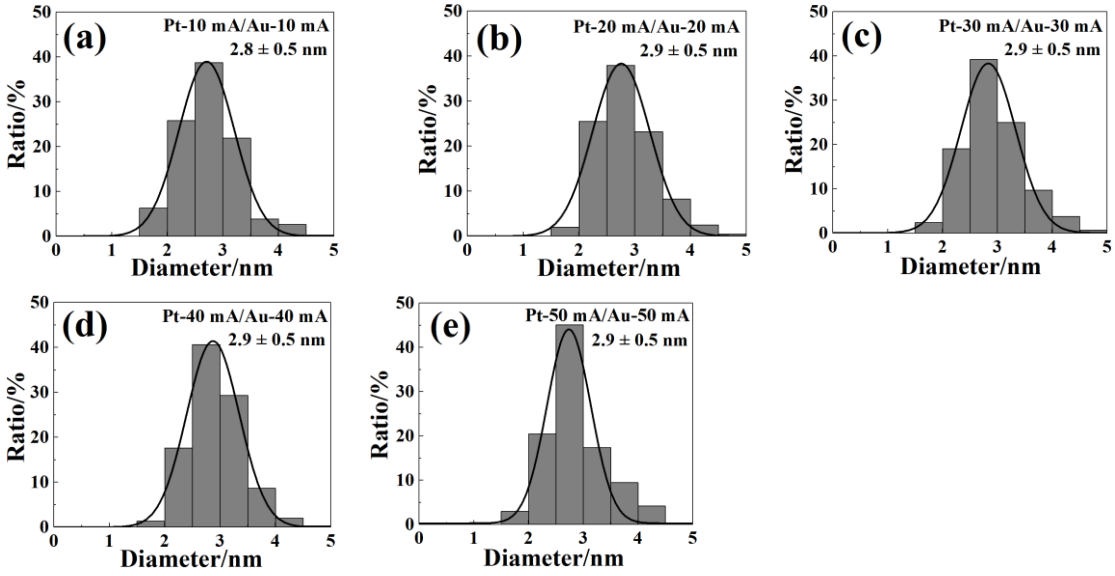

Figure S8. TEM images of PEG-NPs dispersion generated by sputtering onto PEG under various sputtering current of Pt/Au target from 10 mA/10 mA (a), 20 mA/20 mA (b), 30 mA/30 mA (c), and 40 mA/40 mA (d).

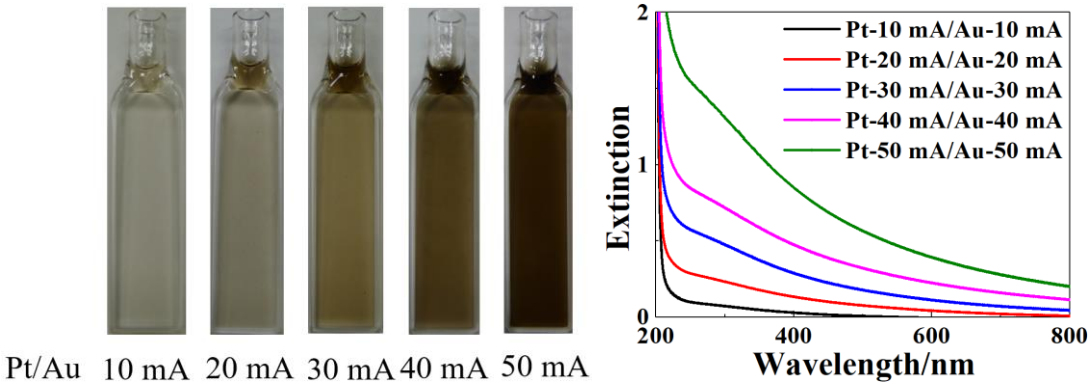

Figure S9. Photograph of PEG-NPs dispersions obtained by sputtering onto PEG under various sputtering current of Pt/Au target from 10 mA/10 mA-50 mA/50 mA. under room light (left), and corresponding UV-Vis absorption spectra of PEG-NPs dispersions (right).

Table S2. Deposition amount of Pt/Au in PEG sputtered using different sputtering current and time.

Sputtering current of Pt-Au (mA-mA)	10-10	20-20	30-30	40-40	50-50
Deposition amount for 3 min sputtering (mg) (Particle size (nm))					0.6 (2.5±0.5)
Deposition amount for 30 min sputtering (mg) (Particle size (nm))	0.5 (2.8±0.5)	1.5 (2.9±0.5)	2.6 (2.9±0.5)	4.1 (2.9±0.5)	5.6 (2.9±0.5)
Deposition amount for 60 min sputtering (mg) (Particle size (nm))					11.2 (2.9±0.9)
Deposition amount for 90 min sputtering (mg) (Particle size (nm))					16.8 (3.7±1.5)
Deposition amount for 240 min sputtering (mg) (Particle size (nm))		12.0 (2.9±0.8)			44.8 (4.5±1.8)

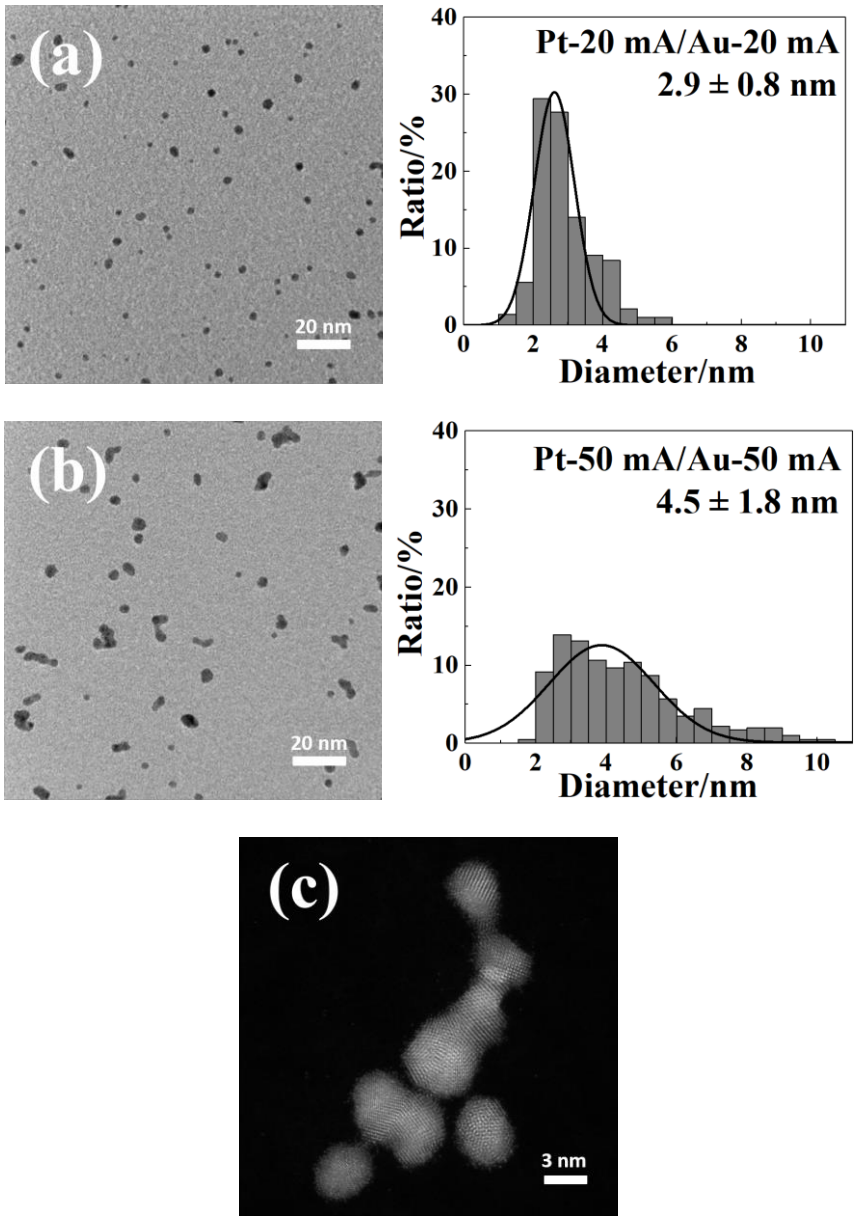

Figure S10. TEM images of PEG-NPs dispersion produced by sputtering onto PEG for 4 h under sputtering current of Pt-20 mA/Au-20 mA (a), Pt-50 mA/Au-50 mA (b), and corresponding STEM image (c).

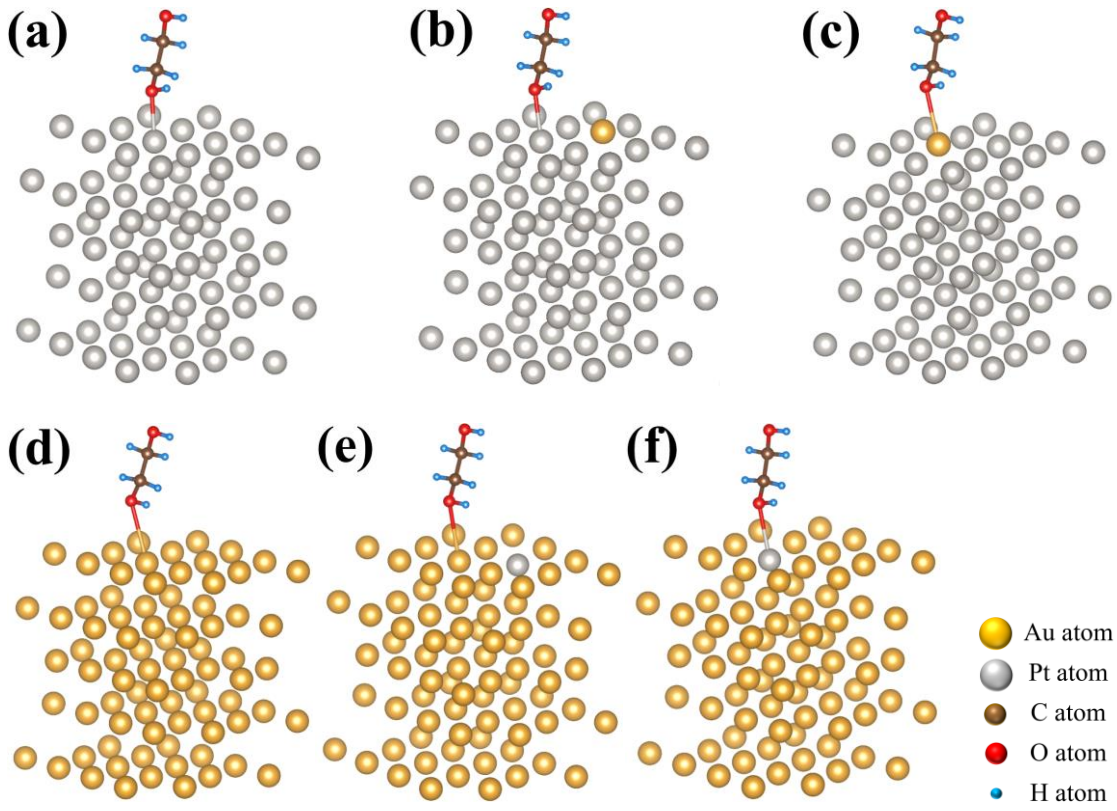

Figure S11. Final relaxed structure for PEG molecule adsorbed on Pt in Pt (111) surface (a), Pt in Pt/Au (111) surface (one Pt atom substituted by one Au atom in structure (a)) (b), Au in Pt/Au (111) surface (one Pt atom substituted by one Au atom in structure (a) (c), Au in Au (111) surface (d), Au in Pt/Au (111) surface (one Au atom substituted by one Pt atom in structure (d)) (e), and Pt in Pt/Au (111) surface (one Au atom substituted by one Pt atom in structure (d)) (f).

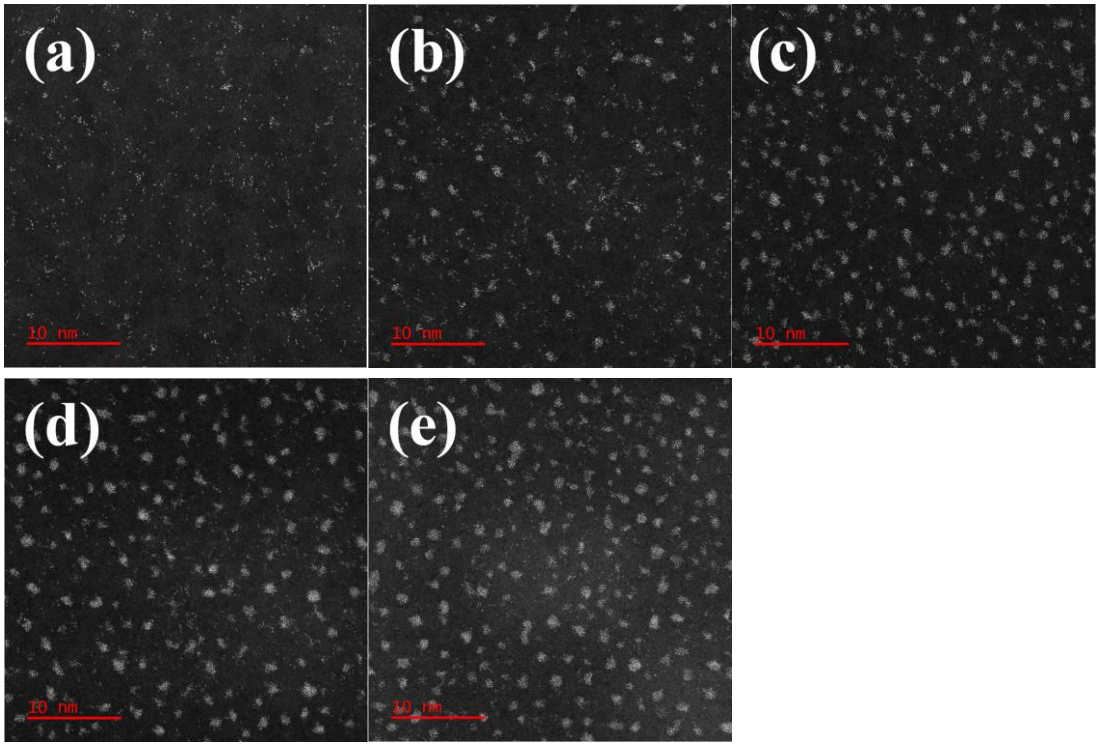

Figure S12. STEM images of Pt NPs obtained by sputtering onto TEM grid for 1s under various sputtering current of Pt target from 10 (a), 20 (b), 30 (c), 40 (d) and 50 mA (e).

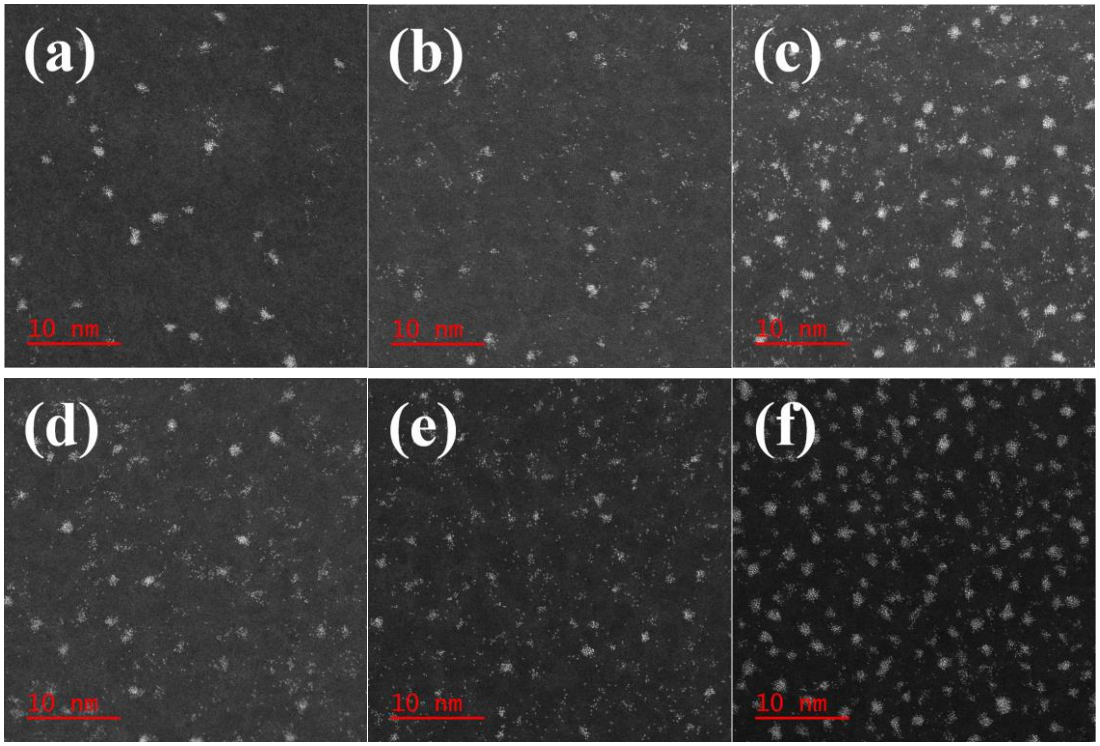

Figure S13. STEM images of NPs obtained by sputtering onto TEM grid for 1s under various sputtering current of Pt target from 0 (a), 10 (b), 20 (c), 30 (d), 40 (e) and 50 mA (f) while keeping sputtering current of Au target constant at 20 mA.

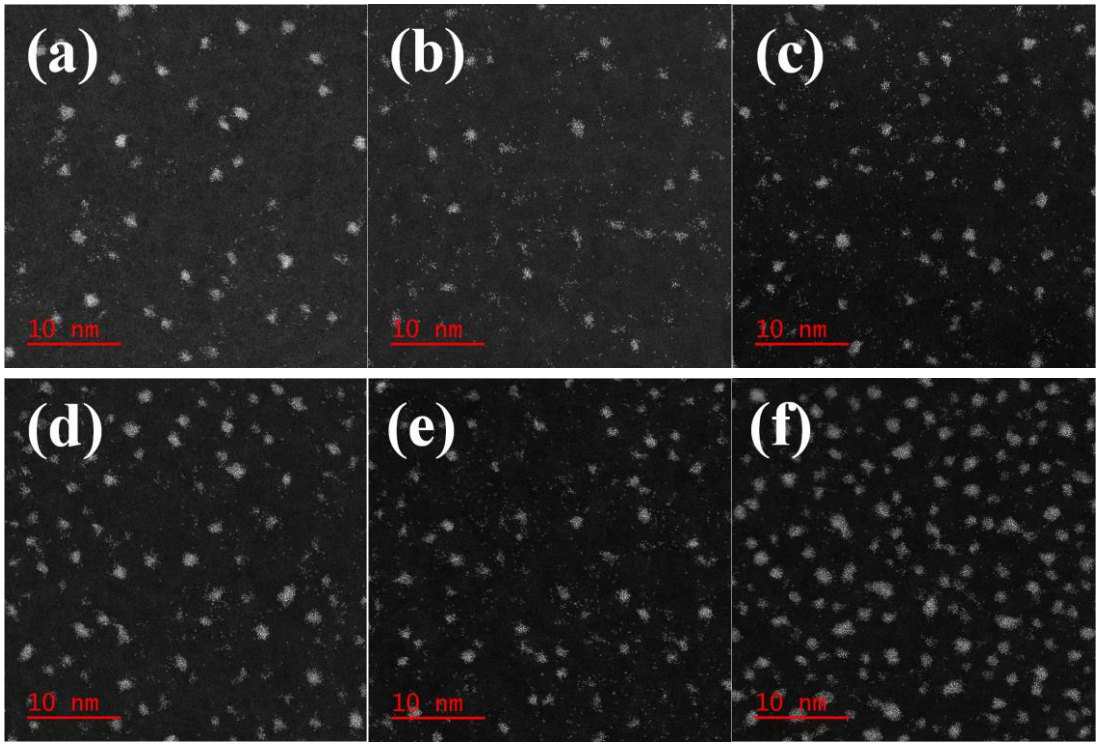

Figure S14. STEM images of NPs obtained by sputtering onto TEM grid for 1s under various sputtering current of Pt target from 0 (a), 10 (b), 20 (c), 30 (d), 40 (e) and 50 mA (f) while keeping sputtering current of Au target constant at 40 mA.

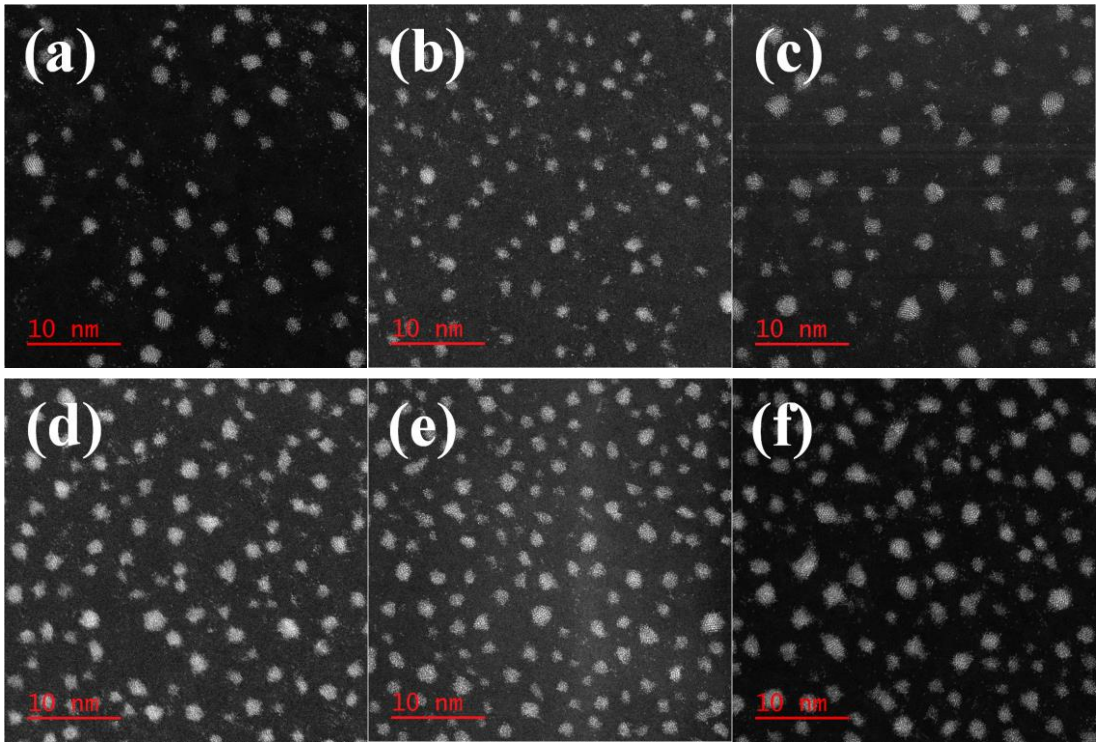

Figure S15. STEM images of NPs obtained by sputtering onto TEM grid for 1s under various sputtering current of Pt target from 0 (a), 10 (b), 20 (c), 30 (d), 40 (e) and 50 mA (f) while keeping sputtering current of Au target constant at 50 mA.

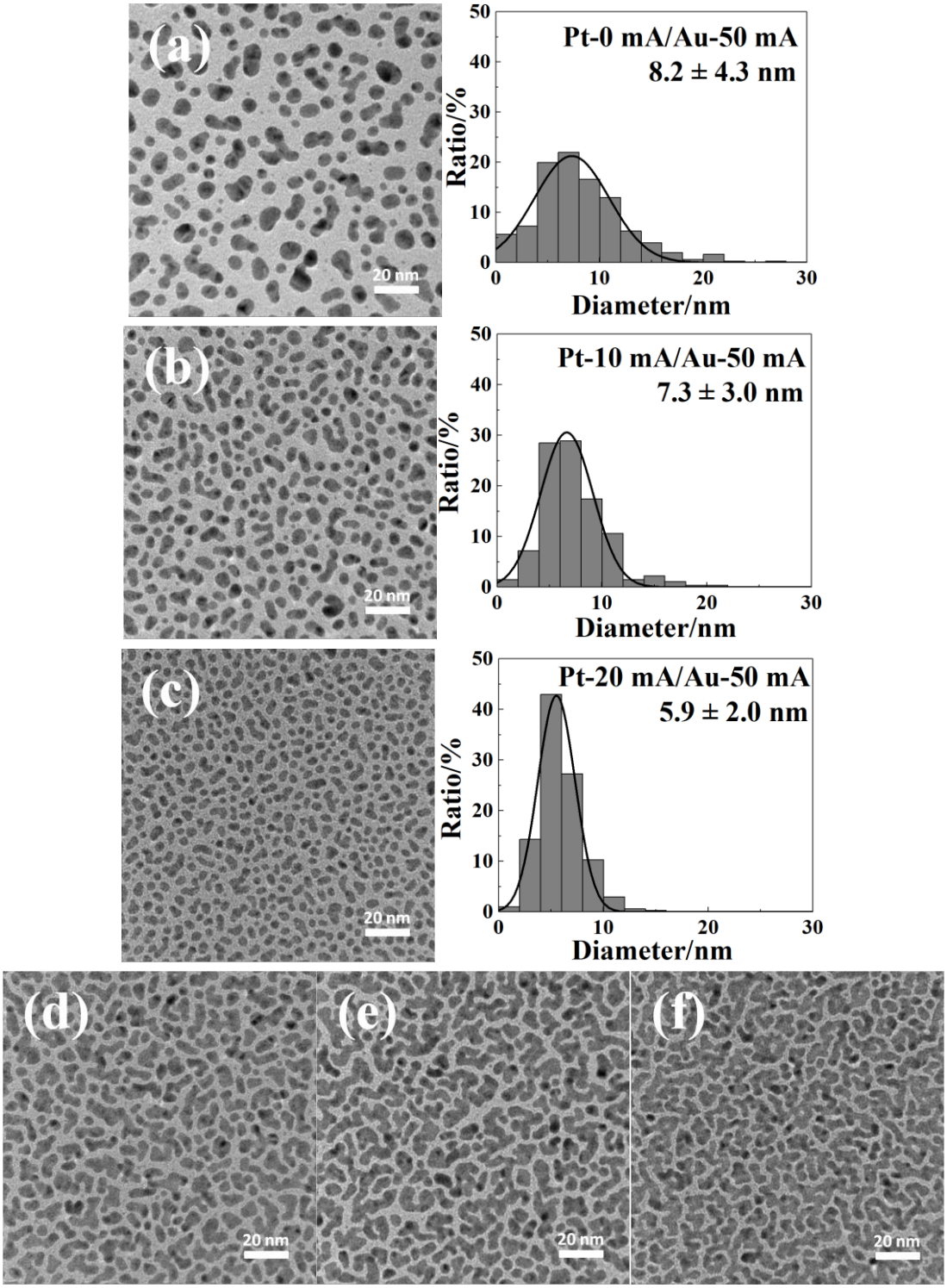

Figure S16. TEM images of NPs obtained by sputtering onto TEM grid for 30 s under various sputtering current of Pt target from 0 (a), 10 (b), 20 (c), 30 (d), 40 (e) and 50 mA (f) while keeping sputtering current of Au target constant at 50 mA.

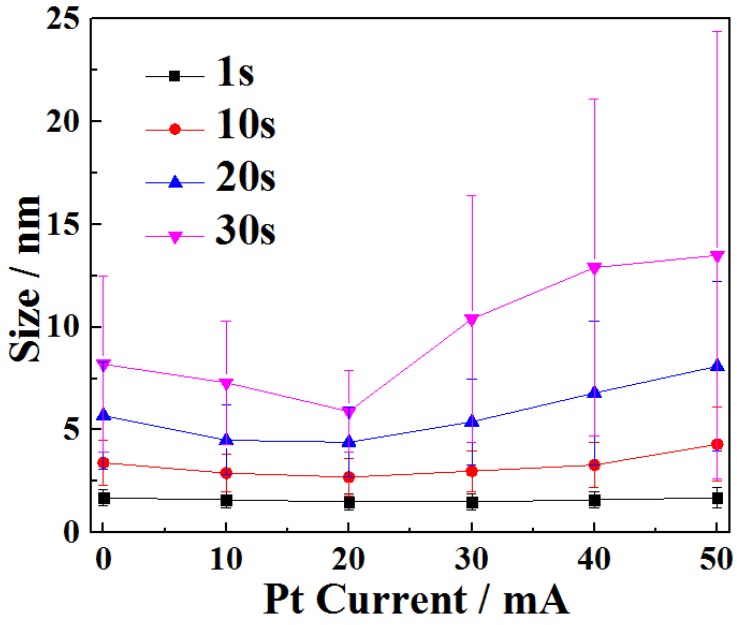

Figure S17. Relation between particle size and sputtering current of Pt sputtered onto TEM grid under the 50 mA of Au for 1 s (black), 10 s (red), 20 s (blue) and 30 s (pink).

List of publications

1st Author

i. Sub-2 nm single-crystal Pt nanoparticles via sputtering onto a liquid polymer. L. Deng, M. T. Nguyen, T. Yonezawa. Langmuir, 2018, 34(8): 2876-2881.

ii. Preparation and growth mechanism of Pt/Cu alloy nanoparticles by sputter deposition onto a liquid polymer. L. Deng, M. T. Nguyen, S. Mei, T. Tokunaga, M. Kudo, S. Matsumura, T. Yonezawa. Langmuir, 2019, 35, 8418-8427.

iii. Highly Correlated Size and Composition of Pt/Au Alloy Nanoparticles via Magnetron Sputtering onto Liquid. L. Deng, M. T. Nguyen, J. Shi, T. Y. R. Chau, S. Mei, K. Li, T. Tokunaga, M. Kudo, S. Matsumura, N. Hashimoto, T. Yonezawa. To be submitted.

Co-Authored

i. Au/Cu bimetallic nanoparticles via double-target sputtering onto a liquid polymer. M. T. Nguyen, H. Zhang, L. Deng, T. Tokunaga, T. Yonezawa. Langmuir, 2017, 33(43): 12389-12397.

ii. Monitor the Growth and Oxidation of Cu-nanoparticles in PEG after Sputtering. Y. R. Chau, L. Deng, M. T. Nguyen, T. Yonezawa. MRS Advances, 2019, 4(5-6): 305-309.

List of research accomplishments

Conference attended

1. The Chemical Society of Japan, Hokkaido Region Meeting, Summer Session

Preparation of Pt and Alloy Nanoparticles by Matrix Sputtering

(oral presentation, Jul. 22nd, 2017, Asahikawa)

2. The 161th Annual Fall Meeting of The Japan Institute of Metals and Materials

Single Target Sputter Deposition into Liquid to Prepare Pt and Alloy Nanoparticles

(poster presentation, Sept. 6th-8th,2017, Sapporo)

3. The Iron and Steel Institute of Japan and The Japan Institute of Metals and Materials, Hokkaido Region Meeting

Double target sputtering onto liquid to prepare Pt/Au alloy nanoparticles

(oral presentation, Jan. 25th-26th, 2018, Sapporo)

4. The Japan Institute of Metals and Materials, Hokkaido Region Meeting

Au/Pt alloy nanoparticles prepared by sputtering onto liquid

(poster presentation, Jul. 13th, 2018, Sapporo)

5. The 69th Divisional Meeting on Colloid and Surface Chemistry Compositional Dependent AuPt Alloy Nanoparticles via Sputtering onto PEG

(oral presentation, Sept. 18th-20th, 2018, Tsukuba)

Sputtering onto PEG for Sub 2nm Single Crystal Pt Nanoparticles

(poster presentation, Sept. 18th-20th, 2018, Tsukuba)

6. 2018 MRS Fall Meeting

Sputter Deposition onto Liquid to Prepare Pt and Pt Alloy Nanoparticles

(poster presentation, Nov. 25th-30th, 2018, Boston)

7. The Iron and Steel Institute of Japan and The Japan Institute of Metals and Materials, Hokkaido Region Meeting

Pt/Cu Alloy Nanoparticles via Sputter Deposition onto Liquid Polymer

(oral presentation, Jan. 10th-11st, 2019, Muroran)

8. The 99th Chemical Society Japan Annual Meeting

Study the Growth of Pt/Cu Alloy Nanoparticles Prepared by Sputter Deposition onto a Liquid Polymer

(oral presentation, Mar. 16th-19th, 2019, Kobe)